

Department of Physics and Astronomy

University of Heidelberg

Master thesis

in Physics

submitted by

Aaron Spring

born in Frankfurt/Main

2017

**Decadal variations
of the Southern Ocean carbon sink
in 100 historical MPI-ESM ensemble simulations**

This Master thesis has been carried out by Aaron Spring
at the institute of Environmental Physics
under the supervision of
Prof. Dr. Norbert Frank
and
Dr. Tatiana Ilyina
from
Max Planck Institute for Meteorology, Hamburg,
Ocean Biogeochemistry, Ocean in the Earth System

ABSTRACT

Recent observations suggest pronounced decadal variations in the Southern Ocean carbon sink. However, due to the sparse spatial and temporal coverage of observations, it is challenging to distinguish the dynamics of internally varying processes. Earth system models (ESMs), while being a useful tool to analyze processes that contribute to variability, rarely capture this variability. By analyzing a large ensemble of 100 historical simulations based on Max Planck Institute's ESM (MPI-ESM) starting from different initial conditions but using identical forcing, I assess modeled decadal internal variability of sea-air CO₂ flux in the Southern Ocean.

The modeled decadal internal variability of the Southern Ocean carbon sink south of 35°S is quantified to $\sim \pm 0.19$ PgC/yr/decade in the historical period. This amounts to $\sim 12\%$ of the mean state of the Southern Ocean carbon sink at ~ 1.15 PgC/yr and dominates over the increasing forced Southern Ocean CO₂ uptake signal of ~ 0.14 PgC/yr/decade. MPI-ESM Large Ensemble captures decadal variations of similar magnitude as suggested by observations. The largest variability is found at 50-60°S, where CO₂ flux follows two wind-driven regimes: stronger winds enhance the upper-ocean overturning circulation and the corresponding upwelling of deep waters weakens the carbon sink. For weakening winds, the upper-ocean circulation slows down and hence strengthens the carbon sink.

ZUSAMMENFASSUNG

In kürzlich veröffentlichten Beobachtungsdaten lassen sich dekadische Schwankungen in der Kohlenstoffsenke im Südlichen Ozean erkennen. Dabei stellt es sich aufgrund der geringen räumlichen und temporären Beobachtungsdatendichte als schwierig dar, die Dynamik der variablen Prozesse zu unterscheiden. Erdsystemmodelle, die ein nützliches Hilfsmittel zur Analyse von variablen Prozessen sind, erfassen diese internen Schwankungen nur selten. In der vorliegenden Masterarbeit untersuche ich modellierte interne Variabilität der Kohlenstoffsenke im Südlichen Ozean mittels Analyse eines Ensembles von 100 historischen Simulationen, basierend auf dem Max-Planck-Institut ESM (MPI-ESM) mit leicht veränderten Anfangsbedingungen.

Die modellierte dekadische interne Variabilität der Kohlenstoffsenke im Südlichen Ozean südlich von 35°S beträgt $\sim \pm 0.19 \text{ PgC/Jahr/Dekade}$. Dies macht $\sim 12\%$ der durchschnittlichen Kohlenstoffaufnahme von $\sim 1.15 \text{ PgC/Jahr}$ im Südlichen Ozean aus und dominiert über das dortige ansteigende Klimawandelsignal von $\sim 0.14 \text{ PgC/Jahr/Dekade}$. Die 100 MPI-ESM Simulationen erfassen dekadische Trends von ähnlicher Stärke vergleichbar mit Beobachtungsdaten. Die höchste Variabilität lässt sich in der Region $50\text{-}60^{\circ}\text{S}$ erkennen, wo die Kohlenstoffflüsse durch folgende zwei Windregime beeinflusst werden: herrschen stärkere Winde, stimulieren sie die obere Umwelzzirkulation, was das Aufsteigen von Tiefenwasser verstärkt und durch das darauf folgende Ausgasen die Kohlenstoffsenke reduziert; auf der anderen Seite verlangsamten schwächere Winde die Umwelzzirkulation und stärken somit die Kohlenstoffsenke.

CONTENTS

1	INTRODUCTION	1
2	METHODS	5
2.1	Model description of MPI-ESM	5
2.2	Large ensemble simulations	8
2.3	Observational data	10
2.4	Statistical methods	11
2.5	Climatological methods	12
3	MODEL EVALUATION IN THE SOUTHERN OCEAN	15
3.1	CO ₂ flux	15
3.2	Winds	20
3.3	Biology	23
3.4	Upper-Ocean Overturning Circulation	27
4	PROCESSES CORRESPONDING TO MULTI-YEAR TRENDS IN SEA-AIR CO ₂ FLUX	31
4.1	The role of westerly winds in Southern Ocean CO ₂ flux variability	31
4.2	Positive CO ₂ flux trends	34
4.3	Negative CO ₂ flux trends	41
5	CONTRIBUTION OF DIFFERENT PROCESSES TO MULTI-YEAR PCO ₂ TRENDS	47
5.1	Derivation of the framework	47
5.2	Estimate of pCO ₂ drivers	51
6	SUMMARY, CONCLUSIONS AND OUTLOOK	59
A	APPENDIX	63
	BIBLIOGRAPHY	83

INTRODUCTION

The increasing atmospheric concentrations of carbon dioxide (CO_2) drive anthropogenic climate change, which alters the Earth's climate system at a soaring rate [Crutzen, 2002]. While roughly half of the anthropogenic CO_2 emissions remain in the atmosphere, the carbon reservoirs in oceans and on land modulate the global carbon cycle and hence the climate [Le Quéré et al., 2016]. The oceans currently take up about 25-30% of the anthropogenic carbon emissions [Sabine et al., 2004]. As a key region, the Southern Ocean is estimated to contribute about 50% to the global ocean carbon sink [Takahashi et al., 2012]. The large uptake ability of the Southern Ocean arises from its unique position in the global overturning circulation [Talley, 2013]. Deep upwelled waters, which have not been exposed to the atmosphere of higher CO_2 , take up additional anthropogenic CO_2 and sink back into the ocean as intermediate waters [Morrison et al., 2015]. Additionally, primary production in the Southern Ocean sequesters carbon into the deep ocean [Falkowski et al., 1998]. Moreover, high solubility of pCO_2 in the Southern Ocean due to low sea-surface temperature permits the waters to hold higher oceanic pCO_2 concentrations than in the tropical oceans [Heinze et al., 2015].

The extreme conditions of the Southern Ocean result in sparse spatial and temporal coverage of observations, so even various observation-based CO_2 flux products yield large uncertainties [Rödenbeck et al., 2015]. Also modeling results have a large spread [Wang et al., 2016] but claim the Southern Ocean as a constraint to reduce model uncertainties in future projections [Kessler and Tjiputra, 2016].

Recent observations suggest pronounced decadal variations in the Southern Ocean carbon sink [Rödenbeck et al., 2013; Landschützer et al., 2015]. Understanding internal variability is important to recognize whether strong trend occur due to external forcing or arise from natural fluctuations of the earth system [Murphy et al., 2004]. Contrasting the expected increasing Southern Ocean carbon sink due to the increasing atmospheric forcing, Landschützer et al. [2015] even reported a decadal declining trend in the 2000s. Due to sparse measurement data, it is challenging to distinguish the dynamics of internally varying processes, which demands for the evaluation and can be provided by models. Models, numerical representations of the climate system based on physical, biological and chemical principles, are a useful tool to analyze processes that contribute to variability.

Supposing the strength and position of the westerly winds as the major reason for climate variability for the Southern Ocean [Thompson et al., 2000; 2011], the carbon cycle responds in the thermal pCO₂ effect, circulation changes and biological production.

By forcing an ocean model with atmospheric reanalysis data, Lovenduski et al. [2007; 2008] demonstrated that increased upwelling due to stronger and southward shifted westerly winds in the Southern Hemisphere cause a decline in the Southern Ocean carbon sink.

Yet, Earth System Models ([ESMs](#)) containing a freely evolving coupled atmospheric and ocean component have challenges in capturing the decadal variations in sea-air CO₂ flux as suggest by observations [Wang et al., 2016]. Advances in computing power now enable simulating a larger number of model realizations, which increases the likelihood of capturing pronounced decadal trends. Using a large ensemble of simulations with perturbed initial conditions but identical forcing and model allows to separate trends into an ensemble mean trend, the forced signal, and the residual, the internal variability [McKinley et al., 2016; 2017].

By using a large ensemble of 100 simulations based on the [MPI-ESM](#) (hereafter [MPI-ESM LE](#)) I investigate the decadal internal variability of oceanic carbon uptake to answer the following research questions:

- What is the modeled internal variability of the Southern Ocean carbon sink?
- What are the sources of this internal variability?
- What are the contributions of different processes to multi-year trends in sea-air CO₂ flux in the Southern Ocean?

My thesis revisits the dominant processes leading to strong trends in the Southern Ocean carbon sink [similar to Lovenduski et al., 2007; 2008] in the ocean biogeochemical model HAMburg Ocean Carbon Cycle Model ([HAMOCC](#)) of [MPI-ESM](#).

This revisit is particularly interesting as other large ensembles of perturbed initial conditions [ESM](#) simulations do not capture strong decadal variations in the Southern Ocean carbon sink whereas [MPI-ESM LE](#) does [Li & Ilyina, in preparation; private communication N. Lovenduski ([NCAR](#)) and S. Schlunegger ([GFDL](#))].

Working on my research questions builds the outline for this thesis: I describe the large ensemble of MPI-ESM simulations in ch. 2 and evaluate the model with respect to the key features related to the Southern Ocean carbon sink variability in ch. 3. Hereafter I qualitatively describe the response of individual processes related to changes in Southern Hemisphere winds in ch. 4. In ch. 5 I quantitatively assess the individual responses of different processes on oceanic pCO₂. Finally in ch. 6 I draw my main conclusions and evaluate how attributable perturbed initial conditions large ensembles are for internal variability in observations and give an outlook on possible future research.

2

METHODS

2.1 MODEL DESCRIPTION OF MPI-ESM

The Max Planck Institute-Earth System Model (**MPI-ESM**) consists of coupled general circulation models of the atmosphere **ECHAM6** [Stevens et al., 2013] and ocean **MPIOM** [Jungclaus et al., 2013] as well as subsystem models for vegetation on land **JSBACH** [Reick et al., 2013] and for marine biogeochemistry **HAMOCC** [Ilyina et al., 2013]. The large ensemble simulations are based on **MPI-ESM** version 1.1.00p2¹ with a low-resolution configuration. Since the atmospheric pCO₂ levels are prescribed, terrestrial carbon cycle from the land component **JSBACH** and oceanic carbon cycle from **HAMOCC** do not interact (fig. 2.1). The full Earth System Model (**ESM**) [Giorgetta et al., 2013] as well as its components have been described and evaluated in detail by the given references. In the following subsections, I give an overview about the implemented processes affecting internal variability of the oceanic carbon cycle.

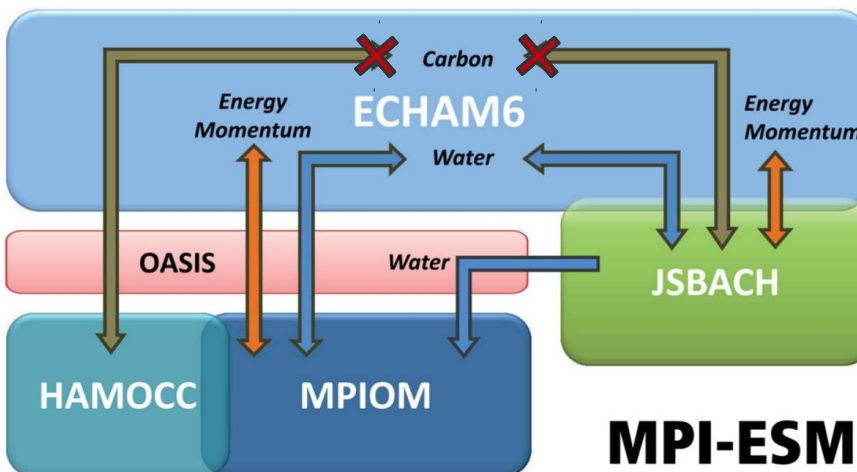


Figure 2.1: Schematic overview on the different components in **MPI-ESM** with prescribed atmospheric partial pressure pCO_{2,atm} [Giorgetta et al., 2013]

2.1.1 *ECHAM*

ECHAM is an general circulation model for the atmosphere. **ECHAM** has an sea-air gas exchange interface with **HAMOCC** and further-

¹ full source code: <https://code.zmaw.de/projects/mpi-esm/repository/show/tags/mpiesm-1.1.00p2>

more couples water, energy and momentum fluxes with **MPIOM**. The atmosphere component **ECHAM**6.3 runs on a T63 grid, corresponding to 1.9° horizontal resolution, with 47 vertical layers up to 0.01 hPa [Stevens et al., 2013]. This high vertical resolution and atmospheric height allows to model jets originating in the tropopause. Those jets define the position and strength of the westerly winds in the Southern hemisphere. Changes in **ECHAM** with regard to **CMIP5** version in Stevens et al., 2013 are described in Bittner et al., 2016. They majorly include the new radiation code of **ECHAM**6.3.

2.1.2 MPIOM

The Max Planck Institute Ocean Model (**MPIOM**) is an ocean general circulation model (OGCM) with a horizontal resolution of 1.5° on average on the Arakawa C-grid, 40 fixed-depth vertical levels on a realistic topography and with a free surface [Jungclaus et al., 2013]. The spatial resolution of 1.5° translated to a grid cell length of ~ 150 km at the northern edge of the Southern Ocean at 30°S and ~ 40 km in Antarctic coastal waters. Eddies are parametrized by the GM-scheme [Gent et al., 1995]. Therefore, the vertical mixing and diffusion based on Richardson-number dependent formulation is important for vertical gradients [Pacanowski and Philander, 1981]. Tracers are advected by the Navier-Stokes equations with Boussinesq-approximation.

The mixed-layer depth (**MLD**) is calculated by a potential density criterion where the difference between the sea-surface density and the lower end of the mixed-layer is 0.125 kg m^{-3} [Jungclaus et al., 2013].

2.1.3 HAMOCC

The **HAMOCC** is a global marine carbon cycle model which simulates oceanic carbon and nutrient cycles [Maier-Reimer, 1984; Maier-Reimer, 1993; Six and Maier-Reimer, 1996]. As a subsystem in the ocean, biogeochemical tracers except for opal and calcite shells are advected by **MPIOM**. **HAMOCC** aims to reproduce distributions of biogeochemical parameters over various timescales from seasons to millenia without regional tuning or temporal adjustments towards observations [Ilyina et al., 2013]. This includes processes on three compartments: sea-air interaction at the sea surface, biogeochemistry of the water column and sediment biogeochemistry (fig. 2.2). The **HAMOCC** model version for the large ensemble is identical to the one used in **CMIP5** which is analyzed in detail in Ilyina et al., 2013. In the following subsection, I will only give an overview about the implementation of the most relevant processes for the variability on decadal and shorter timescales.

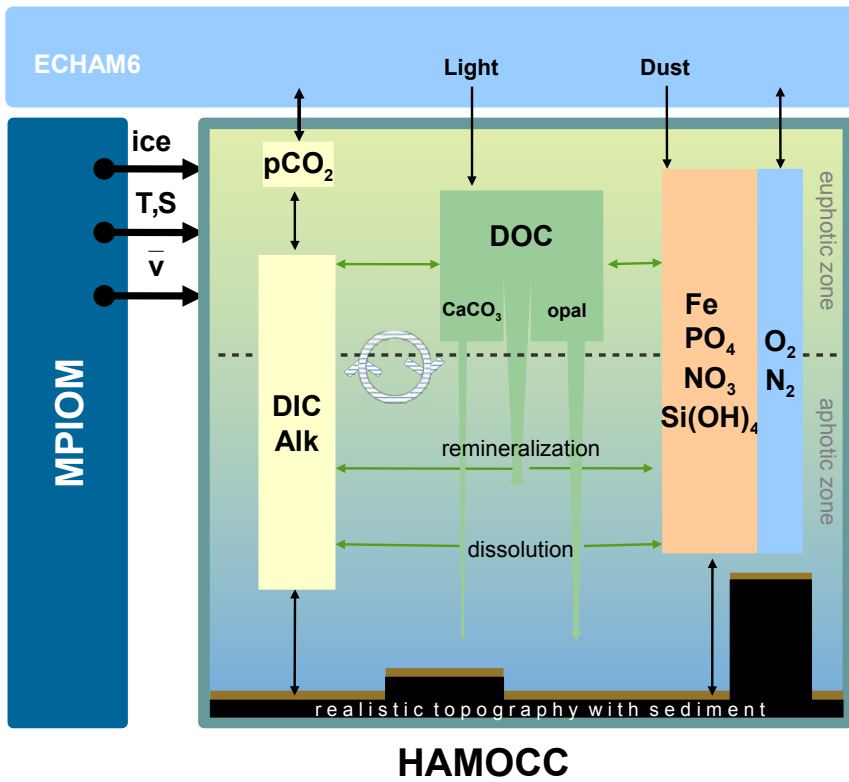


Figure 2.2: Schematic overview of the global ocean biogeochemistry model **HAMOCC** [Ilyina et al., 2013] which is coupled to the atmospheric model component **ECHAM** and the ocean model **MPIOM**. The ocean model provides state variables of physical oceanography, i.e. ice cover, temperature (T), salinity (S) and the advective velocities (\bar{v}). The water column holds tracers of gases, i.e. oxygen (O_2), nitrogen (N_2), laughing gas (N_2O), and dimethyl sulfide (DMS); nutrients, i.e. iron (Fe), phosphate (PO_4), nitrate (NO_3) and silicic acid $Si(OH)_4$; and tracers of carbonate chemistry, i.e. dissolved inorganic carbon (**DIC**) and alkalinity (**Alk**). Photosynthesis converts **DIC** and nutrients to dissolved organic carbon (**DOC**), which produces calcium carbonate ($CaCO_3$) or opal shells.

The carbonate system determines $pCO_{2,\text{ocean}}$ [Maier-Reimer, 1993]. Dissolved inorganic carbon and alkalinity are directly calculated as prognostic tracers from which other tracers derived. When $pCO_{2,\text{atm}}$ reacts with seawater, the carbonate chemistry evaluates $pCO_{2,\text{ocean}}$ based on the law of mass action formulae depending on temperature (calculated according to Weiss, 1974), salinity, **DIC** and alkalinity.

The CO₂ flux calculation implemented in the model follows an empirical relationship under the conceptual one-layer ocean-sided stagnant film model with gas transfer velocity k_w [Wanninkhof, 1992]:

$$\text{CO}_2\text{flux} = (1 - f)k_w\Delta p\text{CO}_2 \quad (1)$$

$$k_w = 0.31u_{10}^2(\text{Sc}(T)/660)^{-\frac{1}{2}}$$

$$\Delta p\text{CO}_2 = p\text{CO}_{2,\text{ocean}} - p\text{CO}_{2,\text{atm}},$$

where f is the sea-ice fraction of the grid cell, u_{10} is the wind speed at 10 m height, Sc is the temperature-dependent Schmidt number, 660 is the Schmidt number of CO₂ in seawater at 20°C and $\Delta p\text{CO}_2$ is the difference between the partial pressure of CO₂ in the atmosphere and the ocean, so positive values of sea-air CO₂ flux represent a net flux from the ocean to the atmosphere.

In the euphotic zone up to a depth of 90m, phytoplankton converts inorganic nutrients, e.g. phosphate (PO₄), nitrate (NO₃), iron (Fe) and DIC to organic matter by photosynthesis. The biological pump [Volk and Hoffert, 1985] is implemented based on an extended NPZD-type ecosystem formulation [Six and Maier-Reimer, 1996]. Phytoplankton growth is co-limited by nutrients (phosphate, nitrate and iron), temperature and light: Phytoplankton is parametrized by bulk phytoplankton, which mimics the combined growth of diatoms, coccolithophores and dinoflagellates under exponentially increasing optimum growth rate temperatures [Eppley, 1972]. Phytoplankton growth depends linearly on the availability of light, without saturation for stronger irradiance. The temperature-irradiance dependence is combined by a limitation function in Smith, 1936 (fig. A11). Michaelis-Menten kinetics describe the nutrient limitation of the maximum phytoplankton growth rate with a half-saturation constant [Michaelis and Menten, 1913]. The limiting role of nutrients is described by the nutrient availability factor that multiplies with the average growth rate of phytoplankton. The macro-nutrient iron is modeled by iron-relaxation from lignans. Iron enters the water column via a monthly dust input climatology, is used in photosynthesis and released in remineralization.

There are two different falling detritus: opal producing, if silicate is available or else calcium carbonate producing.

Once detritus reaches the ocean floor, particulate matter enters the sediment and finally the burial layer. At the upper boundary of the sediment all tracers are in exchange with the sediment via pore water exchange [Heinze et al., 1999].

2.2 LARGE ENSEMBLE SIMULATIONS

Large ensemble simulations are a novel tool to investigate model internal variability. "Climate variability refers to variations in the mean

state (...), which may be due to natural internal processes within the climate system (internal variability), or to variations in natural or anthropogenic external forcing (external variability)" [IPCC, 2013]. The variability in observations is impossible to separate, if - like in the case of $p\text{CO}_{2,\text{ocean}}$ - no long-lasting direct measurement records exist. Although modeled internal variability is not equivalent to observed internal variability, we can learn about the random variations of natural processes.

By iterating a climate simulation with an identical forcing and model code but slightly perturbed initial conditions, single ensemble members will be exposed to the same process implementations. The interplay of those at a stochastically random level lets each realization evolve in a unique way while still being bound to a common forced signal following the external forcing. Perturbed initial conditions large ensemble simulations allow to distinguish a signal into a force signal which is the average signal across all ensemble members, and the residual which modulates the signal around the forced signal due to internal variability [McKinley et al., 2016; 2017]:

$$\text{signal} = \text{forced signal} + \text{internal variability}.$$

As running large ensembles simulation comes with high computational costs, this area of climate modeling research is still more recent. There are only a few datasets available and published papers are still rare, e. g. Deser et al., 2012; Thompson et al., 2015; Lovenduski et al., 2016; Krumhardt et al., 2017; Kay et al., 2015; McKinley et al., 2016; Ilyina, 2016; Bittner et al., 2016; Hedemann et al., 2017; Rodgers et al., 2015.

The MPI-ESM LE contains 100 simulations under historical CMIP5 forcing from 1850 to 2005. The forcing includes volcano eruptions from the historical period and solar cycles. Anthropogenic forcings include well-mixed greenhouse gases, anthropogenic sulphate aerosols and land-use change. Atmospheric $p\text{CO}_2$ levels are prescribed according to the CMIP5 protocol [Taylor et al., 2012]. The carbon cycle is not coupled, so effects of changes in the terrestrial or oceanic carbon sink are not reflected in the atmospheric $p\text{CO}_{2,\text{atm}}$.

Ensemble members differ through starting from different year of the pre-industrial control simulation, so ocean and atmosphere have slightly different initial conditions in each run. This was achieved by branching off ensemble members from a 2000-year pre-industrial control run after roughly 50 years, when the historical forcing sets it.

NCAR's Community Earth System Model (CESM) LE [Kay et al., 2015] led to the first studies of perturbed initial conditions large ensembles on internal variability by Deser et al., 2012. CESM LE served for studies analyzing the timescales of trend-detection in the ocean

carbon sink [McKinley et al., 2016] and the partitioning of its uncertainties [Lovenduski et al., 2016]. The initial state of the atmosphere was slightly perturbed by roundoff-level changes to air temperature in their 32 runs.

Geophysical Fluid Dynamics Laboratory ([GFDL](#)) ran a 30-member ensemble simulation based on their model ESM2M. They used different dates separated by one day each but didn't publish any oceanic carbon uptake paper yet [Rodgers et al., 2015].

Although the initialization of ensembles differs, the variability after a few model years is not affected anymore by initialization method but by model variability [Hawkins and Sutton, 2009].

CESM Large Ensemble studies like Deser et al., 2012 and Thompson et al., 2015 assume Gaussian statistics. In sec. 2.4.3 I show that our larger ensemble generates spatial and temporal distributions with statistics similar to gaussian distributions assuming that variability does not change over this 25-yr period.

2.3 OBSERVATIONAL DATA

There are large uncertainties in observational-based CO₂ flux products, especially in the Southern Ocean [Rödenbeck et al., 2015]. Because direct pCO₂ measurements in the Southern Ocean are sparse and discontinuous, different mapping techniques lead to a spread in observation-based estimates.

For comparison of CO₂ flux with model simulations I use the Self-Organizing Map-Feed-Forward Network ([SOM-FFN](#)) data which is based on the Surface Ocean Atlas ([SOCAT](#)) Version 2 [Bakker et al., 2014] since 1982. It uses a neural network-based data interpolation to create pCO₂ maps [Landschützer et al., 2013; Landschützer et al., 2014; Landschützer et al., 2016]. The data product is smoothed by a 3x3 filter averaging two months and the neighboring grid cells but this has little effect on seasonal dynamics as this study focuses on the decadal variability. I use this pCO₂ data product because this method takes multiple variables for pCO₂ interpolation to cover regions without direct pCO₂ measurements. The input training data of the algorithm is seasonally biased as the available pCO_{2,ocean} samples originate mostly from austral summer months.

However, [SOM-FFN](#) as well as the mixed-layer scheme Jena-MLS [Rödenbeck et al., 2013; Rödenbeck et al., 2014] produce a relatively low monthly mismatch globally compared to original [SOCAT](#) data [Rödenbeck et al., 2015]. Both those data products agree on the decadal trends in the Southern Ocean. As the different data products cannot be validated or falsified, I use [SOM-FFN](#) as the best estimate - still acknowledging the current limitations of pCO₂ in-situ data.

2.4 STATISTICAL METHODS

2.4.1 Linear trends and statistical tests

The main tool for analysis - linear trends - is the computation of a linear regression coefficient via least-squares. With Student's t-test, I check in spatial patterns whether this trend is significantly different to the null hypothesis (ch. 4) [Mood et al., 1974]. To exclude seasonal variability the climatological seasonality is removed from all monthly data before trend computation.

The Mann-Kendall test is a statistical tool to assess if there is a monotonic upward or downward trend of the variable of interest over time [Mann, 1945; Kendall, 1975]. This test is applied in sec. 3.1 to extract trends based on a selection criterion of monotony.

Monotonic upward means that it consistently increases over time. The Mann-Kendall test is best seen as an exploratory analysis and is used most appropriately to identify stations where changes are significant or of large magnitude [Hirsch et al., 1982].

The Mann-Kendall statistic S counts magnitude relations of each pair of all available timesteps in a dataset with the sign function:

$$S = \sum \text{sgn}(x_k - x_i).$$

This Mann-Kendall statistic S converts to probabilities for monotonic behavior according to Gilbert, 1987.

2.4.2 Choice of trends

To analyze the processes driving decadal internal variability σ_{DIV} (sec. 2.4.3) I focus on individual ensemble realizations as described later in ch. 3 and 4. Here I have to make a compromise between signal strength and robustness versus trend length. The longer a period, the more likely the trend deviates from a monotonic behavior, e.g. after a few years of monotonic increase the trend flips (fig. 3.2). Therefore longer trends show less chance to have a strong signal per trend-length (fig. A2). Also, longer trends experience a stronger influence of atmospheric forced trend. Furthermore, the underlying mechanisms for CO₂ flux trends in our ensemble simulation seem to be of the same origin regardless of the exact length of the trend period. Therefore, I decided to select 8-year trends in ch. 3 to understand the trending processes in ch. 4, because 8-year trends are still very close to decadal 10-year trends and still able to show similar magnitude and monotonic behavior as the observation-based estimate. Monotonic behavior is maintained by a Mann-Kendall test above a probability threshold of 0.98 ($S_{\text{threshold}} \leq 16$), which does not require strictly monotonic behavior but allows few deviations.

2.4.3 Decadal internal variability

Internal variability is present on many timescales. To investigate decadal internal variability I assess the differences of the annual mean state in a decade. For that I define decadal internal variability σ_{DIV} of any variable X as the standard deviation of the changes in M running multi-year (specifically 8-year) periods or decades in all N ensembles:

$$\sigma_{DIV}(X) = \sqrt{\frac{1}{MN} \sum_{n=ens}^N \sum_{m=yr}^M (x_{m,n} - \bar{x}_{m,n})^2} \quad (2)$$

$$x_{m,n} = X_{\text{decade}_{\text{end},n}} - X_{\text{decade}_{\text{start},n}}$$

I use values of the annual values to filter out seasonal variability and set the turn of the year to the end of July to fully capture one austral summer season allowing in-depth analysis for trends in biology.

Previous studies assume Gaussian statistics but lack an adequate ensemble size to check for in detail [Deser et al., 2012; Thompson et al., 2015]. The Max Planck Institute-Earth System Model Large Ensemble ([MPI-ESM LE](#)) used for this study includes 100 members. Furthermore, I increase my sample size and calculate trends in running intervals between 1980 and 2004, so strictly speaking internal variability is defined here in ensemble space and temporal space, which should not differ much over this period of 25 years.

The temporal distribution of the spatially integrated sum of the Southern Ocean south of 35°S ([fig. A1a](#)) as well as of a single randomly chosen grid cell in the Southern Ocean CO₂ flux ([fig. A1b](#)) follow Gaussian statistics. Assuming this also for other variables allows me to use the standard deviation as a metric and interpret those as probabilities.

2.5 CLIMATOLOGICAL METHODS

2.5.1 Southern Annular Mode Index

The Southern Ocean westerly winds are variable in strength and location. To describe this variability the Southern Annular Mode ([SAM](#)) index was defined by Gong and Wang, 1999. To construct the index I remove the climatological seasonal cycle from the maps of sea-level pressure and take a zonal mean of the latitudes 40°S and 65°S, standardize them against the climatological period of 1950-1979 as P* and take the difference to create the index value:

$$SAM = P_{40^\circ S}^* - P_{65^\circ S}^*$$

2.5.2 Thermal separation

In order to separate the influence of temperature on CO₂ flux I apply the methodology of Takahashi et al., 1993; Takahashi et al., 2002. The thermal component pCO_{2,thermal} accounts for the effect of changes in sea-surface temperature (SST) on pCO₂ whereas the non-thermal component pCO_{2,non-thermal} approximately accounts for all other changes.

$$pCO_{2,thermal} = \overline{pCO_2} \cdot \exp [0.0423^{\circ}C^{-1} (\bar{T} - T)] \quad (3)$$

$$pCO_{2,non-thermal} = pCO_2 \cdot \exp [0.0423^{\circ}C^{-1} (\bar{T} - T)] \quad (4)$$

The overbar indicates the temporal average.

3

MODEL EVALUATION IN THE SOUTHERN OCEAN

My analysis of the internal variability of the Southern Ocean carbon sink originates in the evaluation of air-sea CO₂ flux ([sec. 3.1](#)). As the strength of the CO₂ flux in the Southern Ocean is modulated by the strength of westerly winds [Lovenduski et al., [2007](#)], I assess also the sea-level pressure fields ([sec. 3.2](#)) as well as biology ([sec. 3.3](#)) and upper-ocean circulation, which respond to changes in wind ([sec. 3.4](#)).

A previous model evaluation of **HAMOCC** for the Coupled Model Intercomparison Project 5 (**CMIP5**) provides a global view on biogeochemistry [Illyina et al., [2013](#)]. In this chapter I evaluate the model focusing on the Southern Ocean and specifically the processes related to the carbon sink. In each subsection I compare the modeled mean state of the Southern Ocean to observational data and assess modeled decadal internal variability in spatial distribution and temporal evolution.

3.1 CO₂ FLUX

The patterns of CO₂ flux are mainly controlled by primary production (see in detail [sec. 3.3](#)) and advective transport of **DIC** and alkalinity (see in detail [sec. 3.4](#)). Ekman suction, also referred to as upwelling, drives outgassing and Ekman subduction, also referred to as downwelling, drives CO₂ uptake or ingassing. Positive values in sea-air CO₂ flux indicate outgassing and negative values CO₂ uptake by the oceans.

The climatological ensemble mean state from 1980 to 2004 of the Southern Ocean CO₂ flux in **MPI-ESM** marks the Antarctic coastal region is a CO₂ sink, whereas the upwelling waters in the Atlantic and Indian sector at 50–60°S are outgassing regions and CO₂ flux neutral in the Pacific ([fig. 3.1a](#)). North of 50°S, the oceans take up CO₂ because of stronger primary production and Ekman subduction.

The observational-based estimate **SOM-FFN** shows similar patterns of carbon uptake and outgassing but in lower absolute values ([fig. 3.1c](#)). Hardly any measurements in the region of seasonal ice cover make a comparison with observation-based values hard to interpret.

For spatial distributions I define decadal internal variability σ_{DIV} as the standard deviation over the changes in decades in the whole ensemble ([sec. 2.4.3](#)).

The region 45-60°S is most variable and characterized by upwelling ([fig. 3.8a](#)) and the southern edge of primary production ([fig. 3.5a](#)). The change in latitudinal position and strength of the westerly winds affects the position and amplitude of upwelling ([sec. 3.4](#)) and primary production ([sec. 3.3](#)).

The observation-based **SOM-FFN** decadal variability σ_{DIV} is most pronounced at 50-60°S in the Atlantic and Indian and south of 60°S in the Pacific [Landschützer et al., 2016]. The amplitude of decadal variability is smaller than in **MPI-ESM** ([fig. 3.1d](#)). However, this comparison is limited by large differences in sample size between the 22-year observational record and the 100 **MPI-ESM** realizations.

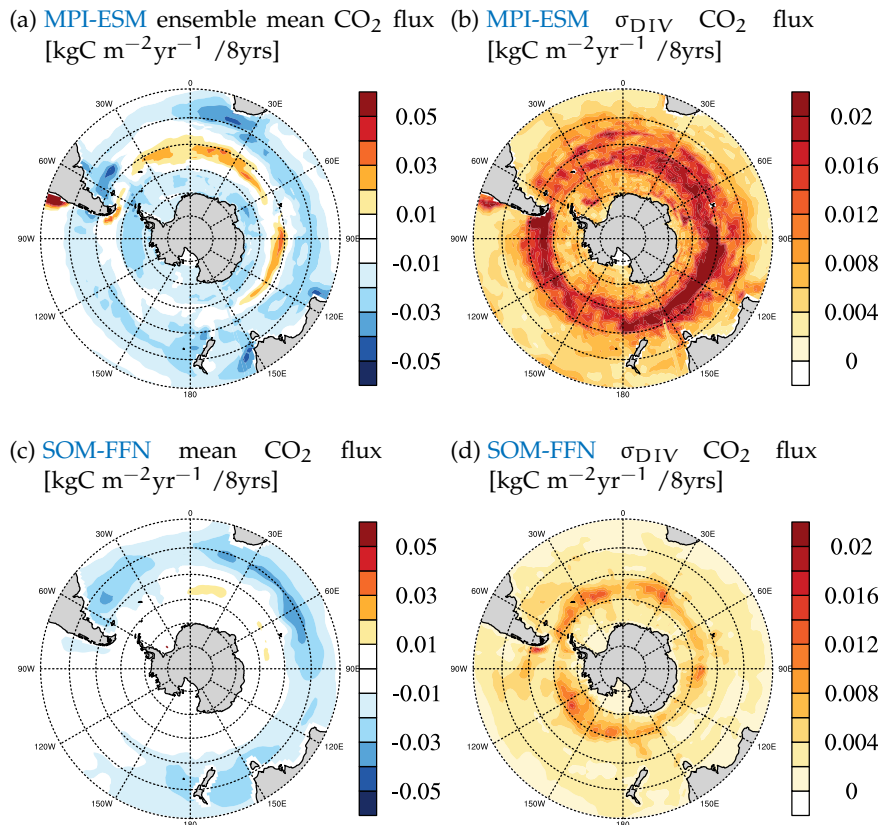


Figure 3.1: Spatial distribution of the climatology (a,c) and decadal internal variability σ_{DIV} (b,d) from 1980-2004 of the Southern Ocean sea-air CO₂ flux: (a) **MPI-ESM LE** ensemble mean as forced signal, (b) ensemble decadal standard deviation as decadal internal variability σ_{DIV} , (c) **SOM-FFN** climatology 1982-2004, (d) **SOM-FFN** decadal variability σ_{DIV} ; negative values indicate ocean uptake.

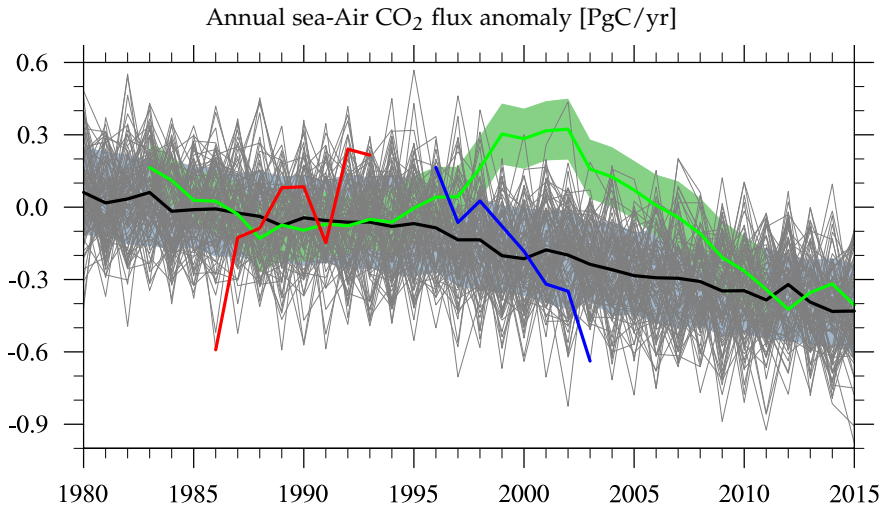


Figure 3.2: Temporal evolution of the Southern Ocean sea-air CO₂ flux anomaly south of 35°S with respect to the 1980s. Grey lines show the 100 ensemble members, the black line the ensemble mean, the blue shading is the ensemble decadal internal variability σ_{DIV} , the red line shows the most positive 8-year trend, the blue line shows the most negative 8-year trend, the green line represents the [SOM-FFN](#) observation-based estimate [Landschützer et al., 2015]; negative values indicate carbon uptake; [MPI-ESM LE](#) is extended under [RCP4.5](#) forcing from 2005 to 2015.

The temporal evolution of the Southern Ocean ensemble mean CO₂ flux south of 35°S is dominated by the forced negative trend of rising atmospheric CO₂ concentrations (fig. 3.2). Still, no individual realization follows the negative trend strictly monotonic - they oscillate around the ensemble mean state triggered by internal variability. Exemplary, the most extreme monotonic positive and negative 8-year trend is highlighted. The modeled ensemble mean sea-air CO₂ flux over the historical period 1980-2004 is ~ -1.15 PgC/yr and decadal internal variability σ_{DIV} is $\sim \pm 0.19$ PgC/yr/decade, larger than the forced signal of ~ -0.14 PgC/yr/decade, which reflects the mean of decadal changes. Tab. 3.1 shows an overview the statistical quantities related to Southern Ocean carbon sink variability.

The observational-based estimate for the whole region south of 35°S shows a strong positive CO₂ flux trend in the 1990s and a strong negative trend reinvigorating the carbon sink in the 2000s [Landschützer et al., 2015] (fig. 3.2). The modeled σ_{DIV} is lower than of decadal variations in [SOM-FFN](#) (tab. 3.1). This means that on multi-year time-scales [SOM-FFN](#) is 50% more variable than [MPI-ESM LE](#). This comparison must be ingested with caution as influent datasets differ in ensemble-space. [SOM-FFN](#) would rank as one exceptionally variable 22-year realization into [MPI-ESM LE](#).

dataset	trend length [TL]		8-yr trend		10-yr trend	
	MPI-ESM	SOM-FFN	MPI-ESM	SOM-FFN	MPI-ESM	SOM-FFN
mean state [PgC/yr]	-1.15	-0.87	-1.15	-0.87		
σ_{DIV} [PgC/yr/TL]	± 0.22	± 0.35	± 0.19	± 0.30		
forced signal [PgC/yr/TL]	-0.11	/	-0.14	/		
positive trend [PgC/yr/TL]	+0.70	+0.38	+0.53	+0.39		
corrected trend [PgC/yr/TL]	+0.81	+0.49	+0.67	+0.53		
probability [%]	0.01	20	0.1	10		
negative trend [PgC/yr/TL]	-0.78	-0.53	-0.74	-0.66		
corrected trend [PgC/yr/TL]	-0.67	-0.39	-0.60	-0.52		
probability [%]	0.3	25	0.3	10		

Table 3.1: Overview of statistical quantities in two trend lengths [TL] in sea-air CO₂ flux in the Southern Ocean south of 35°S from Max Planck Institute-Earth System Model Large Ensemble ([MPI-ESM LE](#)) and Self-Organizing Map-Feed-Forward Network ([SOM-FFN](#)) [[Landschützer et al., 2015](#)]; positive and negative trends are the most extreme trends in each dataset; the forced signal is subtracted off the corrected trends; probabilities quantify the likelihood that corrected trends are due to internal variability; 8-yr trends are required to be monotonic.

The decadal variability σ_{DIV} in [SOM-FFN](#) data is ~ 0.30 PgC/yr/decade, with the most positive CO₂ flux trend in the 1990s of $\sim +0.39$ PgC/yr/decade and the most negative trend of ~ -0.66 PgC/yr/decade. Compared to [SOM-FFN](#)'s σ_{DIV} , both observation-based trends corrected for the modeled forced signal get an attribution to internal variability of $\sim 10\%$ ($\sim 1.6\sigma$). Under the context of [MPI-ESM LE](#)'s σ_{DIV} these magnitudes in observation-based trends could be due to internal variability with probabilities of 1% ($\sim 2.6\sigma$) for 1990s and 2000s trends respectively. This outlines the low likelihood of these [SOM-FFN](#) CO₂ flux trends attributed to internal variability from the perspective of numerical modeling with perturbed initial conditions (tab. 3.1).

As [MPI-ESM LE](#) simulations are forced with prescribed atmospheric CO₂ concentrations, the modeled internal variability of an interactive carbon cycle would be a more realistic counterpart for the observed internal variability. The non-linear changes in atmospheric CO₂ concentrations due to the interplay of the oceanic and terrestrial carbon cycle result in 25% higher internal variability [[Illyina et al., 2013](#)].

Applying the selection criteria from sec. 2.4.2 I focus on the two highlighted extreme CO₂ flux trends with monotonic behavior (fig. 3.2). For decadal 10-year trends the most extreme cases are of the same magnitude ($\sim +0.5$ PgC/yr/decade and ~ -0.7 PgC/yr/decade) as those derived from observation-based estimates in the 1990s and 2000s

[Landschützer et al., 2015] (fig. A2). The processes related to decadal and multi-year trends only differ in monotony. Longer trends are more strongly exposed to the forced trend and likely dominated strong short-term variability and hence do not persist as long. In the following I always also analyze the drivers of two distinct 8-year trends. The most positive monotonic 8-year air-sea CO₂ flux trend from 1985 to 1992 in ensemble 78 reaches $\sim +0.5$ PgC/yr/8yrs and the most negative monotonic 8-year trend from 1995 to 2002 in ensemble 143 reaches ~ -0.6 PgC/yr/8yrs.

3.2 WINDS

Winds are governed by distributions in sea-level pressure ([SLP](#)). They point from high pressure to low pressure systems, but get diverted to their left in the Southern Hemisphere by the Coriolis force. Therefore, strong westerly winds are established between the low-pressure system south of 45°S and higher pressure systems over the subtropical gyres ([fig. 3.3a](#)). This zonally symmetric [SLP](#) pattern in the ensemble climatological mean leads to zonally symmetric westerly winds peaking at 50°S.

The spatial zonal distribution in observational data of a reanalysis climatology from National Centers for Environmental Prediction ([NCEP](#)) is so similar to the [MPI-ESM LE](#) climatology that I plot the difference between [MPI-ESM LE](#) climatology and [NCEP](#) reanalysis [Kalnay et al., 1996] ([fig. 3.3c](#)). The position of the jets in [ECHAM](#) is shifted to lower latitudes [Stevens et al., 2013] which seems to be a common atmospheric modeling challenge [Kidston and Gerber, 2010]. Therefore, the modeled westerlies are too strong from 30-60°S and too weak south of 60°S. The zonal wind speed difference peaks at 45°S at +1m/s.

The decadal internal variability σ_{DIV} increases zonally towards lower latitudes with the highest internal decadal variability in the pacific sector in the Southern Ocean seasonal ice-covered area ([fig. 3.3b](#)).

Observational reanalysis data reveal the same spatial distribution with a higher amplitude of decadal internal variability ([fig. 3.3d](#)). The pacific sector reflects the area of an Antarctic dipole induced from the El Niño-Southern Oscillation ([ENSO](#)), which manifests itself in variability of sea-ice [Yuan, 2004]. This is also known as the Pacific-South American (PSA) Oscillation [Sallée et al., 2008]. The atmospheric Southern Ocean jet splits and in El Niño conditions intensifies on a northern route inducing a low pressure system with more storms. La Niña conditions bring a high pressure system with less storms vice versa. Such tele-connections of the tropics into the Southern Ocean are subject of current research and have been rarely analyzed yet for the Southern Ocean carbon sink.

The temporal evolution and internal variability of the annual [SAM](#) index calculated according to [Gong and Wang, 1999] ([sec. 2.5.1](#)) is shown in [fig. 3.3](#). Positive [SAM](#) index values are associated with an anomalously low [SLP](#) over Antarctica that result in a southward-shift and intensification of westerly winds. The [MPI-ESM](#) ensemble mean has a positive trend as a consequence to anthropogenic CO₂ emissions and ozone depletion over Antarctica [Thompson et al., 2011].

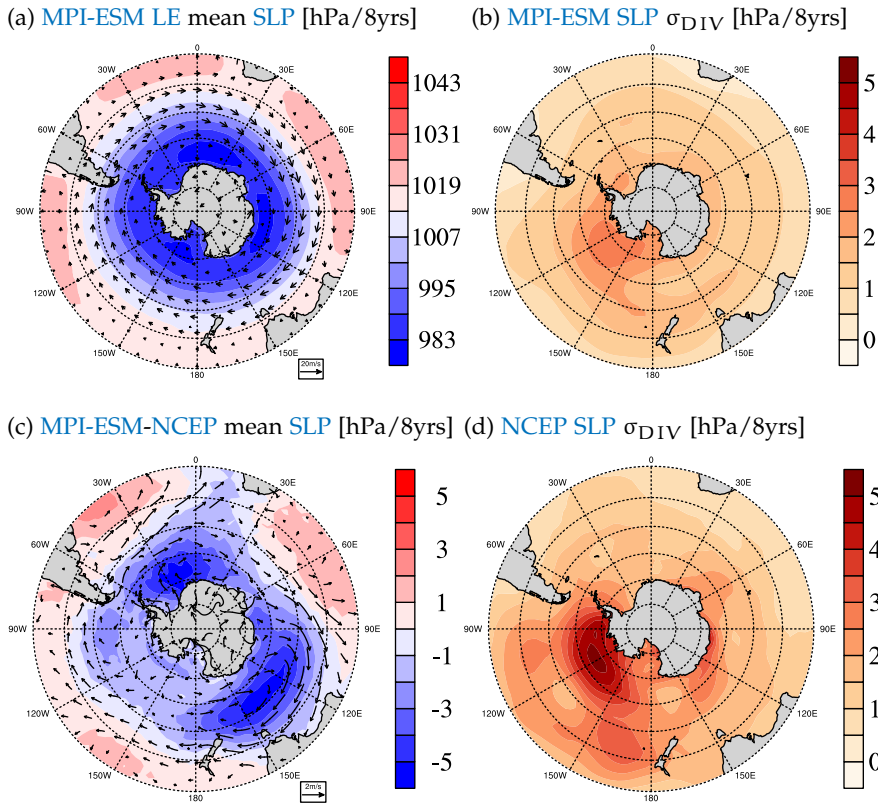


Figure 3.3: Spatial distribution of the Southern Ocean sea-level pressure (SLP) and wind vectors overlain as arrows: (a) MPI-ESM ensemble mean climatology from 1980 to 2004 as forced signal, (b) ensemble decadal standard deviation as decadal internal variability σ_{DIV} ; (c) difference between MPI-ESM and reanalysis data from NCEP reanalysis climatology [Kalnay et al., 1996], (d) decadal internal variability σ_{DIV} from NCEP reanalysis climatology.

MPI-ESM LE SAM index lies in the range of the observational station-based SAM index from [Marshall, 2003], although it follows a weaker trend in the ensemble mean.

The positive CO₂ flux trend shows a positive trend in SAM. Those strengthening winds increase upwelling (sec. 3.4), which brings over-saturated waters to the surface and hence leads to outgassing anomalies. This weakens the carbon sink and vice versa strengthens the carbon sink under the context of weakening westerly winds. The detailed response of primary production and advective transports under the context of changing winds is discussed in detail later in ch. 4.

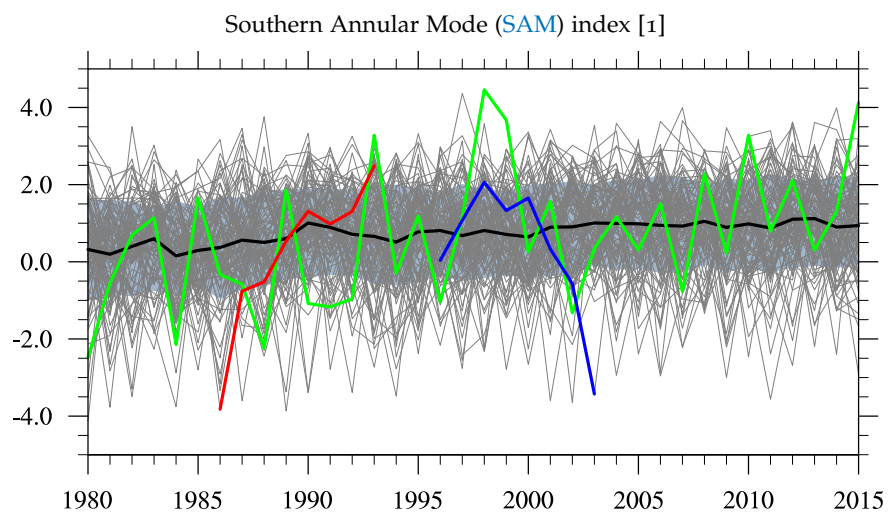


Figure 3.4: Temporal evolution of the annual Southern Annular Mode (SAM) index according to [Gong and Wang, 1999]. Grey lines show the 100 ensemble members; the black line the ensemble mean; the blue shading is the decadal internal variability σ_{DIV} ; the red line represents the SAM during positive sea-air CO₂ flux trend; the blue line during the negative CO₂ flux trend; the green line shows the station-based SAM from Marshall, 2003.

3.3 BIOLOGY

The strong seasonal cycle in insulation and the sparseness of land topography leads to first-order zonally symmetric constraints for light and [SST](#). The high-latitude Southern Ocean is a so-called high nutrient low chlorophyll (HNLC) region, where light is the dominant limiting factor for the low biological production but nutrients are plenty [Falkowski et al., 1998]. Summer sea-ice cover and sub-zero [SST](#) values constrain plankton growth and is responsible for the tiny amount of primary production in the coastal areas as well as the Ross Sea and Weddell Sea.

With decreasing latitude in the Southern Ocean, primary production increases along with increasing temperatures and light availability. Nutrients are upwelled by the upper-ocean overturning circulation and advected northwards by Ekman transport. This latitudinal increase of primary production peaks at 40-50°S, where nutrients are abundant from upwelling and Ekman transport and higher temperatures and light availability foster phytoplankton growth rates. The mixing with warm subtropical waters off the Argentinian coast increases [SST](#) and leads to a maximum primary production in the Southern Ocean [Behrenfeld, 2014]. Downstream the Drake passage, the polar front with its cold waters extends more northward [Orsi et al., 1995]. Along with lower nutrient concentrations due to increased precipitation from storms it explains the relatively low primary production in the Atlantic sector compared to other longitudinal counterparts. At the subtropical front decreasing nutrient concentrations limit primary production [Behrenfeld, 2014] ([fig. 3.5](#)).

To evaluate [HAMOCC](#)'s ability to model the Southern Ocean, I do not compare modeled primary production to chlorophyll-a concentration derived from satellite data, because satellite images are frequently hidden by clouds. Instead, I compare the distributions of nitrate which is the limiting nutrient for biological production in this [HAMOCC](#) version. The distribution of nitrate shows a strong gradient in [HAMOCC](#) as well as in the World Ocean Atlas ([WOA](#)) 2013 [Garcia et al., 2013] along the fronts from plentiful of nutrients in the high-latitudes to nutrient depletion in the subtropical gyres ([fig. 3.6](#)). In higher latitudes [HAMOCC](#) underestimates the phosphate concentration by 25%. These lower nutrient concentrations can be a sign of more nutrient consumption at higher primary production or be the reason for lower primary production. The distribution of another important nutrient phosphate shows a similar spatial pattern ([fig. A5](#)).

Internal decadal variability in vertically integrated primary production in the Southern Ocean is higher in high productivity areas ([fig. 3.5b](#)). The whole region at 45-60°S, especially in the Indian sector,

shows a enormously high decadal internal variability σ_{DIV} relative to the ensemble mean state. Internal variability in the Southern Hemisphere is mostly driven by westerly winds. The explicit effect of those on HAMOCC is discussed in ch. 4.

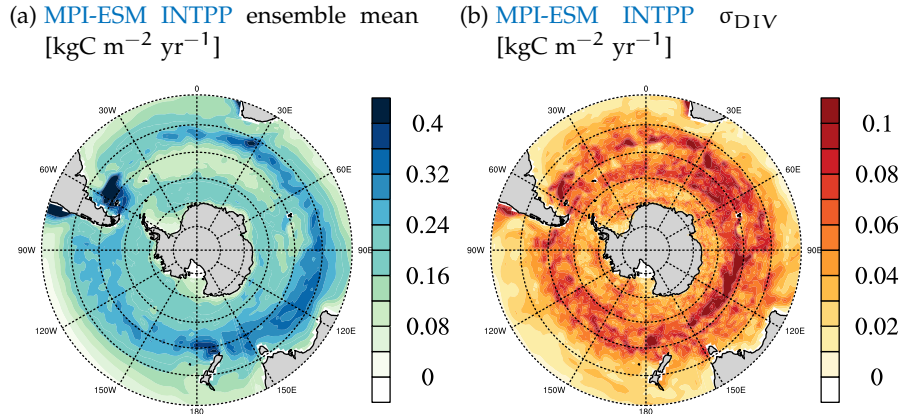


Figure 3.5: Spatial distribution of the vertically integrated primary production in the Southern Ocean: (a) climatological MPI-ESM ensemble mean from 1980 to 2004 as forced signal and (b) ensemble decadal anomaly standard deviation as decadal internal variability σ_{DIV} .

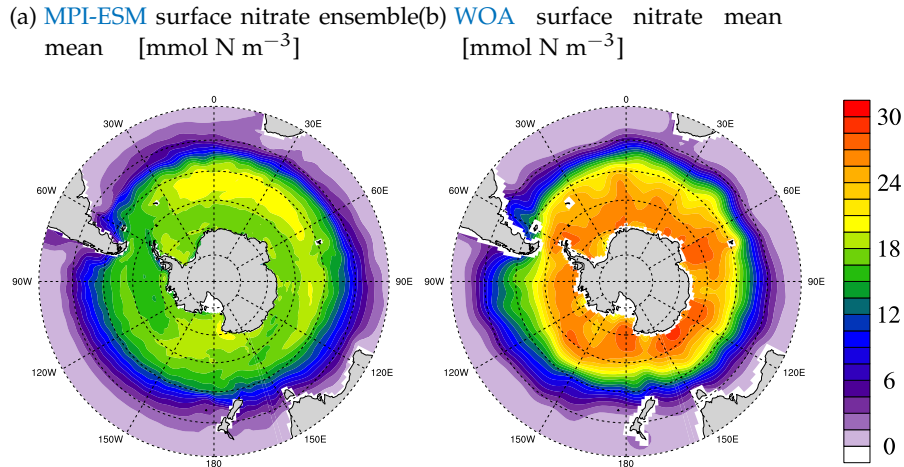


Figure 3.6: Spatial distribution of surface nitrate in the Southern Ocean: (a) MPI-ESM ensemble mean climatology, (b) World Ocean Atlas (WOA) climatology data [Garcia et al., 2013].

Regarding the temporal evolution in the Southern Ocean, primary production is not subject to a strong forced trend in the historical period but varies internally (fig. 3.7). The weak decreasing trend might be the first sign of increased stratification due to sea-surface warming, which in turn inhibits the mixing of nutrients. But the long-term

consequences for primary production is subject to ongoing research and debate [Bopp et al., 2013; Taucher and Oschlies, 2011; Lozier et al., 2011; Kessler and Tjiputra, 2016; Krumhardt et al., 2017; Depecker and Davidson, 2017]. The decadal internal variability σ_{DIV} is 0.5 PgC/yr/decade.

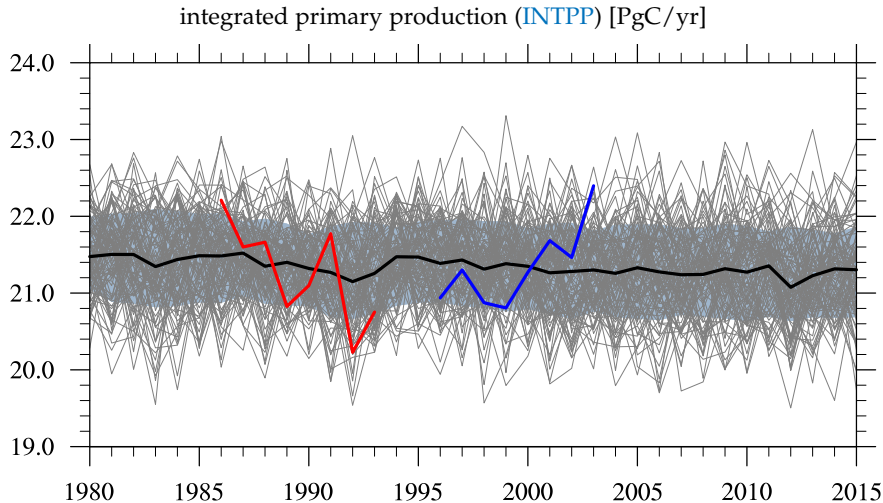


Figure 3.7: Temporal evolution of the integrated primary production (INTPP) in the Southern Ocean south of 35°S. Grey lines show the 100 ensemble members, the black line the ensemble mean, the blue shading is the decadal internal variability σ_{DIV} , the red line shows ITPP during the positive CO₂ flux trend, the blue line during the negative CO₂ flux trend.

The absolute amount of primary production exceeds CO₂ flux by a factor of ~20. The spatial distribution of export flux at 90m, which is the particulate organic matter that sinks below the euphotic zone, is the same as for primary production. As a lower vertical boundary for a upper-ocean budget, export flux is of similar magnitude as CO₂ flux and thus comparable (ch. 5).

The negative CO₂ flux trend has a positive trend in primary production, because primary production lowers surface DIC, pCO_{2,ocean} and hence reduces CO₂ uptake by the ocean; and vice versa negative trends in primary production lead to positive CO₂ flux trends.

MPI-ESM is able to model the general features of the Southern Ocean, such as the characteristics of a high nutrient low chlorophyll region [Bopp et al., 2013]. But compared to other models and observational data, the seasonal cycle of phytoplankton blooms is amplified and too early in the Southern Ocean [Bopp et al., 2013; Neison et al., 2015; Neison et al., 2016]. The reason of this is under current debate in the MPI biogeochemistry research group. It could involve that the Southern Ocean in **MPI-ESM LE** runs is not iron-limited but while

changing the dust input fields and the iron cycling constants lead to an iron-limited Southern Ocean the amplified seasonality is still present [private Communication, Irene Stemmler (MPI, Hamburg)]. Also a look into the grazing of zooplankton and its variable formulation might lead to a more realistic primary production seasonality. Furthermore, the atmospheric bias in westerly winds and the Southern Ocean warm bias [Jungclaus et al., 2013] hinders sea-ice to propagate more extensively. A proper representation of Antarctic sea-ice would come along with a cooler, more stratified Southern Ocean which modulates primary production. But the amplified seasonality also occurs in the norwegian ESM NorESM which uses HAMOCC in a different ocean model, so revisiting seasonality in the high-latitude oceans remains a challenge in HAMOCC.

Additionally, the longest standing data records, which are on the northern hemisphere in Iceland [Six and Maier-Reimer, 1996], are used for the tuning of free model parameters. Historically, the Southern Ocean has never been in the focus of HAMOCC.

3.4 UPPER-OCEAN OVERTURNING CIRCULATION

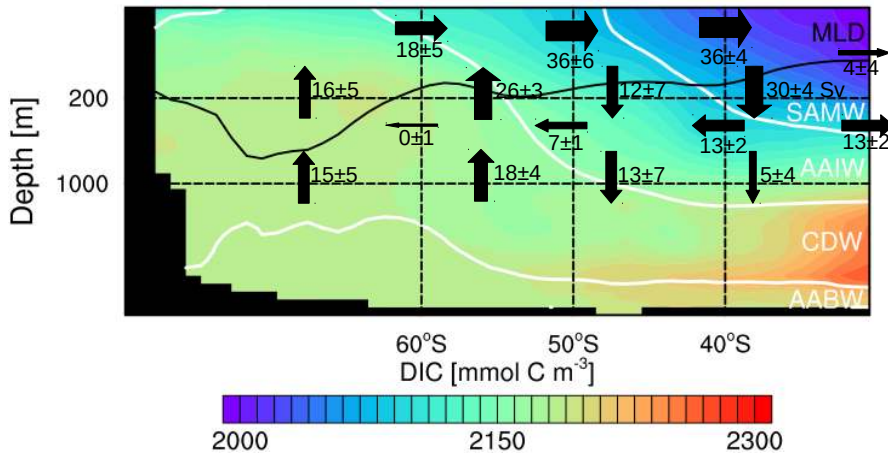
The Southern Ocean upper-ocean overturning circulation is driven by the divergence at 40-60°S corresponding to strong westerly winds (fig. 3.8a). The isopycnals, which separate water masses, orient themselves at values from Sallée et al., 2013b, but are shifted to fit to typical depths, which is a common feature in water mass comparison as models have different density biases [Sallée et al., 2013b]. In the high latitudes south of 50°S Ekman pumping brings Circumpolar Deep Water (CDW) from the ocean interior to the surface. At the surface these waters are transported to the north. At lower latitudes, the surface waters warm and evaporation increases, so relatively cold and low salinity waters known as Antarctic Intermediate Water (AAIW) slide below warmer and more saline Sub-Antarctic Mode Water (SAMW) to extend northwards at intermediate depth. This process is called downwelling or Ekman subduction.

The strong upper-ocean overturning circulation in the Southern Hemisphere features upwelling south of 50°S, northward transport at 40-60°S and downwelling at 30-40°S and is known as the Deacon cell [Döös and Webb, 1994; Speer et al., 2000]. The upper-ocean overturning circulation is driven by the strength and positions of westerly winds. Upwelling steepens and downwelling straightens the isopycnals along which the water masses flow [Marshall and Speer, 2012]. The internal variability in the horizontal processes at intermediate depth is lower than at the surface because the influence of winds decays with depth. The decadal internal variability σ_{DIV} of vertical Ekman pumping and subduction is of similar magnitude at 200m and 1000m (fig. 3.8).

Fig. 3.8a is similar to DeVries et al., 2017, fig. 1, which uses observational data in an inverse model to demonstrate changes in upper-ocean overturning circulation. Due to different vertical velocity regimes I choose different boundaries for the transport which prevents me from quantitative comparisons. Nevertheless, data of DeVries et al., 2017, fig. 1 show the main characteristics of the Deacon cell and water transport of comparable magnitude as in MPI-ESM LE.

How does the upper-ocean overturning circulation relate to the carbon cycle? The concentration of DIC in general increases with depth due to the biological pump and remineralization at depth. This is most clearly seen in the subtropics and blurred by processes of mixing at higher latitudes (fig. 3.8). Still, upwelled waters from the deep oceans have a high pCO₂ potential at which they would equilibrate when lifted to the surface, so the upwelling super-saturated waters in high latitude waters drives CO₂ outgassing and downwelling takes CO₂ equilibrated waters into the deeper ocean (fig. 3.8b) [Morrison

(a) MPI-ESM advective water transport [Sv]



(b) MPI-ESM advective carbon transport [PgC/yr]

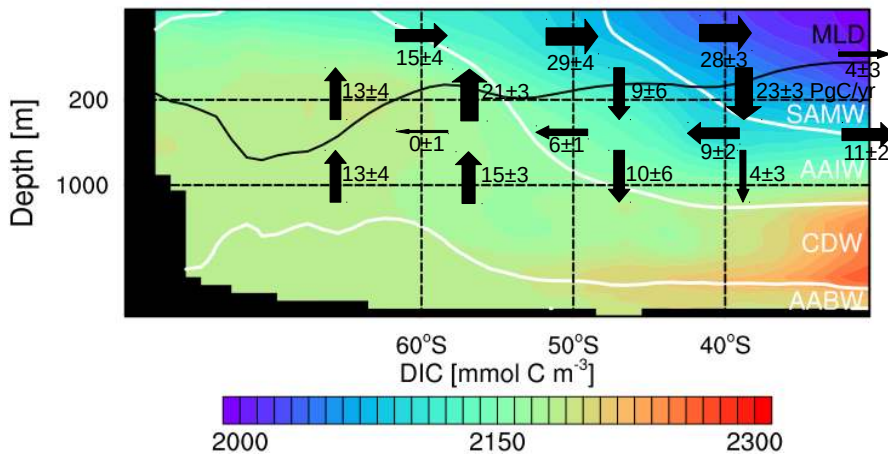


Figure 3.8: Zonally averaged transect of the Southern Ocean and the upper-ocean overturning circulation; black arrows show yearly mean advective transports and decadal internal variability (σ_{DIV}) of (a) water in Sv and (b) carbon in PgC/yr; white lines are isopyncals separating SAMW at potential density $\rho_\theta = 1026.5 \text{ kg m}^{-3}$ from AAIW, at $\rho_\theta = 1027.2 \text{ kg m}^{-3}$ from CDW, at $\rho_\theta = 1027.7 \text{ kg m}^{-3}$ from AABW; the black line is the MLD; the colored contours show the distribution of concentration in DIC.

et al., 2015].

During the positive CO₂ flux trend upper-ocean overturning circulation intensifies. This means enhanced upwelling, which weakens the carbon sink (fig. 4.10) and vice versa strengthens the carbon sink for weaker upper-ocean overturning circulation (fig. 4.5).

The global performance of MPIOM is discussed in detail in Jungclaus et al., 2013. The Southern Ocean SST warm bias is attributed to

an overestimation of downward shortwave radiation into the polar regions [Stevens et al., 2013] and causes the underestimation of sea-ice coverage. Additionally, the water-column stability is too low which allows open-ocean convection in the Ross and Weddell Sea and deeper than observed winter mixing. Additional freshwater input from melting glaciers distributed by icebergs improves the water-column stability, increases sea-ice and prevents open-ocean convection. A similar effect has the coupling to a higher resolved atmosphere due to additional freshwater input from circulation pattern changes [Stössel et al., 2015].

The model quality of overturning circulation in the Southern Ocean is analyzed by Sallée et al., 2013b. **MPI-ESM** realistically simulates subtropical water temperature and Sub-Antarctic Mode Water in general. But the overturning cell is much weaker than in other models.

The **MLD** is an important measure to assess how climate models represent the Southern Ocean. **MLD** in **MPI-ESM** is overestimated compared to observational data from **NOAA** Atlas [Monterey and Levitus, 1997] in the locations of the Antarctic Circumpolar Current (**ACC**) and the Ross and Weddell Sea (fig. 3.9) as well as in the zonal average (fig. 3.8). In the Ross and Weddell Sea the **MLD** deepens to few kilometers depth via open-ocean convection [Stössel et al., 2015], which often appears in climate models but rarely seen in observations [Heuzé et al., 2013; de Lavergne et al., 2014]. The weak stratification explains why **MPI-ESM** overestimates **MLD**; especially in winter [Sallée et al., 2013a].

(a) **MPI-ESM** MLD ensemble mean [m] (b) **NOAA** MLD Atlas mean [m]

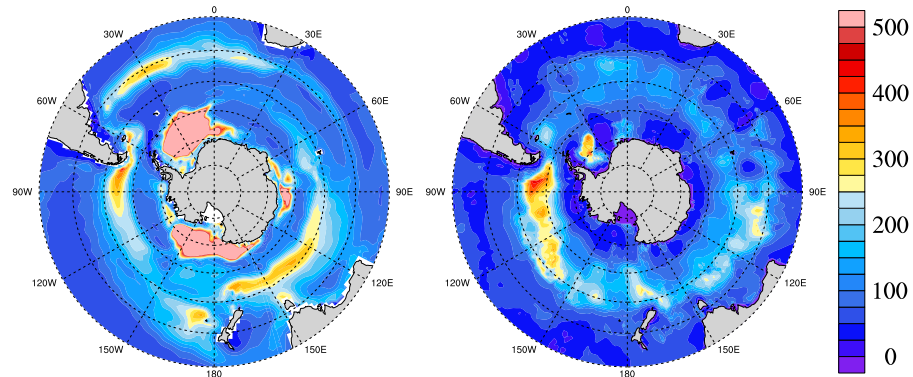


Figure 3.9: Spatial distribution of mixed-layer depth (**MLD**) in the Southern Ocean: (a) **MPI-ESM** ensemble mean climatology, (b) **NOAA** Atlas climatology [Monterey and Levitus, 1997].

4

PROCESSES CORRESPONDING TO MULTI-YEAR TRENDS IN SEA-AIR CO₂ FLUX

4.1 THE ROLE OF WESTERLY WINDS IN SOUTHERN OCEAN CO₂ FLUX VARIABILITY

Thompson and Wallace, 2000 and Hall and Visbeck, 2002 describe the Southern Annular Mode (**SAM**) as the most dominant mode for higher-latitude Southern Hemisphere variability. Lovenduski et al. [2007] explain the influence of the westerly winds on the Southern Ocean carbon sink.

To further assess internal variability due to westerly winds in **MPI-ESM** this chapter discusses the effect of westerly winds on the thermal, physical and biological controls of the Southern Ocean carbon sink in **HAMOCC**.

I find a correlation on 8-year trends between **SAM**, which describes the position and latitudinal shift of westerly winds, and the CO₂ flux in the area of largest decadal internal variability at 50-60°S (fig. 4.1). Although the CO₂ flux formula (sec. 2.1.3) also depends on the wind speed at 10m height, the driver of the changes in fig. 4.1 is not the piston velocity k_w , but in $\Delta p\text{CO}_2$ [Lovenduski et al., 2015]. However, the magnitude of short-term variability on the timescale of days to hours depends highly on wind strength variability whereas the direction of CO₂ flux is independent of wind speed. This relationship reveals two distinct regimes of wind-driven CO₂ flux signals in this area:

Intensified and southward-shifted winds, associated with an increasing trend in **SAM**, lead to a positive CO₂ flux trend. This Southern Ocean carbon sink response has been suggested frequently for the observed and projected trend in **SAM** [Le Quéré et al., 2007; Lovenduski et al., 2007; Lovenduski et al., 2008; Hauck et al., 2013; Landschützer et al., 2015]. The related process responses corresponding to stronger winds are explained in sec. 4.2.

In **MPI-ESM** I also find the reverse case of weakening and northward-shifting westerly winds, associated with a negative trend in **SAM**, which lead to a negative CO₂ flux or ocean uptake trend. The responses of processes corresponding to weaker winds are explained in sec. 4.3. However, observations do not reveal a strong multi-year negative **SAM** trend (fig. 3.4). Likewise, westerly winds did not weaken but continued to increase during the negative CO₂ flux trend in the 2000s [Landschützer et al., 2015]. On the contrary, depending on the

starting year of the trend period, the **SAM** index slightly weakened in the early 2000s [Marshall, 2003; Lovenduski et al., 2015], and also DeVries et al., 2017 report a decline in upper-ocean overturning circulation which may be connected to strength and position of winds.

The strong trends originate in strong changes of the position and strength of Southern hemisphere westerly winds and effect of those on ocean circulation. Though the parametrized eddies in **MPI-ESM LE** might allow deeper mixing to sustain for multiple years and hence longer than the seasonal timescale at which the eddies would counteract those trends [Thompson et al., 2011]. Only a variable definition of isopyncal thickness diffusion could parametrize the expected eddy response from high-resolution simulations [Gent and Danabasoglu, 2011]. These enhanced eddy fluxes in a low-resolution model are discussed in Lovenduski et al., 2013.

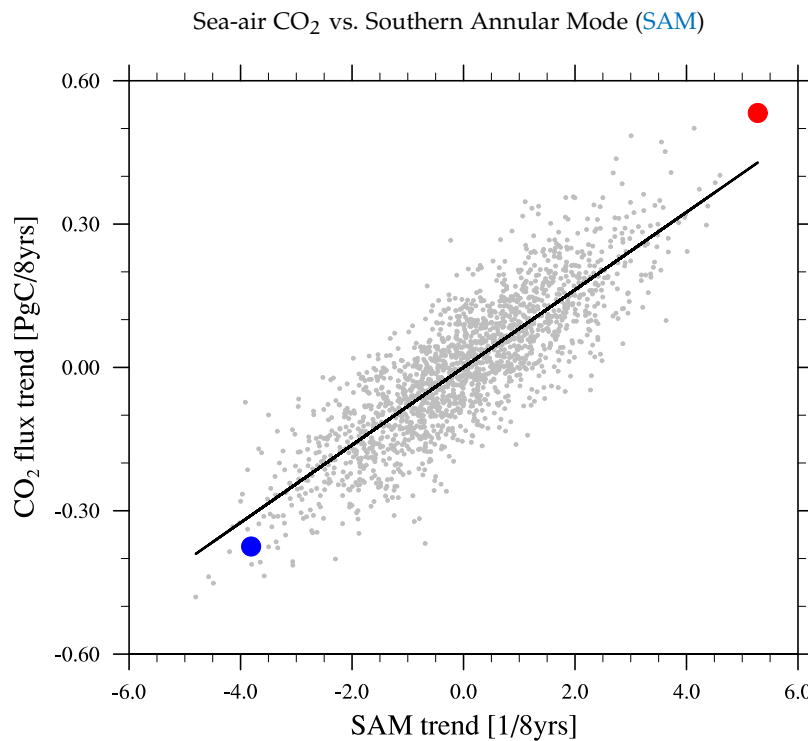


Figure 4.1: Linear trends in the **SAM** as indicator of wind strength vs. sea-air CO₂ flux at 50–60°S; each data point represents 8-year trends of a single realization normalized for the ensemble mean trend between 1980 and 2004; the blue dot represents the most negative monotonic CO₂ flux trend; the red dot the positive monotonic CO₂ flux trend.

To qualitatively understand the mechanisms of the Southern Ocean carbon sink I analyze the drivers of CO₂ flux on a process level. This chapter covers qualitative CO₂ flux changes with respect to the ther-

mal effect, physical circulation and biology. A quantitative analysis of the different drivers for different regions follows in [ch. 5](#).

The analysis presented here involves 8-year trends for reasons stated in [sec. 2.4.2](#) but the results of this chapter apply to various multi-year and decadal trends subject to internal variability (not shown).

The spatial trend patterns of different trend periods mostly appear zonally symmetric, therefore the analysis is not separated into the different Southern Ocean sectors, e. g. in the Pacific, Indian or Atlantic sector. Also, the atmospheric circulation change in [MPI-ESM](#) is too symmetric compared to observations [Haumann et al., 2014]. Therefore, the description here is carried out in zonal latitudinal bands keeping the unsymmetrical Southern Ocean dynamics in mind [Sal-lée et al., 2010; Talley, 2013]. Also due to the underestimated Antarctic sea-ice and open-ocean convection in the Ross and Weddell Sea, I restrict my analysis to the Southern Ocean north of 60°S, but the decadal CO₂ flux trends have a weak signal south of 60°S anyway.

4.2 POSITIVE CO₂ FLUX TRENDS

Strong positive CO₂ flux trends correlate with stronger westerly winds (fig. 4.1) [Lovenduski et al., 2007]. The difference $\Delta p\text{CO}_2$ between oceanic pCO_{2,ocean} and atmospheric partial pressures pCO_{2,atm} depicts a cleaner signal than CO₂ flux (fig. 4.2a,4.2b) and is independent of wind speed and solubility [Lovenduski et al., 2015]. pCO_{2,ocean} rises stronger than pCO_{2,atm}, so CO₂ must be driven by changes in the ocean dynamics (fig. 4.2b). The strongest positive signal occurs in the upwelling at 50–60°S, a weaker and more patchy signal occurs in the subduction areas north of 50°S, whereas changes in most other areas of the Southern Ocean are insignificant (fig. 4.2b).

Westerly winds decrease at 40–50°S and increase at 50–60°S, which results in a southward shift of westerlies (fig. 4.2c) represented by the positive trend in SAM (fig. 3.4).

The response of the thermal effect, upper-ocean overturning circulation and biology are described in sec. 4.2.1, 4.2.2 and 4.2.3, respectively.

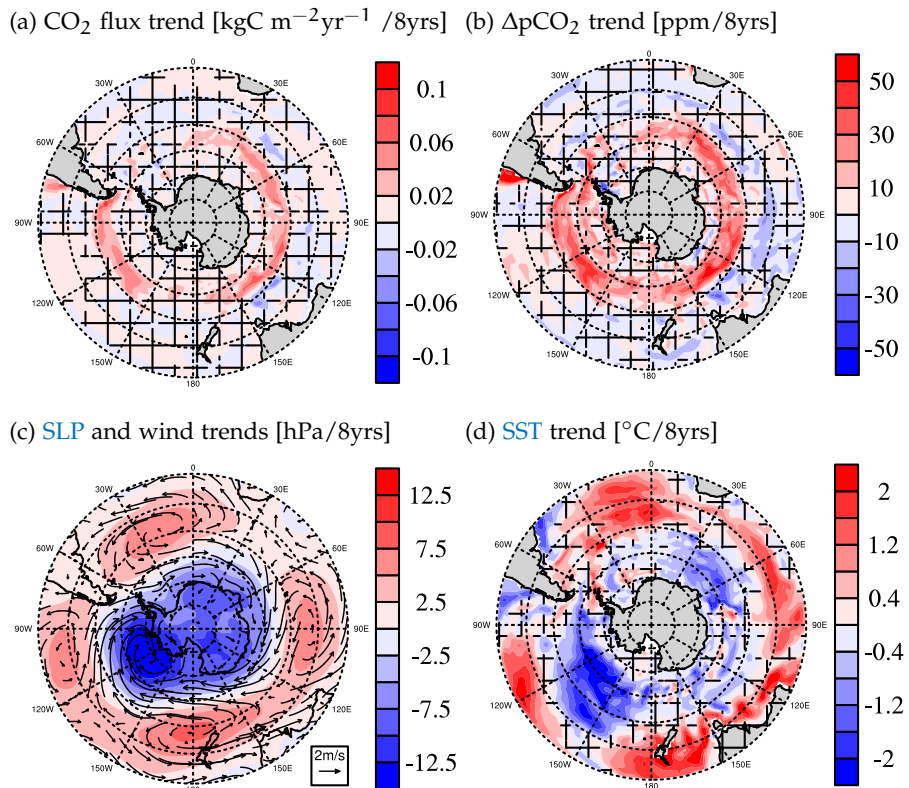


Figure 4.2: Linear trends during the most positive monotonic 8-year sea-air CO₂ flux trend: (a) sea-air CO₂ flux, (b) $\Delta p\text{CO}_2$, (c) SLP and wind vectors overlain as arrows and (d) sea-surface temperature (SST); hatched areas indicate where trends are outside the 5% significance level.

4.2.1 Changes in the thermal effect during positive CO₂ flux trends

The solubility of pCO_{2,ocean} is primarily sensitive to sea-surface temperature (SST). Warmer oceans such as the tropical oceans own a lower solubility than cooler high-latitude oceans - a process referred to as the solubility pump of carbon [Volk and Hoffert, 1985]. Likewise, CO₂-equilibrated waters outgas when warmed and take up CO₂ when cooled.

The difference between the partial pressure of CO₂ in the ocean (pCO_{2,ocean}) and the atmosphere (pCO_{2,atm}) is the main changing quantity in the CO₂ flux formula [Lovenduski et al., 2015] (eq. 1). The separation by Takahashi et al. [1993, 2002] gives insights about the direct influence of SST (sec. 2.5.2). The thermal pCO₂ trend is driven by changes in SST (fig. 4.3a), whereas the non-thermal ΔpCO₂ trend approximates all other changes in pCO_{2,atm}, biology, alkalinity, assuming constant SST (fig. 4.3b). The thermal pCO₂ trend and non-thermal ΔpCO₂ trend approximately add up to the trends in pCO₂ [Landschützer et al., 2015]. The thermal trend follows the SST cooling trend (fig. 4.2d) south of 50°S towards negative CO₂ flux trends, whereas the warming north of 50°S favors outgassing. Increased Ekman transport causes this heat divergence in polar regions and a heat convergence at lower latitudes [Hall and Visbeck, 2002] (fig. 4.5). The non-thermal component strongly increases south of 50°S, so overall the pCO_{2,ocean} increases faster than pCO_{2,atm} leading to a positive sea-air CO₂ flux trend. The non-thermal and thermal trends combined nearly compensate north of 50°S but at 50-60°S the outgassing dominates (fig. 4.2b). The homogenous increase in atmospheric pCO_{2,atm} accounts for a -12 ppm/8yrs in ΔpCO₂ (fig. 4.2b). These changes are stronger in the summer season, especially the non-thermal component because of the stronger summer SLP trend (fig. A7, A8).

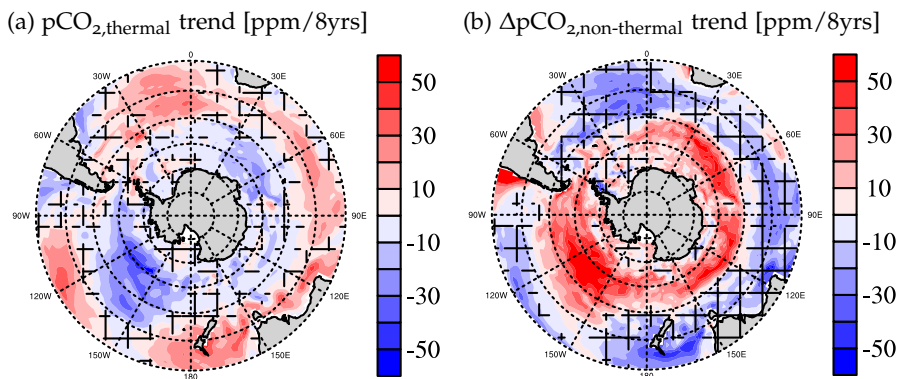


Figure 4.3: Linear trends during the most positive monotonic 8-year sea-air CO₂ flux trend: (a) pCO_{2,thermal} and (b) ΔpCO_{2,non-thermal}; hatched areas indicate where trends are outside the 5% significance level.

4.2.2 Changes in ocean circulation during positive CO₂ flux trends

Stronger westerly winds intensify the upper-ocean overturning circulation [Lauderdale et al., 2013]. Therefore the circulation field advects more DIC and alkalinity along its overturning pathway (fig. 4.5). Intensified upwelling of super-saturated waters at 50-60°S increase DIC and alkalinity concentrations in the euphotic zone (fig. 4.4b). As the pCO_{2,ocean} sensitivity of DIC is larger than for alkalinity, this likely enhances pCO_{2,ocean}, which leads to a positive CO₂ flux (for a detailed discussion see ch. 5). The stronger winds also increase Ekman northward transport and advects DIC and alkalinity further northward (fig. 4.4a). Subduction rates of AAIW and SAMW formation increase north of 50°S, so pCO_{2,atm}-equilibrated waters take additional anthropogenic carbon into the deeper ocean. The southward shift of westerly winds weakens the northern edge of Ekman transport at 30-40°S.

The changes in MLD also contribute to the vertical transport of carbon. By deeper mixing in winter, more carbon-rich waters are included into the MLD, which then serves as a larger super-saturated reservoir. MLD deepens south of 50°S and slightly shoals north of 45°S, whereas open-ocean convection causes the unrealistic zonal MLD averages below 30°S (fig. 4.5) [Sallée et al., 2013a; Stössel et al., 2015].

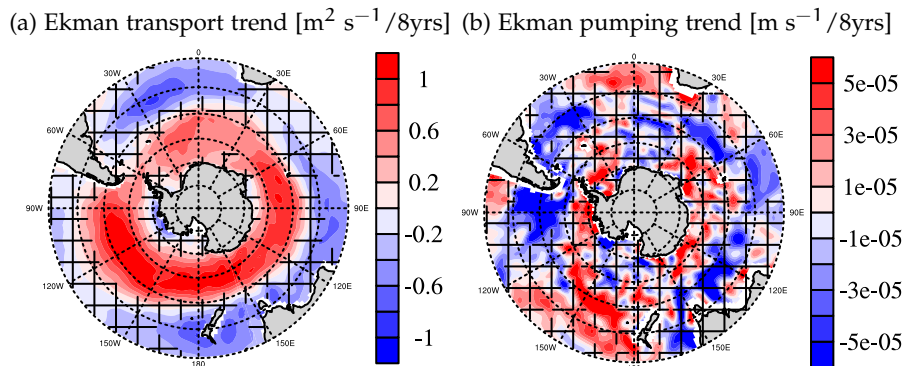


Figure 4.4: Linear trends during the most positive 8-year sea-air CO₂ flux trend: (a) Ekman transport and (b) Ekman pumping; hatched areas indicate where trends are outside the 5% significance level.

The upper-ocean overturning circulation response presented here is in-line with idealized wind-change studies [Lauderdale et al., 2013], modeling studies explaining the observed CO₂ flux trend in the 1990s [Le Quéré et al., 2007; Lovenduski et al., 2007; Lovenduski et al., 2008] as well an inverse modeling study for the 1990s [DeVries et al., 2017].

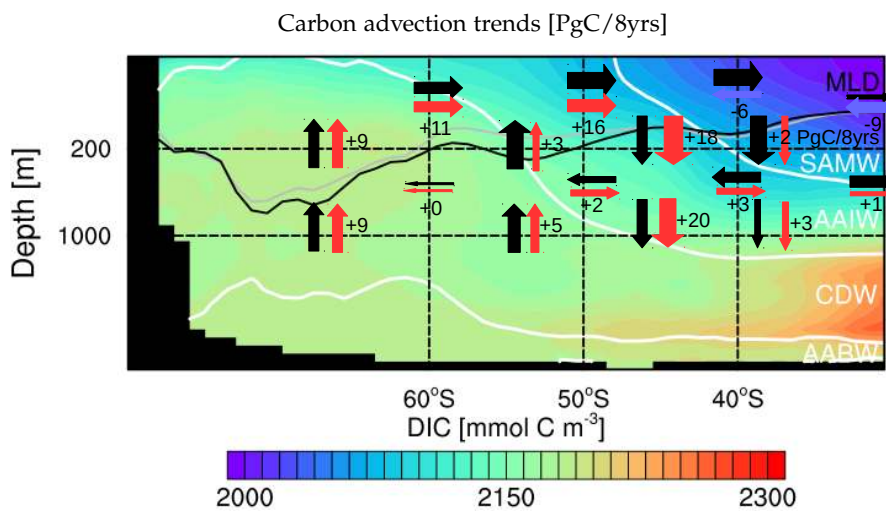


Figure 4.5: Zonally averaged upper-ocean overturning circulation during the most positive 8-year sea-air CO₂ flux trend; black arrows show mean advective carbon transport, red arrows show advective carbon transport trends enforcing the upper-ocean overturning circulation; blue arrows show advective carbon transport trends weakening the upper-ocean overturning circulation; black numbers quantify the trends in advective carbon transport in PgC/8yrs; white lines are isopyncals as in fig. 3.8; grey line is MLD in the beginning and the black line MLD in the end of the period.

4.2.3 Changes in biology during positive CO₂ flux trends

The biological pump draws down surface dissolved inorganic carbon (**DIC**), slightly increases alkalinity and is sensitive to changes in circulation (fig. A12). Mixing changes nutrient distributions, when remineralized nutrients from the deep ocean flush into the euphotic zone. Mixing also pulls the standing stock of phytoplankton deeper into the ocean, where less light inhibits growth. Changes in **SST** also directly affect phytoplankton growth (sec. 2.1.3).

In this subsection, I analyze the 8-year summer (SONDJF) austral summer trends to understand the trends in primary production.

Primary production and sea-air CO₂ flux show opposing zonally symmetric trend patterns as phytoplankton growth takes up large amounts of surface **DIC**, but only weakly increases alkalinity and hence lowers pCO₂ (fig. 4.2a, 4.6a). Primary production declines most pronounced at 50-60°S, increases at 40-50°S and declines at 30-40°S. The challenge at hand is to find out which changes drive these different responses.

Internally varying processes change the availability of nutrients. The decline in nutrients in the subtropics at 30-40°S reduces primary production, but the nutrient availability factor (sec. 2.1.3) slightly increases south of 50°S (fig. 4.6b). Previous observational and modeling studies suggest an increase in primary production, because upwelling brings nutrients, especially iron, from the deep-ocean to the iron-limited surface waters [Lovenduski and Gruber, 2005; Hauck et al., 2013; Wang and Moore, 2012; Tagliabue et al., 2014]. Additional iron fosters primary production following the iron-hypothesis [Martin et al., 1990; Martin, 1990], but observational data for iron is still rather sparse to test this for the whole Southern Ocean [Tagliabue et al., 2014]. Contrasting HAMOCC, many models reproduce this suggested iron-limitation in the Southern Ocean and hence respond with increasing primary production [Wang and Moore, 2012; Hauck et al., 2013].

If the reduction in primary production at 50-60°S cannot be explained by changes in nutrients, what else effects primary production blooms?

The combined light & temperature limitation is primarily driven by temperature after the insulation excels a threshold in cold waters (fig. A11). The strong **SST** cooling trend dominates the light & temperature limitation of primary production. The strong signal in coastal areas as well as Weddell and Ross Sea is attributed to sea-ice changes and open-ocean convection but has minor effects on the primary production and CO₂ flux (fig. 4.6c).

This northward Ekman transport could also advect phytoplankton northwards to cause the increase in primary production at 40-50°S (fig. 4.4b, 4.6a).

The overall decline of primary production in the Southern Ocean under a positive SAM trend is also related to mixing. The summer MLD has a strong increasing trend at 50-60°S, so the mixing deepens (fig. 4.6d). This is caused by stronger winds (fig. 4.2c) and shown in the average depth of the vertical diffusivity due to wind (fig. 4.6e). This deeper mixing in summer then mixes the standing stock of phytoplankton to deeper levels, where they are exposed to less light (fig. 4.6f) [Margalef, 1997]. This theory of a critical depth for phytoplankton blooms was initially proposed by Sverdrup, 1953 and requires a stable water column for phytoplankton to initiate blooms. However, this theory is based on turbulent mixing, so the oceanographic MLD only serves as a first-order mixing measure for phytoplankton [Franks, 2014]. Still the signal sustains to phytoplankton depth, where the average phytoplankton depth decreases up to 15m resulting in up to 30% less light. The lack of monthly output for 3D biogeochemical variables made me use annual averages for phytoplankton, which causes the low significance in fig. 4.6f.

The reverse processes contribute to the increase at 40-50°S. Less winds mix less deep and allow phytoplankton to stay more confined to the surface, where they get more light and flourish (fig. 4.2c, 4.6e, 4.6f). Also the warming increases the phytoplankton growth rate (fig. 4.6c).

Summarizing, a multitude of interconnected processes cause the decline in primary production in the Southern Ocean for an increasing SAM trend. A clear separation of the magnitude of these interdependent processes is impossible.

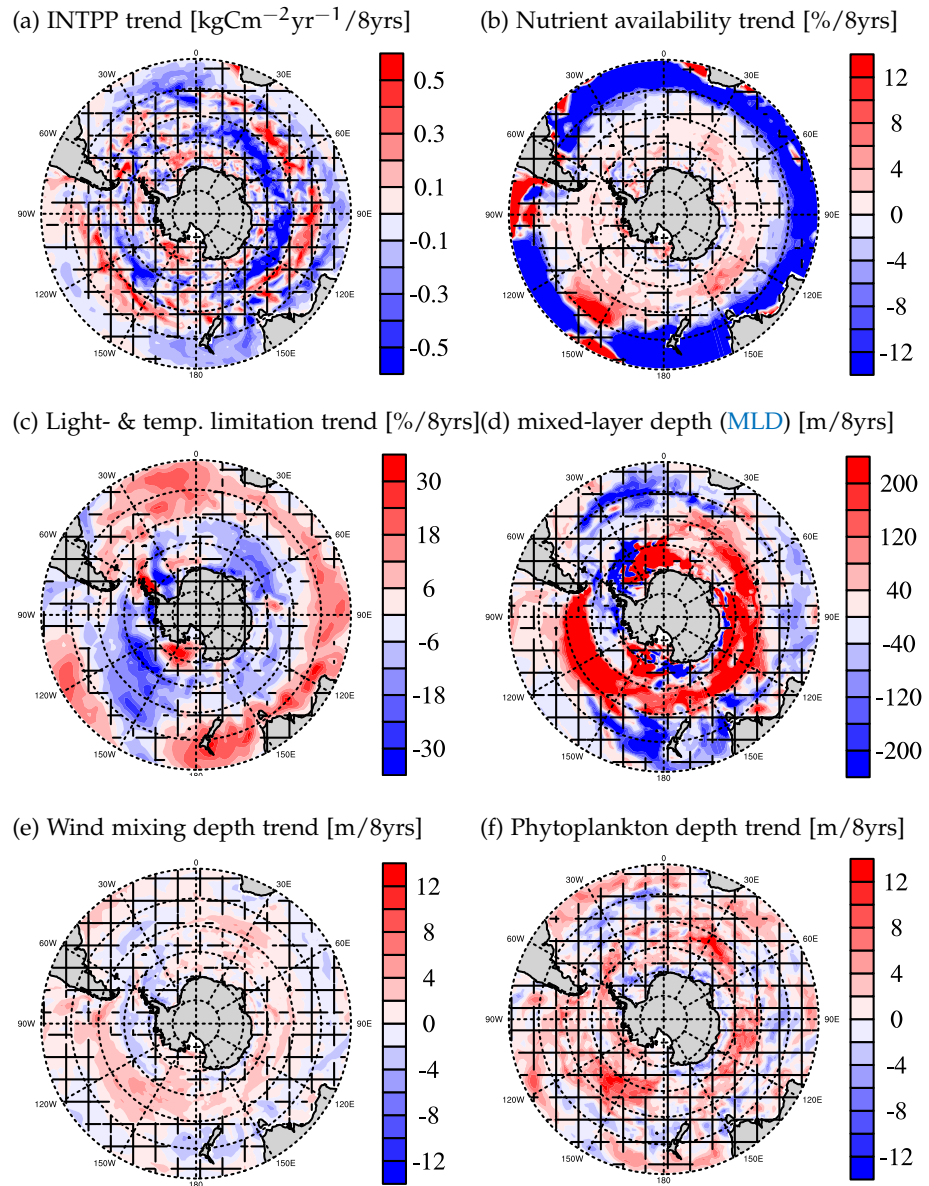


Figure 4.6: Southern Ocean austral summer trends during the most positive 8-year sea-air CO₂ flux trend: (a) integrated primary production (INTPP), (b) nutrient availability factor, (c) surface temperature & limitation function, (d) mixed-layer depth (MLD), (e) average depth of vertical diffusivity due to wind and (f) phytoplankton average depth; hatched areas indicate where trends are outside the 5% significance level.

4.3 NEGATIVE CO₂ FLUX TRENDS

Disclaimer: Generally, in this analysis the direction of trends reverse for weakening and northward-shifting westerlies, which leads to an overall negative sea-air CO₂ flux trend. Additionally, now the prescribed atmospheric pCO_{2,atm} forcing promotes a steady negative background sea-air CO₂ flux trend.

A strong negative sea-air CO₂ flux trends correlates with weaker westerly winds (fig. 4.7a, 4.7c). The strongest negative signal ΔpCO₂ occurs in the upwelling area at 50-60°S. Changes in most other areas of the Southern Ocean are insignificant (fig. 4.7b).

The response in the thermal effect, upper-ocean overturning circulation and biology are described in sec. 4.3.1, 4.3.2 and 4.3.3, respectively.

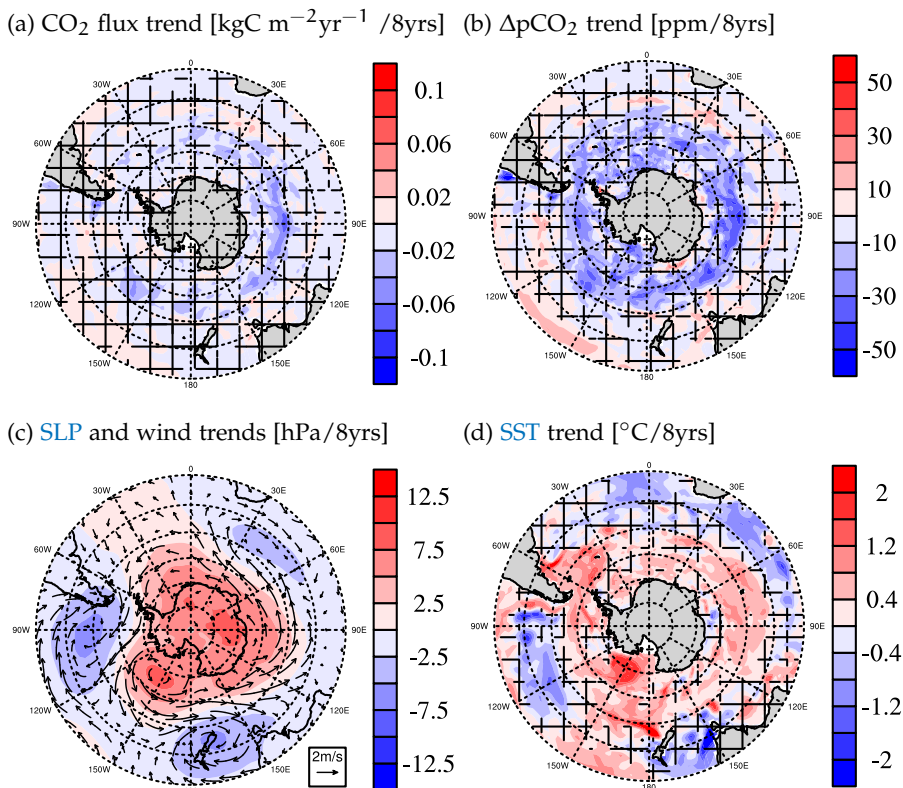


Figure 4.7: Linear trends during the most negative monotonic 8-year air-sea CO₂ flux trend: (a) sea-air CO₂ flux, (b) ΔpCO₂, (c) SLP and wind vectors overlaid as arrows and (d) sea-surface temperature (SST); hatched areas indicate where trends are outside the 5% significance level.

4.3.1 Changes in the thermal effect during negative CO₂ flux trends

The SST warming trend ([fig. 4.7d](#)) drives the thermal trend south of 50°S towards a positive pCO_{2,ocean} trend, whereas the cooling north of 50°S results in a pCO_{2,ocean} decline ([fig. 4.8a](#)). These SST changes are caused by less Ekman transport and lead to a heat convergence in the polar region and a heat divergence in the subtropics [Hall and Visbeck, [2002](#)]. The non-thermal trend has a strong negative signal south of 50°S and a slightly positive north of 50°S ([fig. 4.8b](#)). The increase in atmospheric pCO_{2,atm} accounts for a -14 ppm/8 yrs. The non-thermal and thermal trends combined nearly compensates north of 50°S, but the non-thermal component dominates at 50-60°S ([fig. 4.7b](#)).

These changes are stronger in the summer season, especially the non-thermal component, because of the stronger SLP winter trends ([fig. A9, A10](#)).

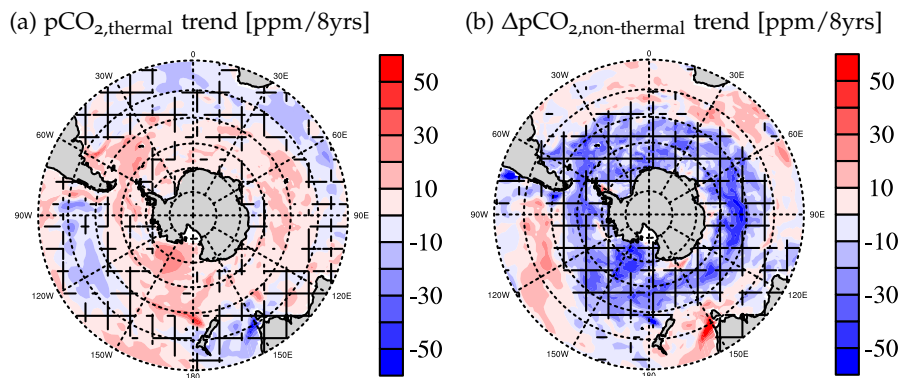


Figure 4.8: Linear trends during the most negative monotonic 8-year sea-air CO₂ flux trend: (a) pCO_{2,thermal} and (b) ΔpCO_{2,non-thermal}; hatched areas indicate where trends are outside the 5% significance level.

4.3.2 Changes in ocean circulation during negative CO₂ flux trends

Weaker westerly winds weaken the upper-ocean overturning circulation [Lauderdale et al., 2013], so the circulation field advects less DIC and alkalinity along its overturning pathway (fig. 4.10). Less upwelling at 50-60°S decreases DIC and alkalinity concentrations in the euphotic zone (fig. 4.9b). Weaker winds also decrease Ekman northward transport and reduce northward advection of DIC and alkalinity (fig. 4.9a). North of 50°S subduction rates of AAIW and SAMW formation decrease, which could also be a sign of a northward-shift in upwelling. The MLD shoals south of 50°S and slightly deepens north of 45°S (fig. 4.10).

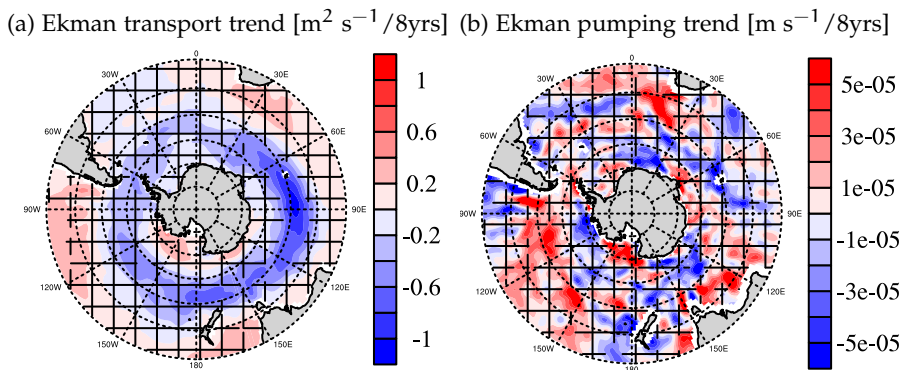


Figure 4.9: Linear trends during the most negative 8-years sea-air CO₂ flux trend: (a) Ekman transport and (b) Ekman pumping; hatched areas indicate where trends are outside the 5% significance level.

This upper-ocean overturning circulation response agrees with idealized wind-change studies [Lauderdale et al., 2013]. The inverse modeling study reports a decline from the 2000s towards the previous decade [DeVries et al., 2017], which could be related to changes in wind. However, Landschützer et al., 2015 did not report a strong negative trend for the strength of observed westerly winds, but a pattern change in SLP in the 2000s became more zonally asymmetric. On the contrary, depending on the starting year of the trend period, the SAM index slightly weakened in the early 2000s [Marshall, 2003; Lovenduski et al., 2015].

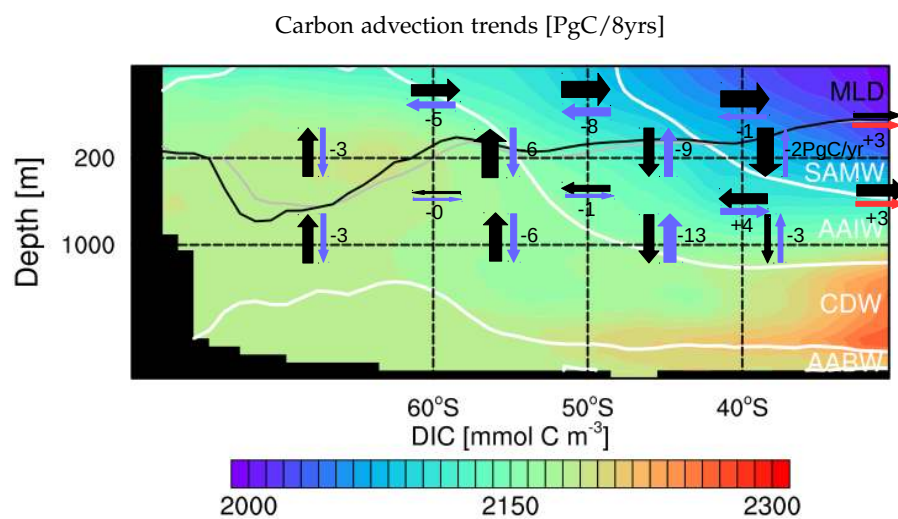


Figure 4.10: Zonally averaged upper-ocean overturning circulation during the most negative 8-year sea-air CO₂ flux trend; black arrows show mean advective carbon transport, red arrows show advective carbon transport trends enforcing the upper-ocean overturning circulation; blue arrows show advective carbon transport trends weakening the upper-ocean overturning circulation; black numbers show the trends in advective carbon transport in PgC/8yrs; white lines are isopycnals as in fig. 3.8; grey line is MLD in the beginning and the black line MLD in the end of the period.

4.3.3 Changes in biology during negative CO₂ flux trends

Primary production and CO₂ flux show opposing zonally symmetric trend patterns ([fig. 4.7a](#), [4.11a](#)). The patchy trend patterns of primary production increase most dominant at 50-60°S, decrease at 40-50°S and increase at 30-40°S.

The additional supply of nutrients in the subtropics at 30-40°S fosters primary production, because the northward-shift in upwelling flushes nutrients from the deep into the nutrient-depleted subtropical gyre region. South of 45°S the nutrient availability hardly changes and decreases ([fig. 4.11b](#)). Previous observational and modeling studies suggest decreasing in primary production because less upwelling brings less nutrients, especially iron, from the deep-ocean to the surface [Hauck et al., [2013](#); Tagliabue et al., [2014](#)]. But the Southern Ocean in [HAMOCC](#) is nitrate limited, so the slight reduction in nutrients rather originates in the increased nutrient consumption due to primary production.

The [SST](#) trends enhance primary production at 50-60°S and lower primary production north of 50°S ([fig. 4.11c](#)).

The weakened northward Ekman transport also keeps the standing stock more southwards and causes the increase in primary production at 50-60°S and the shifted decrease at 40-50°S ([fig. 4.9](#)).

Weaker winds mix the ocean less deep and thereby keeps the standing stock of phytoplankton in more light-flooded levels at 50-60°S ([fig. 4.11e](#)). The reverse process contributes to the decrease at 40-50°S.

Overall, primary production decreases for weaker and northward-shifting winds.

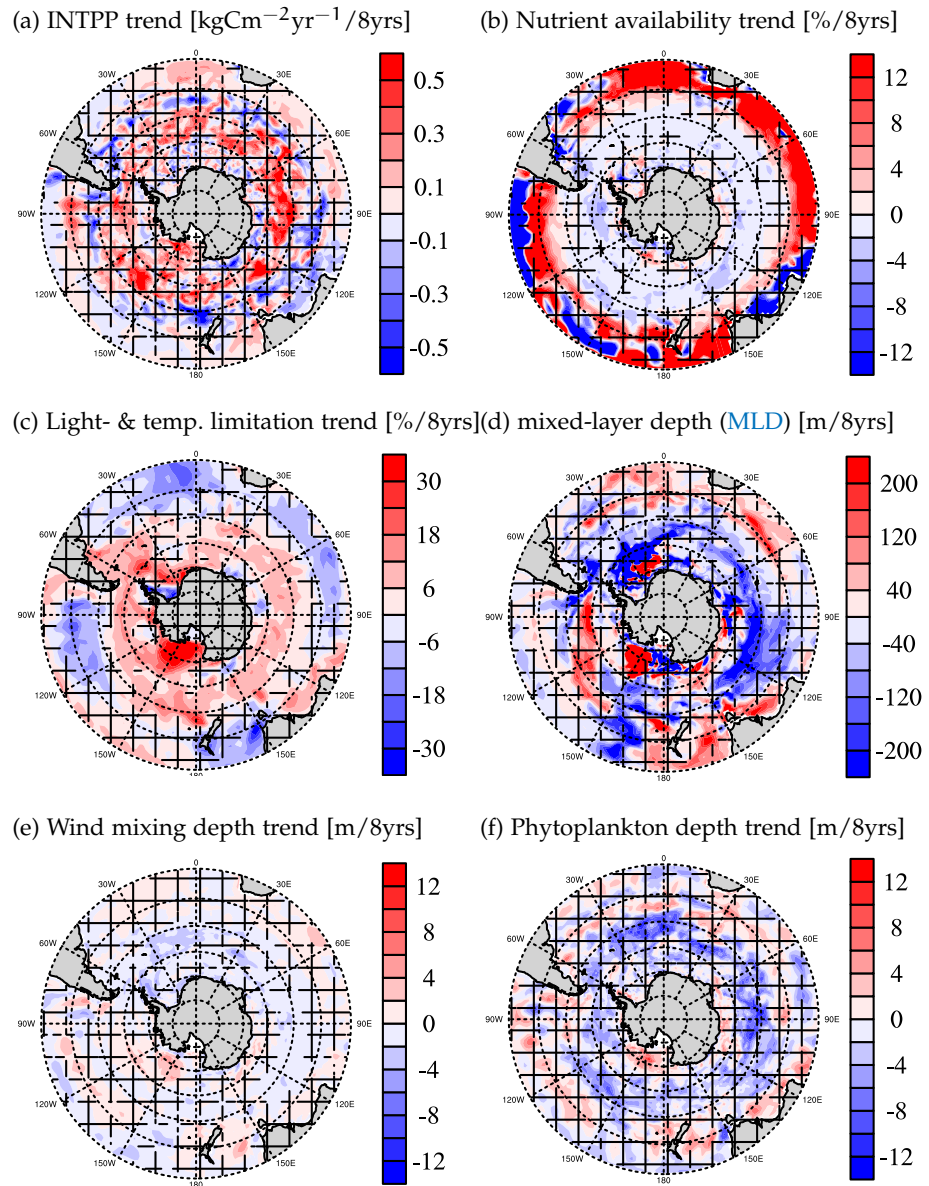


Figure 4.11: Southern Ocean austral summer trends during the most negative sea-air 8-year CO₂ flux trend: (a) vertically integrated primary production (INTPP), (b) nutrient availability factor, (c) surface temperature & limitation function, (d) mixed-layer depth (MLD), (e) average depth of vertical diffusivity due to wind and (f) phytoplankton average depth; hatched areas indicate where trends are outside the 5% significance level.

CONTRIBUTION OF DIFFERENT PROCESSES TO MULTI-YEAR PCO₂ TRENDS

The previous analysis of thermal, circulation and biological CO₂ flux responses towards the westerly winds in ch. 4 asks for an estimate on the relative contributions of each process to the total change. As all the processes interact with each other non-linearly, a clear and clean separation cannot be taken in precision. Therefore the results of this chapter must be understood rather as an *estimation of the first-order drivers* in pCO₂. In this chapter I adapt the pCO₂ diagnostics framework from Lovenduski et al. [2007] to quantitatively estimate the different contributions to pCO_{2,ocean} and thus sea-air CO₂ flux changes.

5.1 DERIVATION OF THE FRAMEWORK

The framework relies on a well-mixed alkalinity and carbon budget across zonal bands of 10° latitude from 50-60°S and 40-50°S of the upper ocean upto the mixed-layer depth (MLD) (fig. 5.1). pCO_{2,ocean} changes associated with different processes are calculated from monthly model output data.

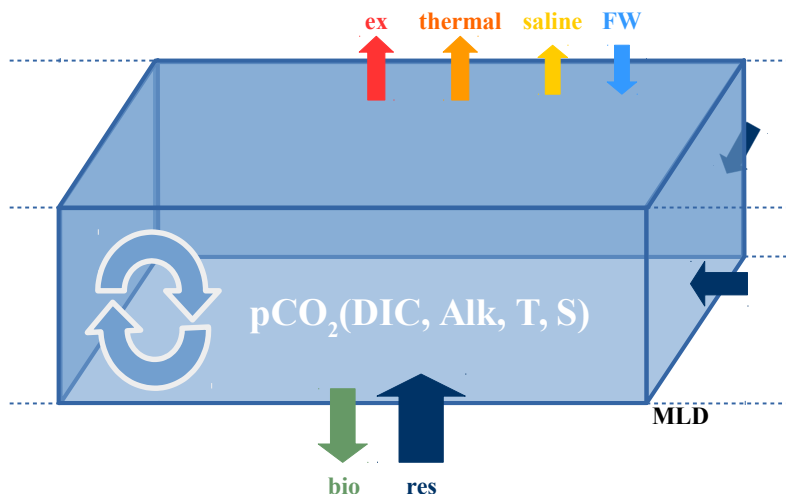


Figure 5.1: Schematic illustration of pCO₂ driver separation assuming a well-mixed zonal box, where changes in pCO_{2,ocean} are separated into contributions due to sea-air CO₂ flux (red), thermal effect (orange), the saline effect (yellow), freshwater (light blue), biology (green) and a residual (dark blue)

I separate pCO_{2,ocean} into different perspectives of understanding: The first perspective on the changes in dissociation constants and solubility separates contributions in the thermal and the saline effect. The second perspective associates pCO_{2,ocean}-changes with concentration changes in alkalinity (Alk) and **DIC**.

$$\delta pCO_{2,ocean} = \underbrace{\delta pCO_{2,thermal} + \delta pCO_{2,sal}}_{\text{dissociation constants and solubility changes}} + \underbrace{\delta pCO_{2,non-thermal-sal}}_{\text{concentration changes}} \quad (5)$$

$$\delta pCO_{2,non-thermal-sal} \approx \delta pCO_{2,Alk} + \delta pCO_{2,DIC} \quad (6)$$

The thermal separation from Takahashi et al. [1993; 2002] identifies a thermal pCO_{2,thermal} from pCO_{2,ocean} (eq. 7). This empirical fit describes the changes in pCO_{2,ocean} of a warming water parcel, i. e. how the temperature-dependent equilibrium constants and solubility change the pCO_{2,ocean} at constant salinity, **DIC** and alkalinity.

The salinity dependence for constant **DIC**, alkalinity and **SST** describes the changes of dissociation constants due to changes in salinity (eq. 8), so an increase in salinity increases pCO_{2,ocean} [Sarmiento and Gruber, 2006]. The non-thermal-saline residual (eq. 9) covers the changes of all other processes, which vary pCO_{2,ocean} excluding the thermal and saline effect, namely concentration changes in **DIC** and alkalinity:

$$\delta pCO_{2,thermal} \approx \frac{\partial pCO_2}{\partial T} \cdot \delta T \approx \overline{pCO_2} \cdot 0.0423^{\circ}\text{C}^{-1} \cdot \delta T \quad (7)$$

$$\delta pCO_{2,sal} = \frac{\partial pCO_2}{\partial S} \cdot \delta S \approx \frac{\overline{pCO_2}}{\bar{S}} \cdot \underbrace{\gamma_S}_{\approx 1} \cdot \delta S \quad (8)$$

$$\delta pCO_{2,non-thermal-sal} = \delta pCO_{2,ocean} - \delta pCO_{2,therm} - \delta pCO_{2,sal} \quad (9)$$

For a deeper look into the pCO_{2,ocean} due to non-thermal-saline effects (eq. 9), I use the salinity-normalized concentrations sDIC and sAlk for **DIC** and alkalinity to prevent double-accounting of freshwater (FW) changes in **DIC** and alkalinity [Keeling et al., 2004]:

$$sDIC = \frac{DIC}{S} \cdot S_0 \quad S_0 = 35 \text{ psu} \quad (10)$$

$$\begin{aligned} \delta pCO_{2,non-thermal-sal} &\approx \frac{\partial pCO_2}{\partial (S/S_0 \ sAlk)} \delta(S/S_0 \ sAlk) \\ &\quad + \frac{\partial pCO_2}{\partial (S/S_0 \ sDIC)} \delta(S/S_0 \ sDIC) \end{aligned} \quad (11)$$

$$\begin{aligned} &\approx \frac{S}{S_0} \frac{\partial pCO_2}{\partial Alk} \delta sAlk + \frac{S}{S_0} \frac{\partial pCO_2}{\partial DIC} \delta sDIC \\ &\quad + \frac{\partial pCO_2}{\partial FW} \delta FW \end{aligned} \quad (12)$$

$p\text{CO}_{2,\text{ocean}}$ increases for increasing **DIC** and decreases for increasing alkalinity:

$$\frac{\partial p\text{CO}_2}{\partial \text{DIC}} = \frac{p\text{CO}_2}{\text{DIC}} \cdot \gamma_{\text{DIC}} \quad (13)$$

$$\frac{\partial p\text{CO}_2}{\partial \text{Alk}} = \frac{p\text{CO}_2}{\text{Alk}} \cdot \gamma_{\text{Alk}} \quad (14)$$

It is noteworthy that sensitivity factors γ_{DIC} and γ_{Alk} are approximations, because they are partial derivatives from a simplified $p\text{CO}_{2,\text{ocean}}$ formulation by substituting bicarbonate and carbonate ion concentrations with **DIC** and alkalinity [Sarmiento and Gruber, 2006, p. 328]:

$$\gamma_{\text{DIC}} \approx \frac{3 \cdot \text{Alk} \cdot \text{DIC} - 2 \cdot \text{DIC}^2}{(2 \cdot \text{DIC} - \text{Alk})(\text{Alk} - \text{DIC})} \quad (15)$$

$$\gamma_{\text{Alk}} \approx -\frac{\text{Alk}^2}{(2 \cdot \text{DIC} - \text{Alk})(\text{Alk} - \text{DIC})} \quad (16)$$

Additional freshwater input (eq. 12) reduces the concentration of **DIC**, alkalinity and salinity by dilution and leads to a slight decrease in $p\text{CO}_{2,\text{ocean}}$. Vice versa, net evaporation increases the concentration of **DIC**, alkalinity and salinity and thus increases $p\text{CO}_{2,\text{ocean}}$:

$$\frac{\partial p\text{CO}_2}{\partial \text{FW}} = \frac{s\text{DIC}}{S_0} \frac{\partial p\text{CO}_2}{\partial \text{DIC}} \delta S + \frac{s\text{Alk}}{S_0} \frac{\partial p\text{CO}_2}{\partial \text{Alk}} \delta \text{Alk} \quad (17)$$

Furthermore the changes in $s\text{DIC}$ and $s\text{Alk}$ are separated into biological, sea-air exchange and residual contribution to check for the origin of **DIC** and alkalinity changes, i. e. biological export, sea-air CO_2 flux or other not specified processes as the residual (likewise for $\delta s\text{Alk}$):

$$\frac{\delta(s\text{DIC})}{\delta t} = \frac{\delta(\text{DIC}_{\text{bio}})}{\delta t} + \frac{\delta(\text{DIC}_{\text{exchange}})}{\delta t} + \frac{\delta(s\text{DIC}_{\text{res}})}{\delta t} \quad (18)$$

The changes due to sea-air CO_2 flux and biology are converted to **DIC** and alkalinity concentration changes by dividing by the **MLD** assuming that the concentration changes are well-mixed across the mixed layer. This assumes that the system is in a steady state and only changes in CO_2 flux, biological export and the residual affect the $p\text{CO}_{2,\text{ocean}}$ trend.

Furthermore, the concentration change of biological primary production and remineralization contributes with organic matter export (coex) and calcium carbonate export (caex) to changes in **DIC** and alkalinity. Organic matter production reduces **DIC** and increases alkalinity. Calcification increases **DIC** and reduces alkalinity by two units by consuming the carbonate ion (Ca^{++}). The magnitude of conversion factors arise from the fixed Redfield stoichiometry ($\text{C} : \text{N} : \text{P} = 122 : 16 : 1$) converting carbon to phosphate units in which alkalinity

is accounted for. For a representation of the pCO_{2,ocean} responses of the different processes see [fig. A12](#).

$$\delta\text{DIC}_{\text{bio}} = -\frac{\text{coex} + \text{caex}}{\text{MLD}} \quad (19)$$

$$\delta\text{Alk}_{\text{bio}} = -\frac{2 \cdot \text{caex} - 16/122 \cdot \text{coex}}{\text{MLD}} \quad (20)$$

The resulting sea-air CO₂ flux reflects the pCO_{2,ocean} after being exposed to all changes by biology and circulation. By definition, CO₂ is also temperature-dependent in k_w and reduces the **DIC** concentration without changing alkalinity ([sec. 2.1.3](#)):

$$\delta\text{DIC}_{\text{ex}} = -\frac{\text{CO}_2 \text{flux}}{\text{MLD}} \quad (21)$$

$$\delta\text{Alk}_{\text{ex}} = 0 \quad (22)$$

These concentration changes in **DIC** and alkalinity modify pCO_{2,ocean} at the same time. The **DIC** and alkalinity contribute with different γ sensitivities and add up to the combined pCO_{2,ocean} change, e.g. the total pCO_{2,bio} change combines pCO_{2,bio,DIC} and pCO_{2,bio,Alk}.

The remaining salinity-corrected residual pCO_{2,res} accounts for all other processes not covered in this framework and approximative errors:

- vertical and lateral advection of **DIC** and alkalinity
- changes in biological carbon inventory
- lateral advection of organic tracers
- linearizations of non-linear processes
- calculation from monthly timesteps
- simplification of γ sensitivity constants in Sarmiento and Gruber, 2006 ([eq. 15, 16](#))
- non-steady state in the beginning of the period

5.2 ESTIMATE OF PCO₂ DRIVERS

Applying the above described framework yields an estimation for the drivers of pCO₂ for the two extreme trends into the two latitudinal regions each with opposing responses from ch. 4 (tab. 5.1). In this section I analyze the positive and negative pCO_{2,ocean} trends first under the perspective of dissociation constants and solubility changes, and then to gain further insights on the non-thermal-saline part under the perspective of concentration changes. Concluding, I frame a picture of the ΔpCO₂ changes and thus sea-air CO₂ flux.

pCO _{2,x} [ppm]	8-yr trend		50-60°S		40-50°S	
	positive	negative	positive	negative	positive	negative
pCO _{2,thermal}	-7.1	6.7	3.4	0.7		
pCO _{2,sal}	0.6	-0.5	0.2	-0.3		
pCO _{2,non-thermal-sal}	38.4	-8.7	6.4	12.5		
pCO _{2,FW}	0.6	-0.5	0.2	-0.3		
pCO _{2,sDIC}	37.6	1.0	10.6	19.1		
pCO _{2,sAlk}	8.1	-4.2	-1.8	-1.5		
pCO _{2,ex,DIC}	-5.1	5.2	0.2	1.1		
pCO _{2,bio,DIC}	4.9	-6.2	-1.4	-0.1		
pCO _{2,bio,Alk}	0.5	-0.6	-0.1	-0.0		
pCO _{2,bio}	5.4	-6.8	-1.5	-0.1		
pCO _{2,res,sDIC}	40.0	-0.8	9.8	18.2		
pCO _{2,res,sAlk}	7.8	-3.9	-1.7	-1.5		
pCO _{2,res}	47.8	-4.7	8.1	16.7		
pCO _{2,ocean}	32.1	-2.4	9.4	12.9		
pCO _{2,atm}	12.0	14.5	12.0	14.5		
dpCO ₂	20.2	-16.9	-2.6	-1.6		

Table 5.1: Trends in drivers of pCO₂ for the most positive sea-air CO₂ flux trend and the most negative sea-air CO₂ flux trend in two 10°-MLD boxes. Only austral summer months contribute to biological trends (pCO_{2,bio}).

During the most positive sea-air CO₂ flux trend at 50-60°S, the thermal trend (pCO_{2,thermal}) decreased because of sea-surface cooling and drives carbon uptake (sec. 4.2.1). While salinity changes (pCO_{2,sal}) are negligible, the overall trend (pCO_{2,ocean}) opposes the thermal trend (pCO_{2,thermal}). So changes in dissociation constants in the thermal and saline effect do not drive this pCO_{2,ocean} trend but changes in concentration (pCO_{2,non-thermal-sal}).

The perspective on processes changing **DIC** and alkalinity reveals that concentration (the opposite process to dilution, see [fig. A12](#)) of **DIC** and alkalinity ($p\text{CO}_{2,\text{FW}}$) has only a minor effect. The largest contribution to the $p\text{CO}_{2,\text{ocean}}$ trend arises from the changes in salinity-normalized alkalinity ($p\text{CO}_{2,\text{sAlk}}$) and mostly **DIC** ($p\text{CO}_{2,\text{sDIC}}$). As outgassing increases, **DIC** ($p\text{CO}_{2,\text{ex,DIC}}$) increasingly leaves the system and thereby decreases $p\text{CO}_{2,\text{ocean}}$. For biological processes I take only the summer trends as phytoplankton does not bloom in winter. It comprises mostly organic matter production which decreases and therefore exports less carbon and more alkalinity out of the system all-in-all increasing $p\text{CO}_{2,\text{ocean}}$ ([sec. 4.2.3](#)). The remaining residual in **DIC**-driven ($p\text{CO}_{2,\text{res,sDIC}}$) and alkalinity-driven ($p\text{CO}_{2,\text{res,sAlk}}$) trends, which are not covered by a distinct process in this framework, dominate this concentration-driven ($p\text{CO}_{2,\text{non-thermal-sal}}$) trend. Therefore at this instance, biology ($p\text{CO}_{2,\text{bio}}$) plays only a minor role and is likely outplayed by circulation changes ($p\text{CO}_{2,\text{res}}$). The changes due to upwelling are very dependent on the history of the water masses advected into and out of the system. Generally, deeper waters have higher **DIC** and alkalinity concentrations in the Southern Ocean and **DIC** would have a slightly higher impact on $p\text{CO}_{2,\text{ocean}}$ because of slightly higher γ_{DIC} , but the proportions of **DIC** and alkalinity matter. So here a strong increase in **DIC** increases $p\text{CO}_{2,\text{res,sDIC}}$ while the increase in alkalinity reduces $p\text{CO}_{2,\text{res,sAlk}}$. These changes are either due to advection changes or an underestimation of the organic matter production decrease ($p\text{CO}_{2,\text{bio}}$). The trends in advection of both **DIC** ($p\text{CO}_{2,\text{res,sDIC}}$) and alkalinity ($p\text{CO}_{2,\text{res,sAlk}}$) are negative, so while upwelling could explain the the **DIC** ($p\text{CO}_{2,\text{res,sDIC}}$) trend, a clear attribution of upwelling to alkalinity ($p\text{CO}_{2,\text{res,sAlk}}$) cannot be made here ([sec. 4.2.2](#)).

At 40-50°S, the warming trend increases $p\text{CO}_{2,\text{thermal}}$, which drives CO₂ outgassing ([sec. 4.2.1](#)). Also the contributions unrelated to dissociation constants changes ($p\text{CO}_{2,\text{non-thermal-sal}}$) increase but at a higher rate.

Looking deeper into these contributions biology slightly increases, so $p\text{CO}_{2,\text{bio}}$ decreases ([sec. 4.2.3](#)), while changes in air-sea CO₂ flux ($p\text{CO}_{2,\text{ex,DIC}}$) are negligible. Overall the residual ($p\text{CO}_{2,\text{res,sAlk}}$) dominates again. Here, unaccounted processes increase **DIC** and alkalinity, so $p\text{CO}_{2,\text{res,sDIC}}$ increases and $p\text{CO}_{2,\text{res,sAlk}}$ decreases. $p\text{CO}_{2,\text{res,sDIC}}$ drives the $p\text{CO}_{2,\text{ocean}}$ trend. As advection increases **DIC** and alkalinity this is related to the circulation changes ([sec. 4.2.2](#)).

Combining the $p\text{CO}_{2,\text{ocean}}$ responses for the most extreme positive CO₂ flux trend with the atmospheric $p\text{CO}_{2,\text{atm}}$ changes lead me to a comprehensive CO₂ flux picture ([fig. 5.2](#)).

While the cooling effect of the stronger winds reduces outgassing in the high-latitude Southern Ocean, the decline in primary production and mostly the increasing upwelling of deeper waters and outplay the thermal effect to a strong positive pCO_{2,ocean} trend at 50-60°S. At 40-50°S the warming effect reduces carbon uptake, which outweighs the non-thermal-saline changes, namely increasing DIC due to lateral advection and less downwelling (with negligible contributions from sea-air CO₂ flux and biology), which leads to a combined positive pCO_{2,ocean} trend.

The atmospheric trend pCO_{2,atm} is strictly positive and sets ΔpCO₂ to a still strong positive trend at 50-60°S and a weak decreasing trend at 40-50°S. The resulting outgassing CO₂ flux trend at 50-60°S is stronger than the weak CO₂ uptake trend at 40-50°S and hence determines the overall Southern Ocean carbon sink trend. The overall positive CO₂ flux trend and its opposite thermal contributions agree with Lovenduski et al., 2007.

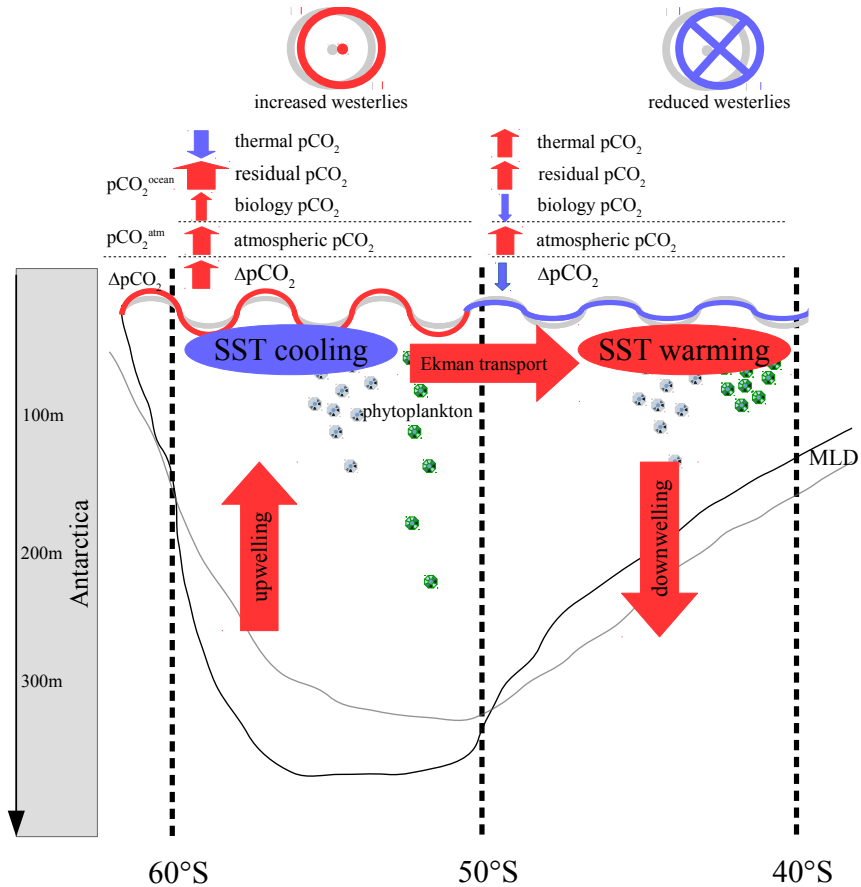


Figure 5.2: Schematic illustration of the Southern Ocean under the context of increasing westerly winds and response in the thermal effect, biology and upper-ocean circulation lead towards a positive sea-air CO₂ flux trend; red color-coding indicates a relative increase of the related quantity or process, whereas blue indicates a relative decrease. The grey line represents the mixed-layer depth (MLD) in the beginning of the trend period, the black line the MLD in the end of the trend period.

During the most negative sea-air CO₂ flux trend at 50-60°S, the thermal trend ($pCO_{2,thermal}$) decreased due to sea-surface warming (sec. 4.3.1), the saline effect ($pCO_{2,sal}$) is negligible, but the thermal and saline effects are overcompensated by concentration changing processes ($pCO_{2,non-thermal-sal}$). But this is of far less extent than for the most positive sea-air CO₂ flux trend, as the overall $pCO_{2,ocean}$ only slightly decreases. The contribution of **DIC** ($pCO_{2,sDIC}$) increases only slightly, whereas the contribution from alkalinity ($pCO_{2,sAlk}$) dominates the negative trend. Looking into the individual processes, increased CO₂ uptake ($pCO_{2,ex,DIC}$) increases, whereas increased biology ($pCO_{2,bio}$) reduces $pCO_{2,ocean}$. The residual **DIC** contribution ($pCO_{2,res,DIC}$) slightly decreases as does **DIC** advection (sec. 4.2.2) which could attribute the residual **DIC** to decreased upwelling. The residual alkalinity contribution ($pCO_{2,res,sAlk}$) decreases stronger, but the concentration changes in alkalinity due to advection also decline, so a clean attribution of residual alkalinity changes to advective circulation changes cannot be made here.

At 40-50°S the thermal trend ($pCO_{2,thermal}$) remains almost unaltered and slightly increases (sec. 4.3.1). The major trend in $pCO_{2,ocean}$ outgassing arises from concentration changes ($pCO_{2,non-thermal-saline}$).

Changes in **DIC** ($pCO_{2,sDIC}$) strongly lead this outgassing trend by a strong residual **DIC** ($pCO_{2,res,DIC}$) increase, which comes from increased **DIC** concentrations due to advection, namely less northward advection and reduced downwelling. This reduced downwelling may be a sign of increased upwelling caused by the northward shift of the overturning cell over the 40°S boundary. The same applies for increased alkalinity, where ($pCO_{2,res,sAlk}$) reduces $pCO_{2,ocean}$ slightly. These residual changes ($pCO_{2,res}$) are clear signs of upwelling.

The three distinct pCO₂ responses for the most negative CO₂ flux trend merge with the rising atmospheric $pCO_{2,atm}$ into the opposing picture in CO₂ flux as for decreasing westerly winds (fig. 5.3).

Weaker winds warm the high-latitude Southern Ocean, which leads to outgassing, but the decreasing upwelling and the decline in primary production outplay the thermal effect to a relative ingassing trend at 50-60°S. At 40-50°S temperatures remain constant and decreased Ekman transport **DIC** supply and increased northward-shifted upwelling leads to a combined relative $pCO_{2,ocean}$ outgassing trend.

The strictly positive atmospheric trend $pCO_{2,atm}$ outperforms the slightly negative $pCO_{2,ocean}$ trend at 50-60°S and slightly overcompensates the $pCO_{2,ocean}$ positive trend at 40-50°S. The resulting negative sea-air CO₂ flux signal at 50-60°S is stronger than the slightly positive sea-air CO₂ flux at 40-50°S and hence determines the overall Southern Ocean carbon sink trend.

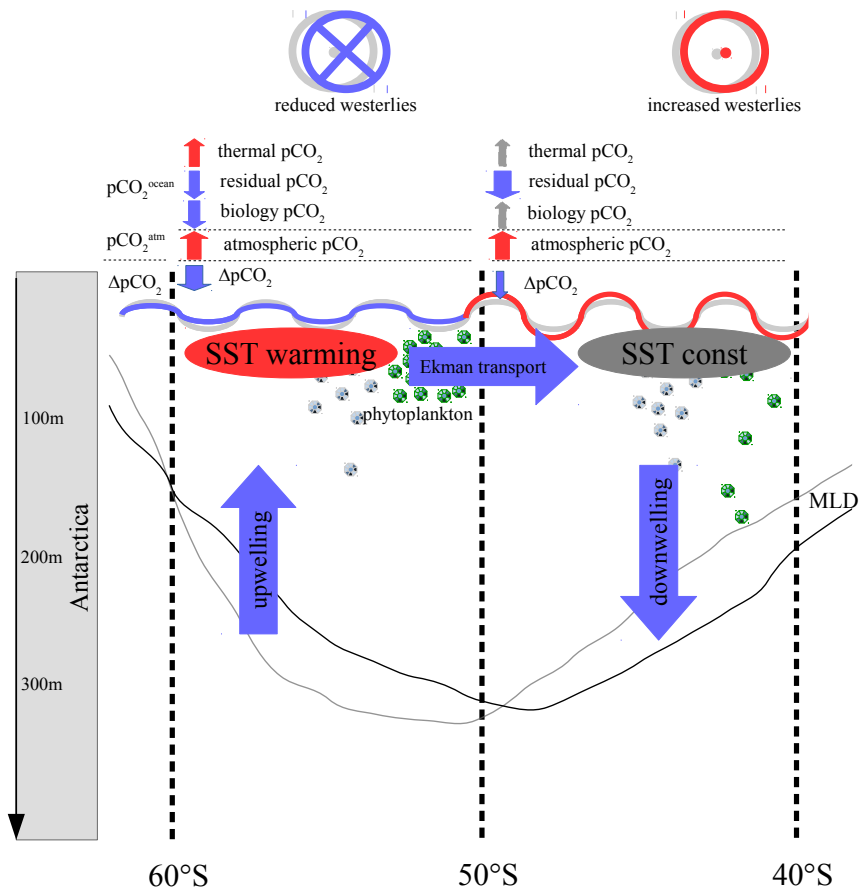


Figure 5.3: Schematic illustration of the Southern Ocean under the context of decreasing westerly winds and response in the thermal effect, biology and upper-ocean circulation leading towards a negative sea-air CO₂ flux trend; red color-coding indicates a relative increase of the related quantity or process, grey indicates no changes and blue indicates a relative decrease. The grey line represents the mixed-layer depth (MLD) in the beginning of the trend period, the black line the MLD in the end of the trend period.

Summarizing, the framework shows the asymmetric contributions of the different drivers in the positive and negative trend ([tab. 5.1](#)). The contribution due to changes in salinity-normalized DIC changes ($pCO_{2,sDIC}$) has a very strong influence and is not symmetric towards zero. $pCO_{2,sDIC}$ mostly reflects the changes in lateral and vertical transport of DIC. Acknowledging that the system is not in steady-state but under transient historical forcing of increasing atmospheric $pCO_{2,atm}$, $pCO_{2,sDIC}$ is expected to rise because the water masses flowing laterally into the budget box are affected by CO₂ uptake by the oceans. In the non-varying carbon uptake state, the expected $pCO_{2,sDIC}$ due to lateral transports could be estimated to the increasing $pCO_{2,atm}$ of $\sim 12 - 14$ ppm/8yrs. Considering this, also $pCO_{2,sDIC}$ responds symmetric.

The framework is very susceptible in the magnitude of individual contributions for the definition of the depth of mixing in [eq. 19-21](#), i. e. whether I choose the top layer of ~ 12 m, fixed 90m, or the actually taken varying mixed-layer depth ([MLD](#)). The direction of the described processes and their relative contributions do not change and the residual adjusts accordingly.

The changes in inventory related to biology is estimated from the change of concentrations from phytoplankton, zooplankton, acfDOC and detritus in carbon units, which make upto $\sim 10\%$ additionally to the biological $pCO_{2,ocean}$ change, but cannot be quantified consistently as the fraction of calcifiers is unknown.

The attribution of the residual changes in DIC to advective changes works at 40-50°S but lacks the clear link at 50-60°S. The trends in alkalinity transport are close to the trends in DIC transport (as in [fig. 4.5](#) and [fig. 4.10](#)). Therefore, the $pCO_{2,ocean}$ trends in the same direction cannot be explained entirely by advective circulation changes. Also the steady state assumption, which is necessary for this box model approach, might shift the framework to misleading responses, because those strong trends cannot start from equilibrium in a transient simulation ([fig. 3.2](#)). Nevertheless, the framework demonstrates that the strongest contribution of the $pCO_{2,ocean}$ trends arises from a process not explicitly specified in the framework, which is most probably the sum of changes in vertical and lateral advection.

6

SUMMARY, CONCLUSIONS AND OUTLOOK

To assess decadal internal variability of the Southern Ocean sea-air CO₂ flux, I analyzed the large ensemble of 100 Max Planck Institute-Earth System Model simulations ([MPI-ESM LE](#)) in the historical period from 1980 to 2004, for which the observational sea-air CO₂ flux product Self-Organizing Map-Feed-Forward Network ([SOM-FFN](#)) is available. I summarize this thesis by revisiting the research questions posed in the introduction.

What is the modeled internal variability of the Southern Ocean carbon sink?

I estimate the modeled decadal internal variability to $\sigma_{\text{DIV}} \sim \pm 0.19$ PgC/yr/decade ([fig. 3.2, A1a](#)). Compared to the 1980-2004 mean sea-air CO₂ flux south of 35°S of ~ -1.15 PgC/yr indicating CO₂ uptake by the ocean, decadal internal variability σ_{DIV} amounts to $\sim 12\%$ of the Southern Ocean carbon sink. In addition, internal variability dominates over the forced sea-air CO₂ flux trend of ~ -0.14 PgC/yr/decade and is hence crucial in evaluating changes in the Southern Ocean carbon sink. The area at 50-60°S has the largest decadal variability ([fig. 3.1b](#)) and dominates the overall Southern Ocean CO₂ flux trend ([ch. 4](#)). [MPI-ESM LE](#) contains positive and negative decadal trends of sea-air CO₂ flux $\sim +0.5$ PgC/yr/decade and ~ -0.7 PgC/yr/ decade of the same magnitude but with less monotonic behavior as suggested by observations [Landschützer et al., [2015](#)] ([fig. A2](#)). The same monotonic behavior as in observations is found in 8-year trends of $\sim +0.5$ PgC/yr/8yrs and ~ -0.6 PgC/yr/8yrs ([fig. 3.2](#)). The underlying source and responses in the carbon sink are analogous on decadal and multi-year time-scale.

What are the sources of this internal variability?

The major source is the variability in strength and position of westerly winds. I find two distinct wind-driven regimes in the area of at 50-60°S with the largest internal variability of sea-air CO₂ flux ([fig. 4.1](#)): On the one hand stronger and southward-shifting westerly winds associated with a positive trend in the Southern Annular Mode ([SAM](#)) reduce the Southern Ocean carbon sink. On the other hand weakening and northward-shifting westerly winds lead to an increase in the Southern Ocean carbon sink.

What are the contributions of different processes to multi-year trends in sea-air CO₂ flux in the Southern Ocean?

The increasing atmospheric pCO_{2,atm} drives the sea-air CO₂ flux trends towards a more CO₂ uptake state, whereas oceanic pCO_{2,ocean} is susceptible to internally varying processes:

For intensifying and southward-shifting westerly winds, sea-surface temperature (SST) cooling drives pCO_{2,ocean} decrease ([sec. 4.2.1](#)). Cooling and deeper wind-mixing reduce primary production increasing pCO_{2,ocean} ([sec. 4.2.3](#)). These responses are dominated by a process that cannot be accounted for directly and is likely the increased upper-ocean overturning circulation, which enhances outgassing of deep waters and overall weakens the Southern Ocean carbon sink (summarizing [fig. 5.2](#)).

Vice versa, for weaker and northward-shifting westerly winds the trends in the different processes reverse. Decreasing upwelling and increased primary production result in little oceanic pCO_{2,ocean} decrease, and only combined with the strong atmospheric pCO_{2,atm} increase the Southern Ocean carbon sink increases ([summarizing fig. 5.3](#)).

What can be learned from these large ensemble simulations about the Southern Ocean carbon sink?

[MPI-ESM LE](#) aims to capture model spread due to internal variability. As a free run it produces its own climate and cannot capture the chronology of different climate modes. Analyzing [MPI-ESM LE](#), I find that perturbed initial conditions large ensemble simulations are capable of capturing decadal internal variations similar to observations; even though only for the most extreme decadal trends in [MPI-ESM LE](#) and not in other ensembles such as from [GFDL](#) or [NCAR](#).

Forcing [MPI-ESM](#) with historical CO₂ emissions instead of prescribed pCO_{2,atm} increases internal variability of the global carbon sink by 25% [[Ilyina et al., 2013](#)]. Therefore, in an emission-driven [ESM](#) configuration with interactive carbon cycle, the internal variability of the Southern Ocean carbon sink could be higher.

The strong decadal sea-air CO₂ flux trends discussed in this thesis originate in strong changes of the position and strength of Southern Hemisphere westerly winds and effect of those on ocean circulation. However, the parametrized eddies in [MPI-ESM LE](#) might allow deeper mixing to sustain on longer time-scales than the seasonal timescale at which the eddies could potentially counteract those trends [[Thompson et al., 2011](#)]. The impact of eddies on the carbon cycle in high-resolution simulations, especially in the Southern Ocean, is under current research [[Ito et al., 2010](#); [Dufour et al., 2013](#);

Gnanadesikan et al., 2015; Meredith, 2016]. Only a variable definition of isopycnal thickness diffusion could parametrize the expected eddy response from high-resolution simulations [Gent and Danabasoglu, 2011]. Lovenduski et al., 2013 reproduced these increasing eddy fluxes and the response to the carbon cycle, but the general challenge of differing ocean circulation patterns remains and makes a comparison between a high-resolution resolved eddies and low-resolution parametrized eddies impossible [Bryan et al., 2014]. A future project of high-resolution perturbed initial conditions ensemble simulations would give a more realistic representation of internal variability.

This thesis suggests that even though decadal variations are captured in large ensemble simulations and decadal trends as in Landschützer et al., 2015 are very rare. This raises the question whether biogeochemical processes are missing or implemented in overestimated robustness in models. From an observational perspective, the historically under-sampled Southern Ocean now got equipped with ARGO floats, including 200 floats with biogeochemical sensors. This permits accurate in-situ measurements for the first time during austral winter months and even under ice making it possible to build and constrain biogeochemical models to primary production in melt ponds or under thinning sea-ice. Most models lack this potentially additional variable contribution to the oceanic carbon sink [Long, 2015; Williams et al., 2017; Horvat et al., 2017].

Modeling the Southern Ocean where different water masses converge, faces long-standing challenges with water-column stability. Open-ocean convection appears in models although not observed for decades [de Lavergne et al., 2014; Stössel et al., 2015]. Antarctic sea-ice is underestimated in MPI-ESM [Jungclaus et al., 2013; Notz et al., 2013]. Additional freshwater input from icebergs would stratify the high-latitude Southern Ocean and thereby hinder open-ocean convection and excessive winter mixing [Sallée et al., 2013a; Stössel et al., 2015]. A higher-resolution atmosphere would introduce oceanic counter gyres in the Weddell and Ross Sea, which push the sea-ice edge to more realistic northern extent [Stössel et al., 2015]. Introducing these developments to MPI-ESM would benefit the representation of biogeochemical cycles in HAMOCC.

The history of large ensemble simulations with perturbed initial conditions is fairly recent. The attempt to study internal variability with MPI-ESM LE gives first insights into internal variability from many realizations of simulations. A further promising project would be the comparison of different perturbed initial conditions large ensembles based on different models, i. e. comparing CESM LE, GFDL LE and MPI-ESM LE.

All in all it becomes increasingly important to understand internal varying processes in our climate system in the case of global CO₂ emission reductions, when CO₂ reduction efforts are tracked by measurements and evaluated by scientists and politicians as suggested by the 2015 United Nations Climate Change Conference, COP 21 [Hawkins and Sutton, 2009; United Nations, 2015; McKinley et al., 2016; Lovenduski et al., 2016; Marotzke et al., 2017].

A

APPENDIX

A.1 STATISTICS OF SOUTHERN OCEAN CARBON SINK

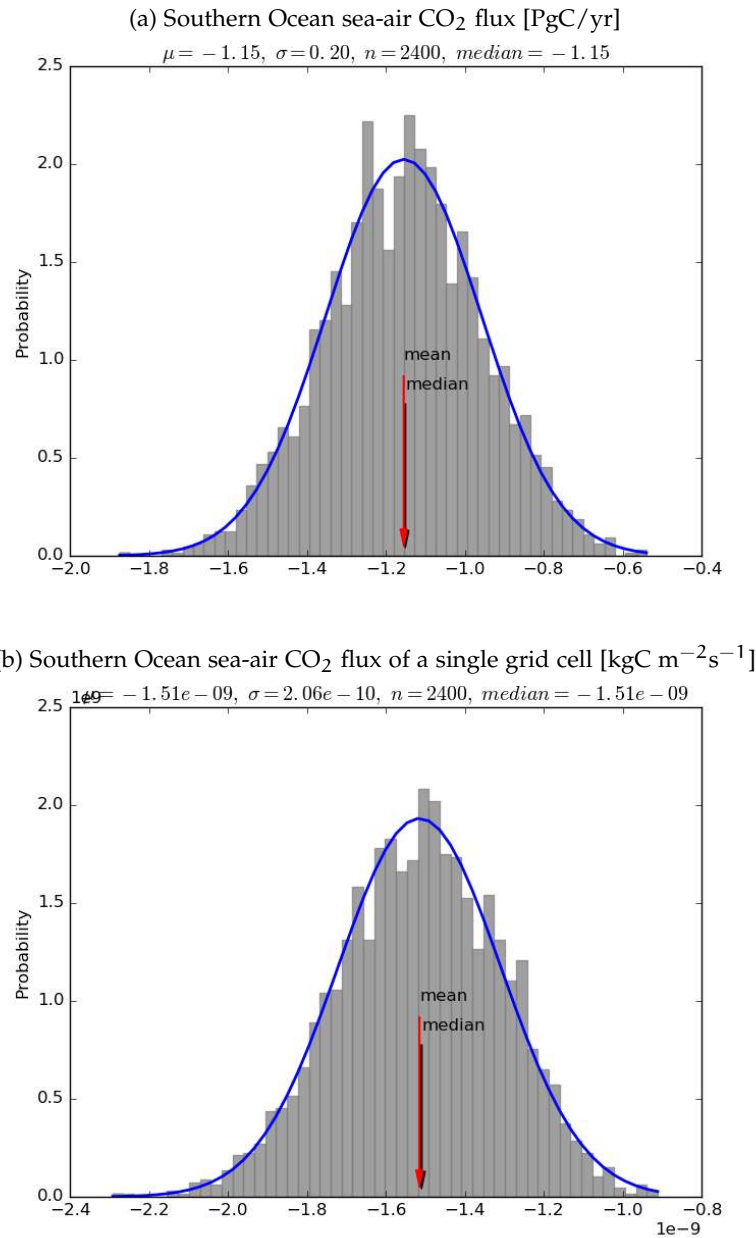


Figure A1: Propability distribution function of the annual sea-air CO₂ flux in the Southern Ocean in ensemble space and temporal space between 1980-2004: (a) field sum over 35-90°S and (b) in a random grid cell.

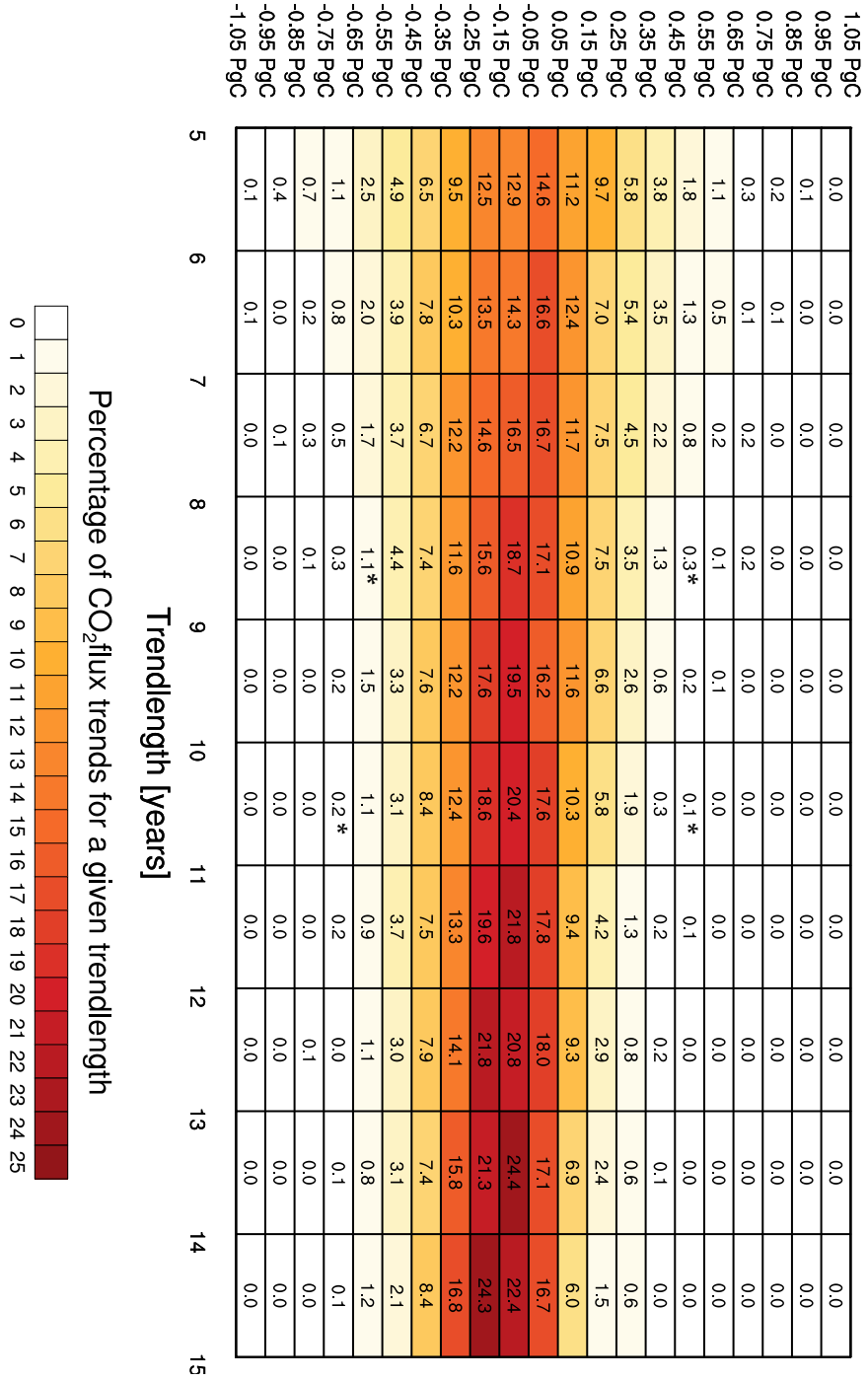
A.2 CO₂ FLUX TRENDSCO₂flux trends heatmap in MPI-ESM Large Ensemble

Figure A2: Southern Ocean carbon sink trends per trend length; * indicate the strongest 8-year and 10-year trends in SOM-FFN

CO₂flux trends heatmap in MPI-ESM Large Ensemble

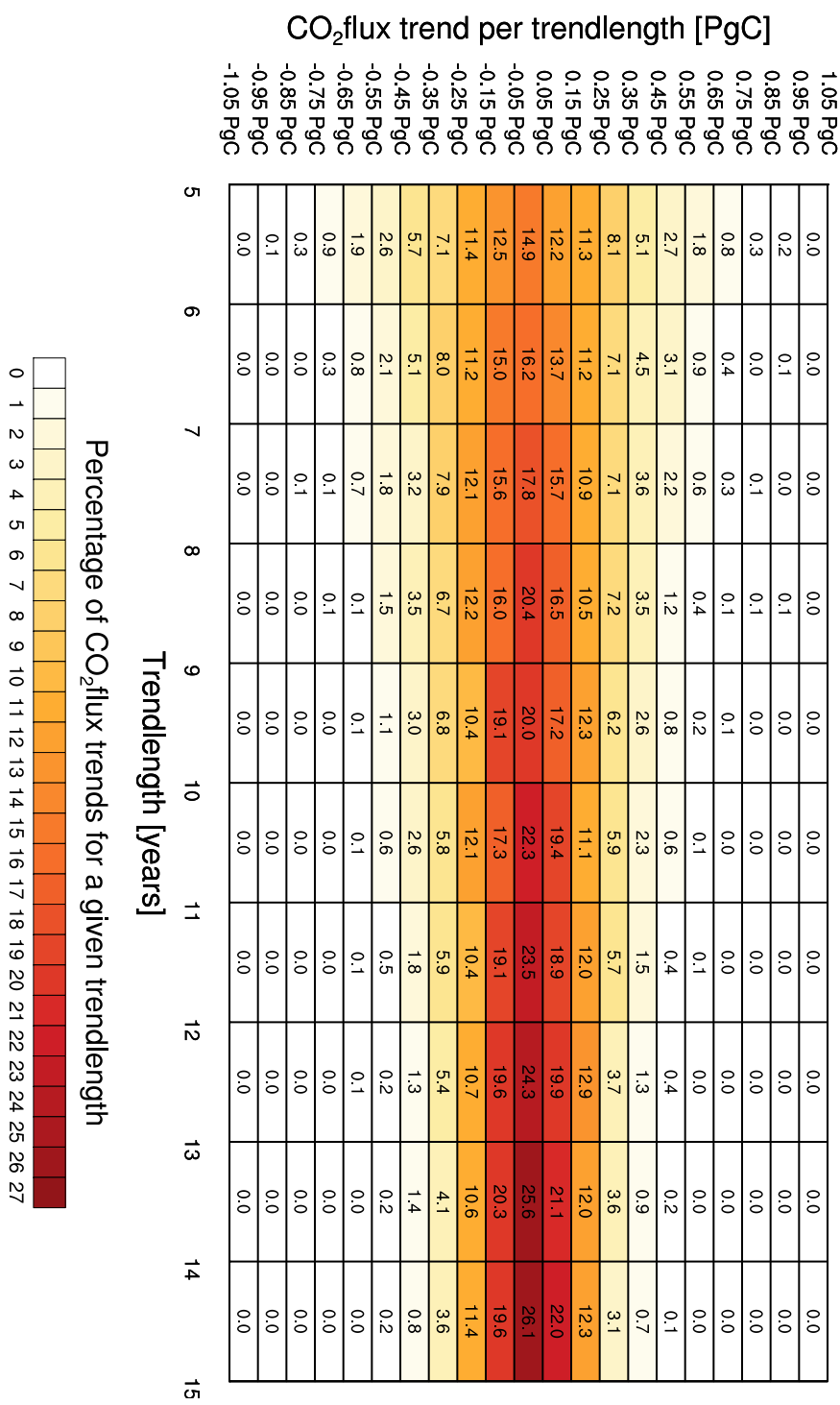


Figure A3: Southern Ocean carbon sink trends per trend length; corrected for forced trend

A.3 MODEL EVALUATION ADDITUM

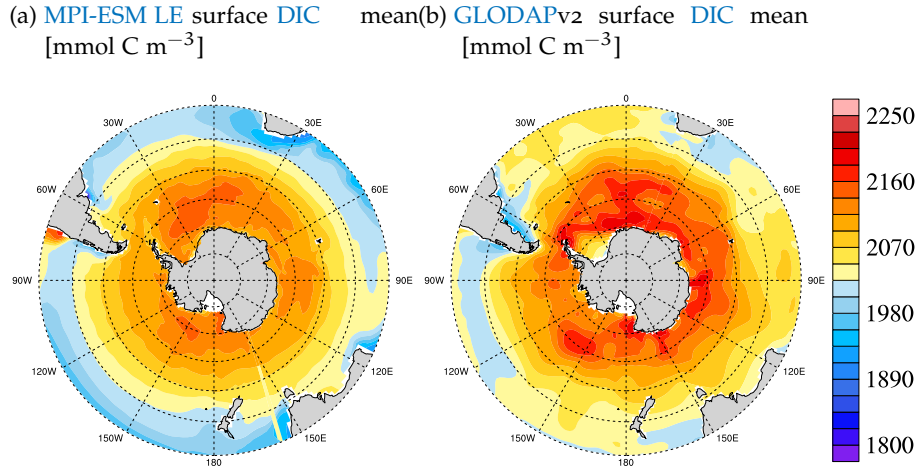


Figure A4: Spatial distribution of the climatology of surface dissolved inorganic carbon (DIC): (a) MPI-ESM LE climatology, (b) Global Ocean Data Analysis Project (GLODAP) Version 2 climatology [Key et al., 2015].

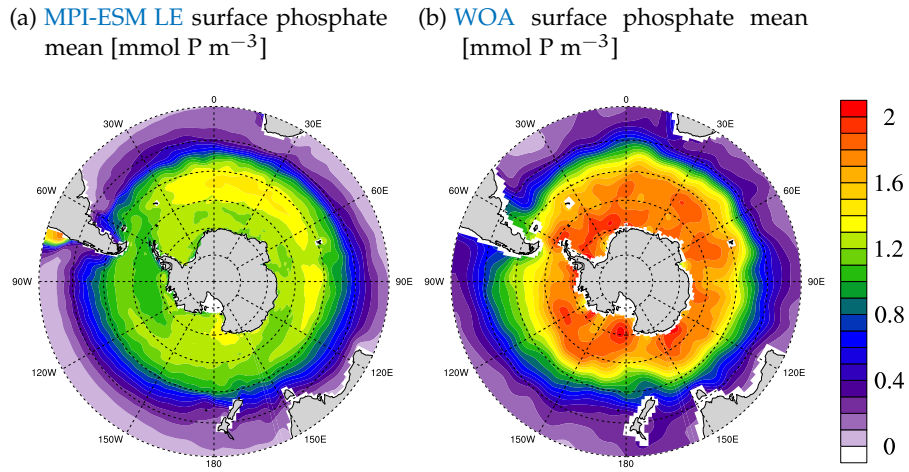


Figure A5: Spatial distribution of the climatology of surface phosphate: (a) MPI-ESM LE climatology, (b) World Ocean Atlas (WOA) climatology [Garcia et al., 2013].

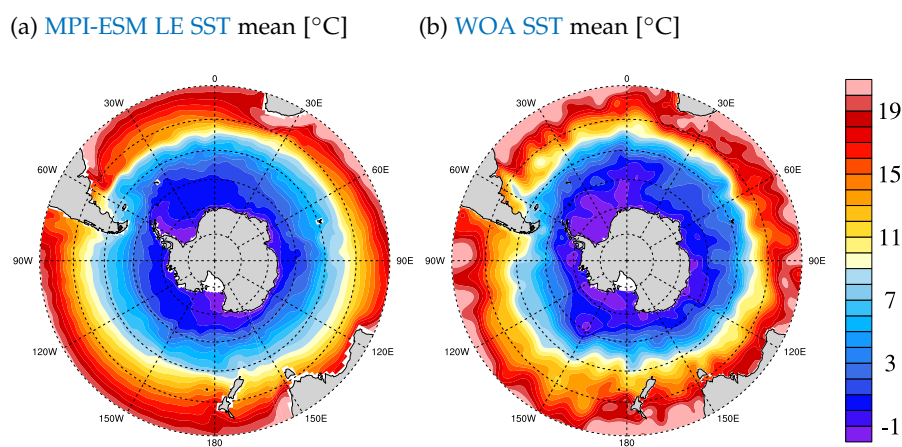


Figure A6: Spatial distribution of the climatology of sea-surface temperature (SST): (a) MPI-ESM LE climatology, (b) WOCE climatology [Gouretski and Koltermann, 2004].

A.4 THERMAL SEPARATION BY SEASONS

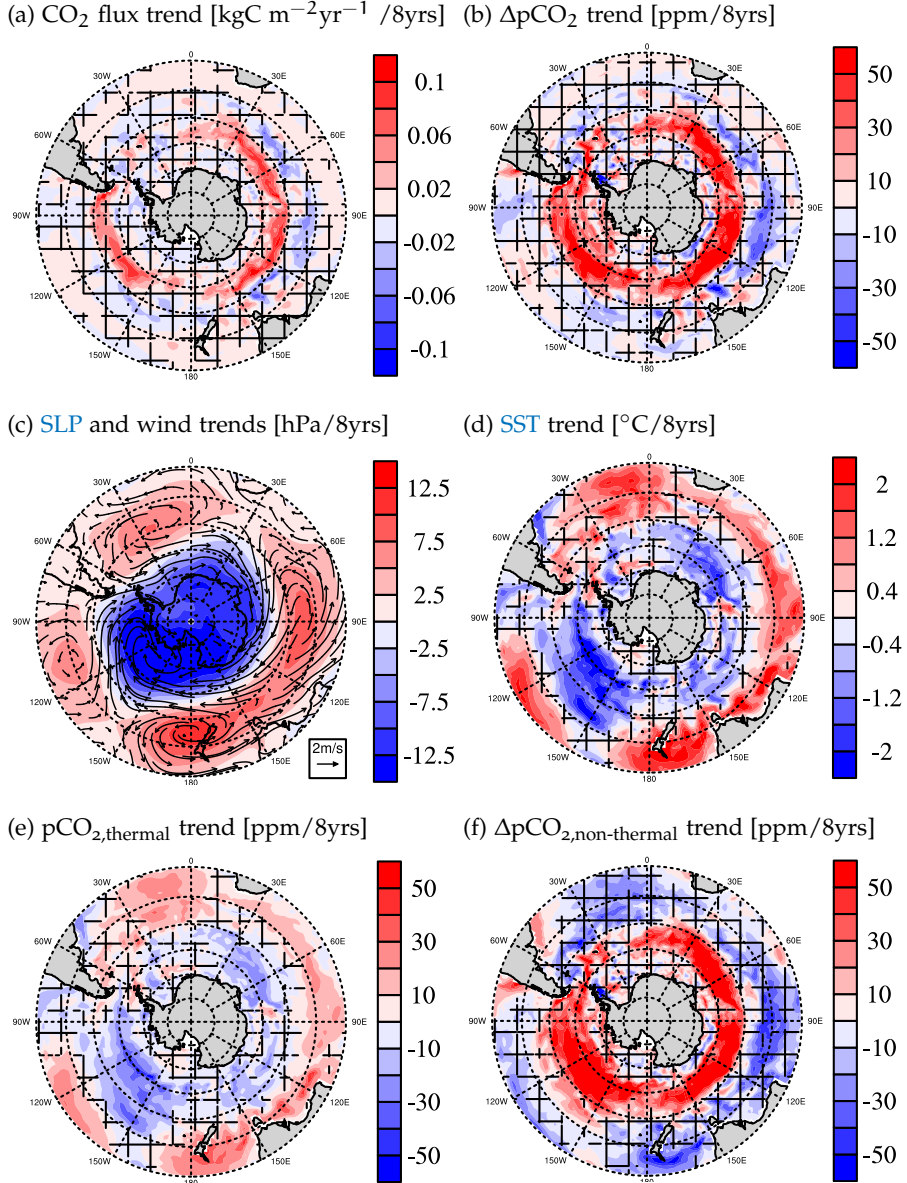
A.4.1 Positive CO_2 flux trend

Figure A7: Linear trends in austral summer during the most positive monotonic 8-year air-sea CO_2 flux trend: (a) sea-air CO_2 flux, (b) $\Delta p\text{CO}_2$, (c) **SLP** and wind vectors overlain as arrows, (d) sea-surface temperature (**SST**), (e) $p\text{CO}_{2,\text{thermal}}$ and (f) $\Delta p\text{CO}_{2,\text{non-thermal}}$; hatched areas indicate where trends are outside the 5% significance level.

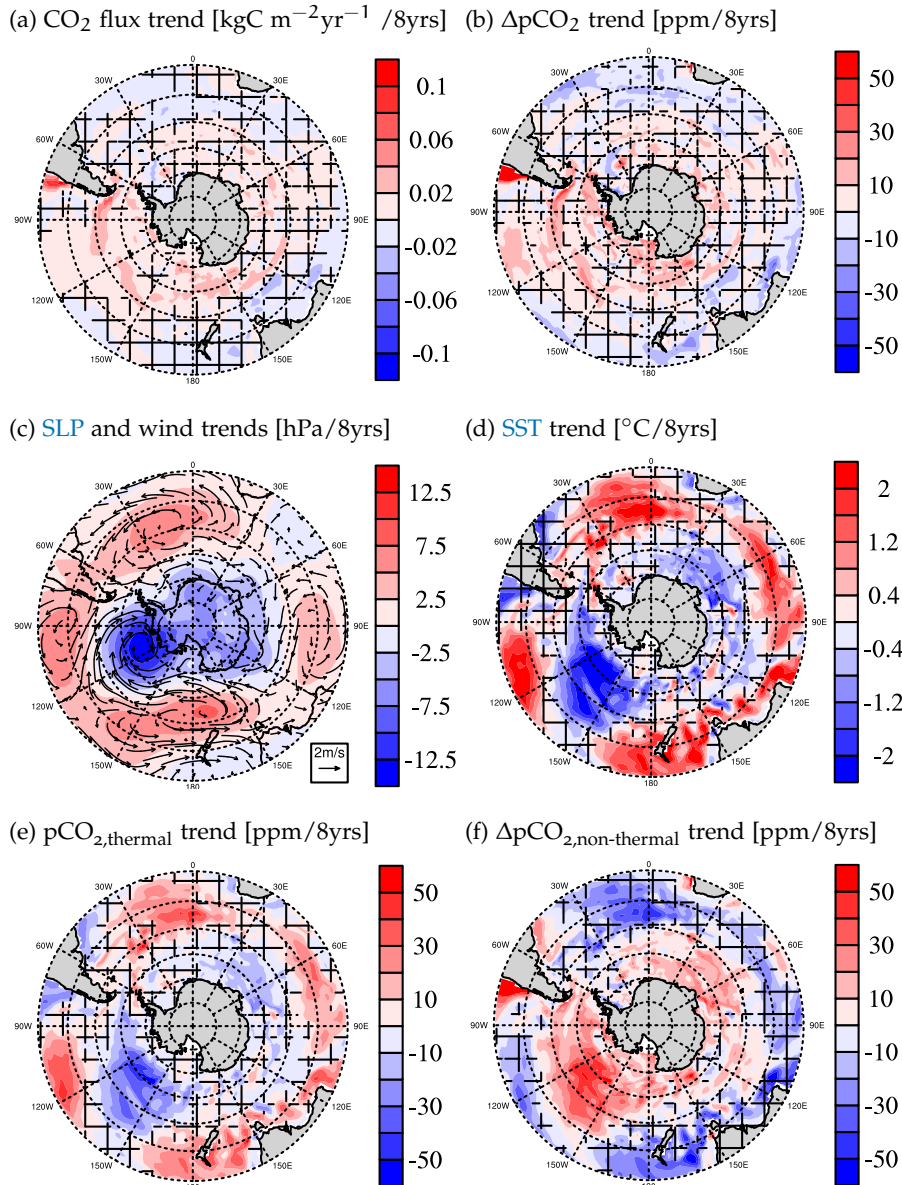


Figure A8: Linear trends in austral winter during the most positive monotonic 8-year sea-air CO_2 flux trend: (a) sea-air CO_2 flux, (b) $\Delta p\text{CO}_2$, (c) SLP and wind vectors overlaid as arrows, (d) sea-surface temperature (SST), (e) $p\text{CO}_{2,\text{thermal}}$ and (f) $\Delta p\text{CO}_{2,\text{non-thermal}}$; hatched areas indicate where trends are outside the 5% significance level.

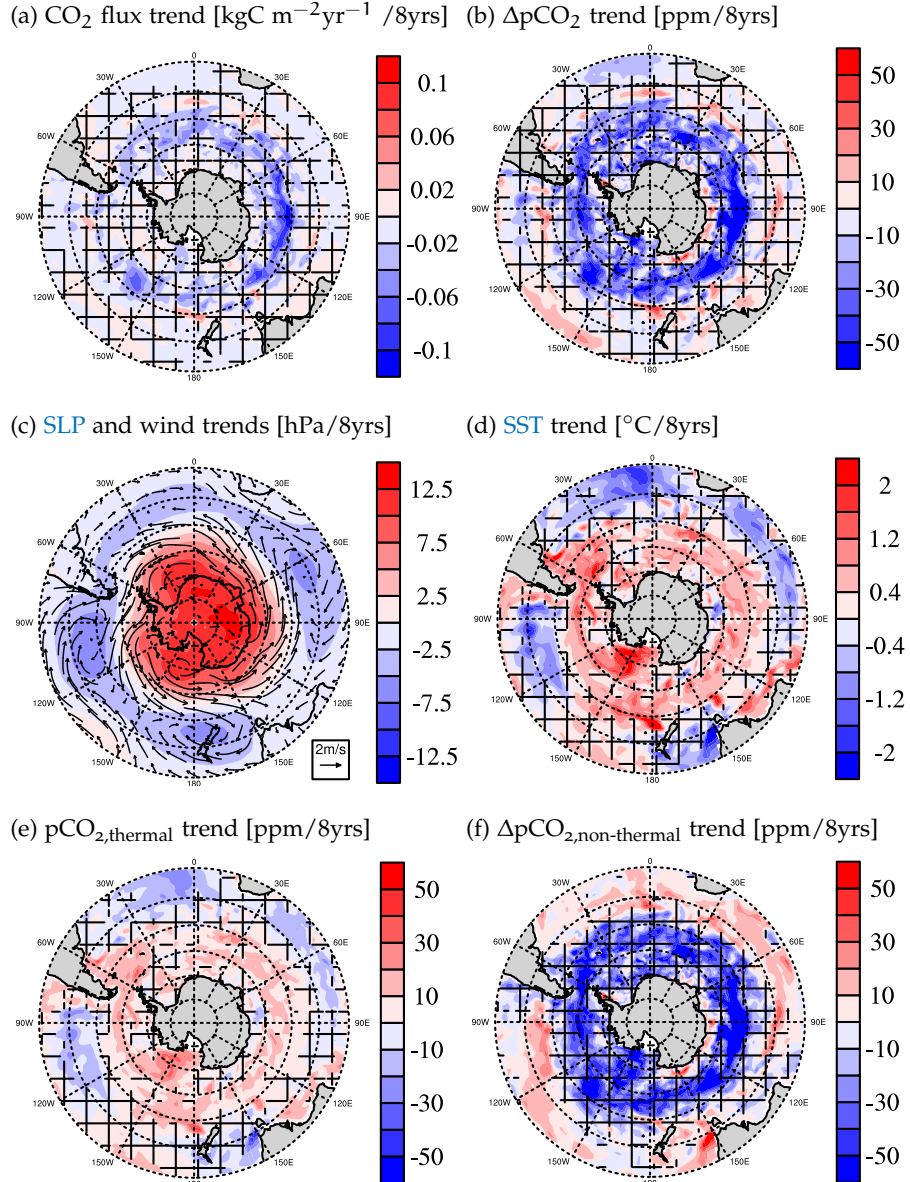
A.5 NEGATIVE CO₂ FLUX TREND

Figure A9: Linear trends in austral summer during the most negative monotonic sea-air 8-year CO₂ flux trend: (a) sea-air CO₂ flux, (b) $\Delta p\text{CO}_2$, (c) SLP and wind vectors overlain as arrows, (d) sea-surface temperature (SST), (e) $p\text{CO}_{2,\text{thermal}}$ and (f) $\Delta p\text{CO}_{2,\text{non-thermal}}$; hatched areas indicate where trends are outside the 5% significance level.

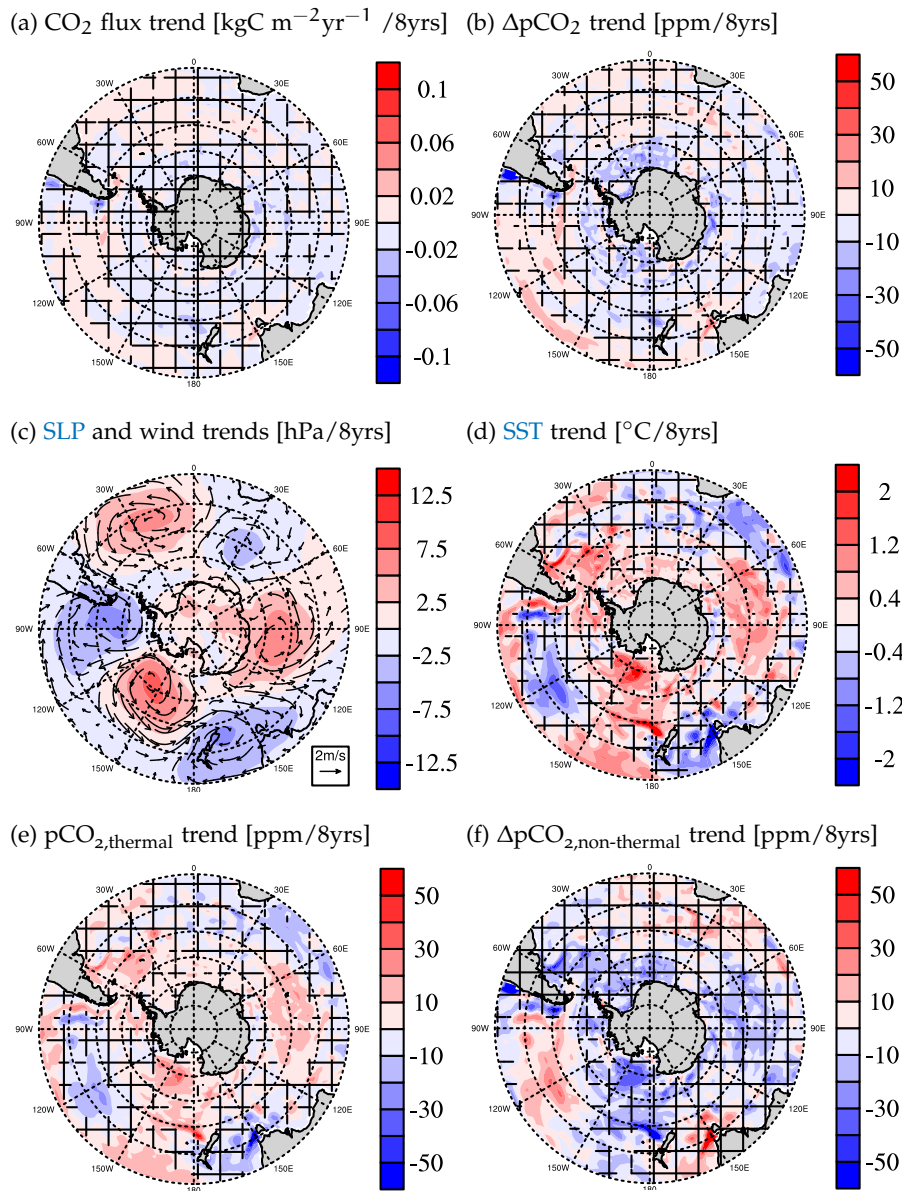


Figure A10: Linear trends in austral winter during the most negative monotonic 8-year sea-air CO₂ flux trend: (a) sea-air CO₂ flux, (b) ΔpCO₂, (c) SLP and wind vectors overlaid as arrows, (d) sea-surface temperature (SST) (e) pCO_{2,thermal} and (f) ΔpCO_{2,non-thermal}; hatched areas indicate where trends are outside the 5% significance level.

A.6 MIS C

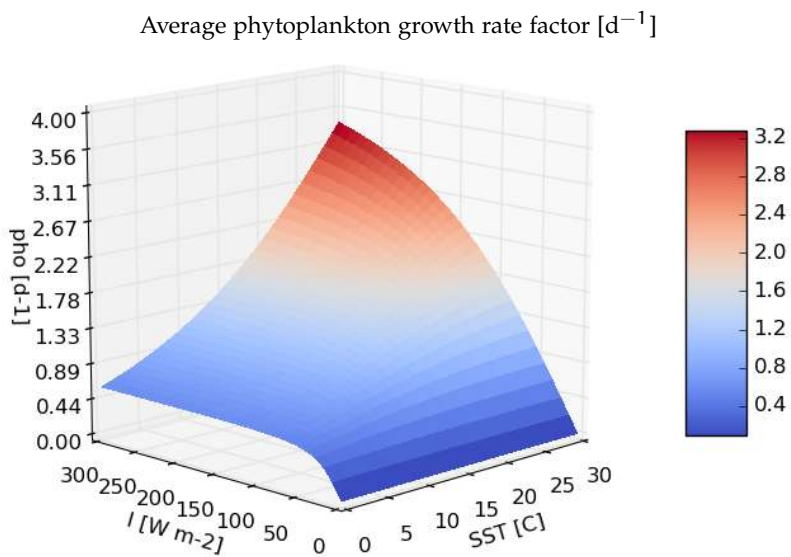


Figure A11: Combined light- & temperature limitation function for the average phytoplankton growth rate in HAMOCC

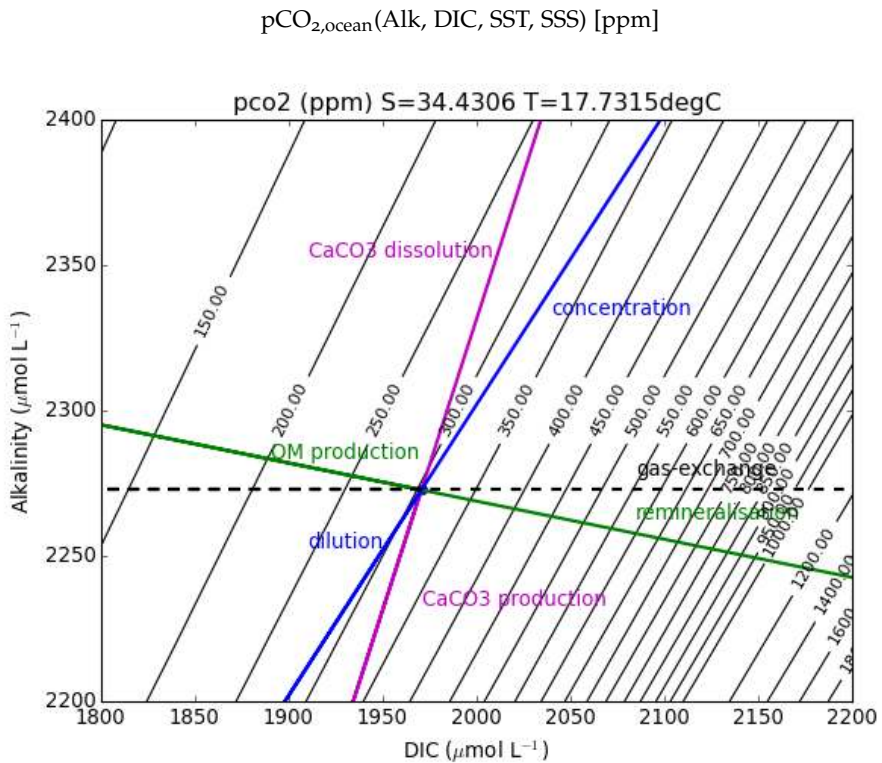


Figure A12: Deffeyes diagram and process contributions

LIST OF FIGURES

Figure 2.1	Schematic overview on the different components in MPI-ESM with prescribed atmospheric partial pressure $p\text{CO}_{2,\text{atm}}$ [Giorgetta et al., 2013]	5
Figure 2.2	Schematic overview of the global ocean biogeochemistry model HAMOCC [Ilyina et al., 2013] which is coupled to the atmospheric model component ECHAM and the ocean model MPIOM . The ocean model provides state variables of physical oceanography, i.e. ice cover, temperature (T), salinity (S) and the advective velocities (\bar{v}). The water column holds tracers of gases, i.e. oxygen (O_2), nitrogen (N_2), laughing gas (N_2O), and dimethyl sulfide (DMS); nutrients, i.e. iron (Fe), phosphate (PO_4), nitrate (NO_3) and silicic acid $\text{Si}(\text{OH})_4$; and tracers of carbonate chemistry, i.e. dissolved inorganic carbon (DIC) and alkalinity (Alk). Photosynthesis converts DIC and nutrients to dissolved organic carbon (DOC), which produces calcium carbonate (CaCO_3) or opal shells.	7
Figure 3.1	Spatial distribution of the climatology (a,c) and decadal internal variability σ_{DIV} (b,d) from 1980-2004 of the Southern Ocean sea-air CO_2 flux: (a) MPI-ESM LE ensemble mean as forced signal, (b) ensemble decadal standard deviation as decadal internal variability σ_{DIV} , (c) SOM-FFN climatology 1982-2004, (d) SOM-FFN decadal variability σ_{DIV} ; negative values indicate ocean uptake.	16

Figure 3.2	Temporal evolution of the Southern Ocean sea-air CO ₂ flux anomaly south of 35°S with respect to the 1980s. Grey lines show the 100 ensemble members, the black line the ensemble mean, the blue shading is the ensemble decadal internal variability σ_{DIV} , the red line shows the most positive 8-year trend, the blue line shows the most negative 8-year trend, the green line represents the SOM-FFN observation-based estimate [Landschützer et al., 2015]; negative values indicate carbon uptake; MPI-ESM LE is extended under RCP4.5 forcing from 2005 to 2015.	17
Figure 3.3	Spatial distribution of the Southern Ocean sea-level pressure (SLP) and wind vectors overlain as arrows: (a) MPI-ESM ensemble mean climatology from 1980 to 2004 as forced signal, (b) ensemble decadal standard deviation as decadal internal variability σ_{DIV} ; (c) difference between MPI-ESM and reanalysis data from NCEP reanalysis climatology [Kalnay et al., 1996], (d) decadal internal variability σ_{DIV} from NCEP reanalysis climatology.	21
Figure 3.4	Temporal evolution of the annual Southern Annular Mode (SAM) index according to [Gong and Wang, 1999]. Grey lines show the 100 ensemble members; the black line the ensemble mean; the blue shading is the decadal internal variability σ_{DIV} ; the red line represents the SAM during positive sea-air CO ₂ flux trend; the blue line during the negative CO ₂ flux trend; the green line shows the station-based SAM from Marshall, 2003.	22
Figure 3.5	Spatial distribution of the vertically integrated primary production in the Southern Ocean: (a) climatological MPI-ESM ensemble mean from 1980 to 2004 as forced signal and (b) ensemble decadal anomaly standard deviation as decadal internal variability σ_{DIV}	24
Figure 3.6	Spatial distribution of surface nitrate in the Southern Ocean: (a) MPI-ESM ensemble mean climatology, (b) World Ocean Atlas (WOA) climatology data [Garcia et al., 2013].	24

Figure 3.7	Temporal evolution of the integrated primary production (INTPP) in the Southern Ocean south of 35°S. Grey lines show the 100 ensemble members, the black line the ensemble mean, the blue shading is the decadal internal variability σ_{DIV} , the red line shows INTPP during the positive CO ₂ flux trend, the blue line during the negative CO ₂ flux trend.	25
Figure 3.8	Zonally averaged transect of the Southern Ocean and the upper-ocean overturning circulation; black arrows show yearly mean advective transports and decadal internal variability σ_{DIV} of (a) water in Sv and (b) carbon in PgC/yr; white lines are isopyncals separating SAMW at potential density $\rho_\theta = 1026.5 \text{ kg m}^{-3}$ from AAIW , at $\rho_\theta = 1027.2 \text{ kg m}^{-3}$ from CDW , at $\rho_\theta = 1027.7 \text{ kg m}^{-3}$ from AABW ; the black line is the MLD ; the colored contours show the distribution of concentration in DIC	28
Figure 3.9	Spatial distribution of mixed-layer depth (MLD) in the Southern Ocean: (a) MPI-ESM ensemble mean climatology, (b) NOAA Atlas climatology [Monterey and Levitus, 1997].	29
Figure 4.1	Linear trends in the SAM as indicator of wind strength vs. sea-air CO ₂ flux at 50-60°S; each data point represents 8-year trends of a single realization normalized for the ensemble mean trend between 1980 and 2004; the blue dot represents the most negative monotonic CO ₂ flux trend; the red dot the positive monotonic CO ₂ flux trend.	32
Figure 4.2	Linear trends during the most positive monotonic 8-year sea-air CO ₂ flux trend: (a) sea-air CO ₂ flux, (b) $\Delta p\text{CO}_2$, (c) SLP and wind vectors overlain as arrows and (d) sea-surface temperature (SST); hatched areas indicate where trends are outside the 5% significance level.	34
Figure 4.3	Linear trends during the most positive monotonic 8-year sea-air CO ₂ flux trend: (a) $p\text{CO}_{2,\text{thermal}}$ and (b) $\Delta p\text{CO}_{2,\text{non-thermal}}$; hatched areas indicate where trends are outside the 5% significance level.	35

Figure 4.4	Linear trends during the most positive 8-year sea-air CO ₂ flux trend: (a) Ekman transport and (b) Ekman pumping; hatched areas indicate where trends are outside the 5% significance level.	36
Figure 4.5	Zonally averaged upper-ocean overturning circulation during the most positive 8-year sea-air CO ₂ flux trend; black arrows show mean advective carbon transport, red arrows show advective carbon transport trends enforcing the upper-ocean overturning circulation; blue arrows show advective carbon transport trends weakening the upper-ocean overturning circulation; black numbers quantify the trends in advective carbon transport in PgC/8yrs; white lines are isopyncals as in fig. 3.8 ; grey line is MLD in the beginning and the black line MLD in the end of the period.	37
Figure 4.6	Southern Ocean austral summer trends during the most positive 8-year sea-air CO ₂ flux trend: (a) integrated primary production (INTPP), (b) nutrient availability factor, (c) surface temperature & limitation function, (d) mixed-layer depth (MLD), (e) average depth of vertical diffusivity due to wind and (f) phytoplankton average depth; hatched areas indicate where trends are outside the 5% significance level.	40
Figure 4.7	Linear trends during the most negative monotonic 8-year air-sea CO ₂ flux trend: (a) sea-air CO ₂ flux, (b) ΔpCO ₂ , (c) SLP and wind vectors overlain as arrows and (d) sea-surface temperature (SST); hatched areas indicate where trends are outside the 5% significance level.	41
Figure 4.8	Linear trends during the most negative monotonic 8-year sea-air CO ₂ flux trend: (a) pCO _{2,thermal} and (b) ΔpCO _{2,non-thermal} ; hatched areas indicate where trends are outside the 5% significance level.	42
Figure 4.9	Linear trends during the most negative 8-years sea-air CO ₂ flux trend: (a) Ekman transport and (b) Ekman pumping; hatched areas indicate where trends are outside the 5% significance level.	43

Figure 4.10	Zonally averaged upper-ocean overturning circulation during the most negative 8-year sea-air CO ₂ flux trend; black arrows show mean advective carbon transport, red arrows show advective carbon transport trends enforcing the upper-ocean overturning circulation; blue arrows show advective carbon transport trends weakening the upper-ocean overturning circulation; black numbers show the trends in advective carbon transport in PgC/8yrs; white lines are isopyncals as in fig. 3.8; grey line is MLD in the beginning and the black line MLD in the end of the period.	44
Figure 4.11	Southern Ocean austral summer trends during the most negative sea-air 8-year CO ₂ flux trend: (a) vertically integrated primary production (INTPP), (b) nutrient availability factor, (c) surface temperature & limitation function, (d) mixed-layer depth (MLD), (e) average depth of vertical diffusivity due to wind and (f) phytoplankton average depth; hatched areas indicate where trends are outside the 5% significance level.	46
Figure 5.1	Schematic illustration of pCO ₂ driver separation assuming a well-mixed zonal box, where changes in pCO _{2,ocean} are separated into contributions due to sea-air CO ₂ flux (red), thermal effect (orange), the saline effect (yellow), freshwater (light blue), biology (green) and a residual (dark blue)	47
Figure 5.2	Schematic illustration of the Southern Ocean under the context of increasing westerly winds and response in the thermal effect, biology and upper-ocean circulation lead towards a positive sea-air CO ₂ flux trend; red color-coding indicates a relative increase of the related quantity or process, whereas blue indicates a relative decrease. The grey line represents the mixed-layer depth (MLD) in the beginning of the trend period, the black line the MLD in the end of the trend period.	54

Figure 5.3	Schematic illustration of the Southern Ocean under the context of decreasing westerly winds and response in the thermal effect, biology and upper-ocean circulation leading towards a negative sea-air CO ₂ flux trend; red color-coding indicates a relative increase of the related quantity or process, grey indicates no changes and blue indicates a relative decrease. The grey line represents the mixed-layer depth (MLD) in the beginning of the trend period, the black line the MLD in the end of the trend period.	56
Figure A1	Probability distribution function of the annual sea-air CO ₂ flux in the Southern Ocean in ensemble space and temporal space between 1980-2004: (a) field sum over 35-90°S and (b) in a random grid cell.	63
Figure A2	Southern Ocean carbon sink trends per trend length; * indicate the strongest 8-year and 10-year trends in SOM-FFN	64
Figure A3	Southern Ocean carbon sink trends per trend length; corrected for forced trend	65
Figure A4	Spatial distribution of the climatology of surface dissolved inorganic carbon (DIC): (a) MPI-ESM LE climatology, (b) Global Ocean Data Analysis Project (GLODAP) Version 2 climatology [Key et al., 2015].	66
Figure A5	Spatial distribution of the climatology of surface phosphate: (a) MPI-ESM LE climatology, (b) World Ocean Atlas (WOA) climatology [Garcia et al., 2013].	66
Figure A6	Spatial distribution of the climatology of sea-surface temperature (SST): (a) MPI-ESM LE climatology, (b) WOCE climatology [Gouretski and Koltermann, 2004].	67
Figure A7	Linear trends in austral summer during the most positive monotonic 8-year air-sea CO ₂ flux trend: (a) sea-air CO ₂ flux, (b) ΔpCO ₂ , (c) SLP and wind vectors overlain as arrows, (d) sea-surface temperature (SST), (e) pCO _{2,thermal} and (f) ΔpCO _{2,non-thermal} ; hatched areas indicate where trends are outside the 5% significance level.	68

Figure A8	Linear trends in austral winter during the most positive monotonic 8-year sea-air CO ₂ flux trend: (a) sea-air CO ₂ flux, (b) ΔpCO ₂ , (c) SLP and wind vectors overlain as arrows, (d) sea-surface temperature (SST), (e) pCO _{2,thermal} and (f) ΔpCO _{2,non-thermal} ; hatched areas indicate where trends are outside the 5% significance level.	69
Figure A9	Linear trends in austral summer during the most negative monotonic sea-air 8-year CO ₂ flux trend: (a) sea-air CO ₂ flux, (b) ΔpCO ₂ , (c) SLP and wind vectors overlain as arrows, (d) sea-surface temperature (SST), (e) pCO _{2,thermal} and (f) ΔpCO _{2,non-thermal} ; hatched areas indicate where trends are outside the 5% significance level.	70
Figure A10	Linear trends in austral winter during the most negative monotonic 8-year sea-air CO ₂ flux trend: (a) sea-air CO ₂ flux, (b) ΔpCO ₂ , (c) SLP and wind vectors overlain as arrows, (d) sea-surface temperature (SST) (e) pCO _{2,thermal} and (f) ΔpCO _{2,non-thermal} ; hatched areas indicate where trends are outside the 5% significance level.	71
Figure A11	Combined light- & temperature limitation function for the average phytoplankton growth rate in HAMOCC	72
Figure A12	Deffeyes diagram and process contributions	72

A.8 LIST OF TABLES

LIST OF TABLES

Table 3.1	Overview of statistical quantities in two trend lengths [TL] in sea-air CO ₂ flux in the Southern Ocean south of 35°S from Max Planck Institute-Earth System Model Large Ensemble (MPI-ESM LE) and Self-Organizing Map-Feed-Forward Network (SOM-FFN) [Landschützer et al., 2015]; positive and negative trends are the most extreme trends in each dataset; the forced signal is subtracted off the corrected trends; probabilities quantify the likelihood that corrected trends are due to internal variability; 8-yr trends are required to be monotonic.	18
Table 5.1	Trends in drivers of pCO ₂ for the most positive sea-air CO ₂ flux trend and the most negative sea-air CO ₂ flux trend in two 10°-MLD boxes. Only austral summer months contribute to biological trends (pCO _{2,bio}).	51

ACRONYMS

MPI	Max Planck Institute for Meteorology Hamburg
HAMOCC	HAMBurg Ocean Carbon Cycle Model
ECHAM	European Center for Medium Range Weather Forecasts HAMburg
MPIOM	Max Planck Institute Ocean Model
ESM	Earth System Model
MPI-ESM	Max Planck Institute-Earth System Model
MPI-ESM LE	Max Planck Institute-Earth System Model Large Ensemble
CMIP5	Coupled Model Intercomparison Project 5
CESM	Community Earth System Model
LE	Large Ensemble

NCAR National Center for Atmospheric Research

NCEP National Centers for Environmental Prediction

GFDL Geophysical Fluid Dynamics Laboratory

NOAA National Oceanic and Atmospheric Administration

WOA World Ocean Atlas

RCP Representative Concentration Pathway

SAM Southern Annular Mode

ENSO El Niño-Southern Oscillation

DIC dissolved inorganic carbon

DOC dissolved organic carbon

INTPP integrated primary production

SST sea-surface temperature

MLD mixed-layer depth

SLP sea-level pressure

ACC Antarctic Circumpolar Current

SAMW Sub-Antarctic Mode Water

AAIW Antarctic Intermediate Water

AABW Antarctic Bottom Water

CDW Circumpolar Deep Water

NPZD NPZD models simulate the interactions of the four variables nutrients (N), phytoplankton (P), zooplankton (Z) and detritus (D).

SOCAT Surface Ocean Atlas

GLODAP Global Ocean Data Analysis Project

SOM-FFN Self-Organizing Map-Feed-Forward Network

BIBLIOGRAPHY

- Bakker, D. C. E. et al. (2014). "An update to the Surface Ocean CO₂ Atlas (SOCAT version 2)." In: *Earth System Science Data* 6.1, pp. 69–90. doi: [10.5194/essd-6-69-2014](https://doi.org/10.5194/essd-6-69-2014) (cit. on p. 10).
- Behrenfeld, Michael J. (2014). "Climate-mediated dance of the plankton." In: *Nature Climate Change* 4.10, pp. 880–887. doi: [10.1038/nclimate2349](https://doi.org/10.1038/nclimate2349) (cit. on p. 23).
- Bittner, Matthias, Hauke Schmidt, Claudia Timmreck, and Frank Sienz (2016). "Using a large ensemble of simulations to assess the Northern Hemisphere stratospheric dynamical response to tropical volcanic eruptions and its uncertainty." In: *Geophysical Research Letters* 43.17. 2016GL070587, pp. 9324–9332. doi: [10.1002/2016GL070587](https://doi.org/10.1002/2016GL070587) (cit. on pp. 6, 9).
- Bopp, L. et al. (2013). "Multiple stressors of ocean ecosystems in the 21st century: projections with CMIP5 models." In: *Biogeosciences* 10.10, pp. 6225–6245. doi: [10.5194/bg-10-6225-2013](https://doi.org/10.5194/bg-10-6225-2013) (cit. on p. 25).
- Bryan, Frank O., Peter R. Gent, and Robert Tomas (2014). "Can Southern Ocean Eddy Effects Be Parameterized in Climate Models?" In: *Journal of Climate* 27, pp. 411–425. doi: [10.1175/JCLI-D-12-00759.1](https://doi.org/10.1175/JCLI-D-12-00759.1) (cit. on p. 61).
- Crutzen, Paul J. (2002). "Geology of mankind." In: *Nature* 415.6867, pp. 23–23. doi: [10.1038/415023a](https://doi.org/10.1038/415023a) (cit. on p. 1).
- DeVries, Tim, Mark Holzer, and Francois Primeau (2017). "Recent increase in oceanic carbon uptake driven by weaker upper-ocean overturning." In: *Nature* 542.7640, pp. 215–218. doi: [10.1038/nature21068](https://doi.org/10.1038/nature21068) (cit. on pp. 27, 32, 36, 43).
- Deppeler, Stacy L. and Andrew T. Davidson (2017). "Southern Ocean Phytoplankton in a Changing Climate." In: *Frontiers in Marine Science* 4. doi: [10.3389/fmars.2017.00040](https://doi.org/10.3389/fmars.2017.00040) (cit. on p. 25).
- Deser, Clara, Adam Phillips, Vincent Bourdette, and Haiyan Teng (2012). "Uncertainty in climate change projections: the role of internal variability." In: *Clim Dyn* 38.3-4, pp. 527–546. doi: [10.1007/s00382-010-0977-x](https://doi.org/10.1007/s00382-010-0977-x) (cit. on pp. 9, 10, 12).
- Döös, Kristofer and David J. Webb (1994). "The Deacon Cell and the Other Meridional Cells of the Southern Ocean." In: *Journal of Physical Oceanography* 24.2, pp. 429–442. doi: [10.1175/1520-0485\(1994\)024<0429:TDCATO>2.0.CO;2](https://doi.org/10.1175/1520-0485(1994)024<0429:TDCATO>2.0.CO;2) (cit. on p. 27).
- Dufour, Carolina O., Julien Le Sommer, Marion Gehlen, James C. Orr, Jean-Marc Molines, Jennifer Simeon, and Bernard Barnier (2013). "Eddy compensation and controls of the enhanced sea-to-air CO₂ flux during positive phases of the Southern Annular Mode." In:

- Global Biogeochemical Cycles* 27.3, pp. 950–961. doi: [10.1002/gbc.20090](https://doi.org/10.1002/gbc.20090) (cit. on p. 60).
- Eppley, Richard W. (1972). “Temperature and phytoplankton growth in the sea.” In: *Fishery Bulletin* 70.4, pp. 1063–1085 (cit. on p. 8).
- Falkowski, P. G., R. T. Barber, and Victor Smetacek (1998). “Biogeochemical Controls and Feedbacks on and Ocean Primary and Production.” In: *Science* 281.5374, pp. 200–206. doi: [10.1126/science.281.5374.200](https://doi.org/10.1126/science.281.5374.200) (cit. on pp. 1, 23).
- Franks, Peter J. S. (2014). “Has Sverdrup’s critical depth hypothesis been tested? Mixed layers vs. turbulent layers.” In: *ICES Journal of Marine Science: Journal du Conseil* 72.6, pp. 1897–1907. doi: [10.1093/icesjms/fsu175](https://doi.org/10.1093/icesjms/fsu175) (cit. on p. 39).
- Garcia, H. E., R. A. Locarnini, T. P. Boyer, J. I. Antonov, O.K. Baranova, M.M. Zweng, J.R. Reagan, and D.R. Johnson (2013). *World Ocean Atlas 2013, Volume 4: Dissolved Inorganic Nutrients (phosphate, nitrate, silicate)*. Ed. by S. Levitus and A. Mishonov. Vol. 76. 25. NOAA Atlas NESDIS. URL: <https://www.nodc.noaa.gov/OC5/woa13/pubwoa13.html> (cit. on pp. 23, 24, 66).
- Gent, Peter R. and Gokhan Danabasoglu (2011). “Response to Increasing Southern Hemisphere Wind in CCSM4.” In: *Journal of Climate* 24, pp. 4992–4998. doi: [10.1175/JCLI-D-10-05011.1](https://doi.org/10.1175/JCLI-D-10-05011.1) (cit. on pp. 32, 61).
- Gent, Peter R., Jurgen Willebrand, Trevor J. McDougall, and James C. McWilliams (1995). “Parameterizing Eddy-Induced Tracer Transports in Ocean Circulation Models.” In: *Journal of Physical Oceanography* 25.4, 463–474. doi: [10.1175/1520-0485\(1995\)025%3C0463:PEITTI%3E2.0.CO;2](https://doi.org/10.1175/1520-0485(1995)025%3C0463:PEITTI%3E2.0.CO;2) (cit. on p. 6).
- Gilbert, R. O. (1987). *Statistical Methods for Environmental Pollution Monitoring*. Wiley (cit. on p. 11).
- Giorgetta, Marco A. et al. (2013). “Climate and carbon cycle changes from 1850 to 2100 in MPI-ESM simulations for the Coupled Model Intercomparison Project phase 5.” In: *Journal of Advances in Modeling Earth Systems* 5.3, pp. 572–597. doi: [10.1002/jame.20038](https://doi.org/10.1002/jame.20038) (cit. on p. 5).
- Gnanadesikan, Anand, Marie-Aude Pradal, and Ryan Abernathey (2015). “Isopycnal mixing by mesoscale eddies significantly impacts oceanic anthropogenic carbon uptake.” In: *Geophysical Research Letters* 42.11, pp. 4249–4255. doi: [10.1002/2015gl064100](https://doi.org/10.1002/2015gl064100) (cit. on p. 61).
- Gong, Daoyi and Shaowu Wang (1999). “Definition of Antarctic Oscillation index.” In: *Geophysical Research Letters* 26.4, pp. 459–462. doi: [10.1029/1999GL900003](https://doi.org/10.1029/1999GL900003) (cit. on pp. 12, 20, 22).
- Gouretski, V. V. and K. P. Koltermann (2004). *WOCE Global Hydrographic Climatology*. Tech. rep. Bundesamt für Seeschifffahrt und Hydrographie (cit. on p. 67).
- Hall, Alex and Martin Visbeck (2002). “Synchronous Variability in the Southern Hemisphere Atmosphere, Sea Ice, and Ocean Resulting

- from the Annular Mode." In: *Journal of Climate* 15.21, pp. 3043–3057. DOI: [10.1175/1520-0442\(2002\)015<3043:SVITSH>2.0.CO;2](https://doi.org/10.1175/1520-0442(2002)015<3043:SVITSH>2.0.CO;2) (cit. on pp. 31, 35, 42).
- Hauck, J., C. Völker, T. Wang, M. Hoppema, M. Losch, and D. A. Wolf-Gladrow (2013). "Seasonally different carbon flux changes in the Southern Ocean in response to the southern annular mode." In: *Global Biogeochemical Cycles* 27.4, pp. 1236–1245. DOI: [10.1002/2013gb004600](https://doi.org/10.1002/2013gb004600) (cit. on pp. 31, 38, 45).
- Haumann, F. Alexander, Dirk Notz, and Hauke Schmidt (2014). "Anthropogenic influence on recent circulation-driven Antarctic sea ice changes." In: *Geophysical Research Letters* 41.23, pp. 8429–8437. DOI: [10.1002/2014gl061659](https://doi.org/10.1002/2014gl061659) (cit. on p. 33).
- Hawkins, Ed and Rowan Sutton (2009). "The Potential to Narrow Uncertainty in Regional Climate Predictions." In: *Bulletin of the American Meteorological Society* 90.8, pp. 1095–1107. DOI: [10.1175/2009BAMS2607.1](https://doi.org/10.1175/2009BAMS2607.1) (cit. on pp. 10, 62).
- Hedemann, Christopher, Thorsten Mauritsen, Johann Jungclaus, and Jochem Marotzke (2017). "The subtle origins of surface-warming hiatuses." In: *Nature Climate Change* 7.5, pp. 336–339. DOI: [10.1038/nclimate3274](https://doi.org/10.1038/nclimate3274) (cit. on p. 9).
- Heinze, C., E. Maier-Reimer, A. M. E. Winguth, and D. Archer (1999). "A global oceanic sediment model for long-term climate studies." In: *Global Biogeochemical Cycles* 13.1, pp. 221–250. DOI: [10.1029/98GB02812](https://doi.org/10.1029/98GB02812) (cit. on p. 8).
- Heinze, C., S. Meyer, N. Goris, L. Anderson, R. Steinfeldt, N. Chang, C. Le Quéré, and D. C. E. Bakker (2015). "The ocean carbon sink – impacts, vulnerabilities and challenges." In: *Earth System Dynamics* 6.1, pp. 327–358. DOI: [10.5194/esd-6-327-2015](https://doi.org/10.5194/esd-6-327-2015) (cit. on p. 1).
- Heuzé, Céline, Karen J. Heywood, David P. Stevens, and Jeff K. Ridley (2013). "Southern Ocean bottom water characteristics in CMIP5 models." In: *Geophys. Res. Lett.* 40.7, pp. 1409–1414. DOI: [10.1002/grl.50287](https://doi.org/10.1002/grl.50287) (cit. on p. 29).
- Hirsch, R.M., J.R. Slack, and R.A. Smith (1982). "Techniques of trend analysis for monthly water quality data." In: *Water Resources Research* 18.1, pp. 107–121 (cit. on p. 11).
- Horvat, Christopher, David Rees Jones, Sarah Iams, David Schroeder, Daniela Flocco, and Daniel Feltham (2017). "The frequency and extent of sub-ice phytoplankton blooms in the Arctic ocean." In: *Science Advances* (cit. on p. 61).
- IPCC (2013). *Climate Change 2013: The Physical Science Basis. Contribution of Working Group I to the Fifth Assessment Report on the Intergovernmental Panel on Climate Change*. Ed. by T. F. Stocker et al. Cambridge University Press. URL: <http://ipcc.ch/report/ar5/> (cit. on p. 9).
- Ilyina, Tatiana (2016). "Hidden trends in the ocean carbon sink." In: *Nature* 530.7591, pp. 426–427. DOI: [10.1038/530426a](https://doi.org/10.1038/530426a) (cit. on p. 9).

- Ilyina, Tatiana, Katharina D. Six, Joachim Segschneider, Ernst Maier-Reimer, Hongmei Li, and Ismael Núñez-Riboni (2013). "Global ocean biogeochemistry model HAMOCC: Model architecture and performance as component of the MPI-Earth system model in different CMIP5 experimental realizations." In: *Journal of Advances in Modeling Earth Systems* 5.2, pp. 287–315. DOI: [10.1029/2012MS000178](https://doi.org/10.1029/2012MS000178) (cit. on pp. 5–7, 15, 18, 60).
- Ito, T., M. Woloszyn, and M. Mazloff (2010). "Anthropogenic carbon dioxide transport in the Southern Ocean driven by Ekman flow." In: *Nature* 463.7277, pp. 80–83. DOI: [10.1038/nature08687](https://doi.org/10.1038/nature08687) (cit. on p. 60).
- Jungclaus, J. H., N. Fischer, H. Haak, K. Lohmann, J. Marotzke, D. Matei, U. Mikolajewicz, D. Notz, and J. S. von Storch (2013). "Characteristics of the ocean simulations in the Max Planck Institute Ocean Model (MPIOM) the ocean component of the MPI-Earth system model." In: *Journal of Advances in Modeling Earth Systems* 5.2, pp. 422–446. DOI: [10.1002/jame.20023](https://doi.org/10.1002/jame.20023) (cit. on pp. 5, 6, 26, 28, 61).
- Kalnay, E. et al. (1996). "The NCEP/NCAR 40-Year Reanalysis Project." In: *Bulletin of the American Meteorological Society* 77.3, 437–471. DOI: [10.1175/1520-0477\(1996\)077%3C0437:TNYRP%3E2.0.CO;2](https://doi.org/10.1175/1520-0477(1996)077%3C0437:TNYRP%3E2.0.CO;2) (cit. on pp. 20, 21).
- Kay, J. E. et al. (2015). "The Community Earth System Model (CESM) Large Ensemble Project: A Community Resource for Studying Climate Change in the Presence of Internal Climate Variability." In: *Bull. Amer. Meteor. Soc.* 96.8, pp. 1333–1349. DOI: [10.1175/bams-d-13-00255.1](https://doi.org/10.1175/bams-d-13-00255.1) (cit. on p. 9).
- Keeling, Charles D., Holger Brix, and Nicolas Gruber (2004). "Seasonal and long-term dynamics of the upper ocean carbon cycle at Station ALOHA near Hawaii." In: *Global Biogeochemical Cycles* 18.4. GB4006. DOI: [10.1029/2004GB002227](https://doi.org/10.1029/2004GB002227) (cit. on p. 48).
- Kendall, M. G. (1975). *Rank Correlation Methods*. Charles Griffin (cit. on p. 11).
- Kessler, A. and J. Tjiputra (2016). "The Southern Ocean as a constraint to reduce uncertainty in future ocean carbon sinks." In: *Earth Syst. Dynam.* 7.2, pp. 295–312. DOI: [10.5194/esd-7-295-2016](https://doi.org/10.5194/esd-7-295-2016) (cit. on pp. 1, 25).
- Key, R. M. et al. (2015). *GLOBAL OCEAN DATA ANALYSIS PROJECT, VERSION 2*. Tech. rep. Climate Change Research Division Office of Biological and Environmental Research, U.S. Department of Energy. URL: <http://cdiac.ornl.gov/oceans/GLODAPv2/> (cit. on p. 66).
- Kidston, J. and E. P. Gerber (2010). "Intermodel variability of the poleward shift of the austral jet stream in the CMIP3 integrations linked to biases in 20th century climatology." In: *Geophysical Re-*

- search Letters* 37.9. L09708. doi: [10.1029/2010GL042873](https://doi.org/10.1029/2010GL042873) (cit. on p. 20).
- Krumhardt, Kristen M., Nicole S. Lovenduski, Matthew C. Long, and Keith Lindsay (2017). "Avoidable impacts of ocean warming on marine primary production: Insights from the CESM ensembles." In: *Global Biogeochemical Cycles* 31.1, pp. 114–133. doi: [10.1002/2016gb005528](https://doi.org/10.1002/2016gb005528) (cit. on pp. 9, 25).
- Landschützer, P., N. Gruber, D. C. E. Bakker, U. Schuster, S. Nakaoka, M. R. Payne, T. P. Sasse, and J. Zeng (2013). "A neural network-based estimate of the seasonal to inter-annual variability of the Atlantic Ocean carbon sink." In: *Biogeosciences* 10.11, pp. 7793–7815. doi: [10.5194/bg-10-7793-2013](https://doi.org/10.5194/bg-10-7793-2013) (cit. on p. 10).
- Landschützer, P., N. Gruber, D. C. E. Bakker, and U. Schuster (2014). "Recent variability of the global ocean carbon sink." In: *Global Biogeochemical Cycles* 28.9, pp. 927–949. doi: [10.1002/2014gb004853](https://doi.org/10.1002/2014gb004853) (cit. on p. 10).
- Landschützer, Peter et al. (2015). "The reinvigoration of the Southern Ocean carbon sink." In: *Science* 349.6253, pp. 1221–1224. doi: [10.1126/science.aab2620](https://doi.org/10.1126/science.aab2620) (cit. on pp. 1, 17–19, 31, 35, 43, 59, 61).
- Landschützer, Peter, Nicolas Gruber, and Dorothee C. E. Bakker (2016). "Decadal variations and trends of the global ocean carbon sink." In: *Global Biogeochemical Cycles* 30.10, pp. 1396–1417. doi: [10.1002/2015gb005359](https://doi.org/10.1002/2015gb005359) (cit. on pp. 10, 16).
- Lauderdale, Jonathan M., Alberto C. Naveira Garabato, Kevin I. C. Oliver, Michael J. Follows, and Richard G. Williams (2013). "Wind-driven changes in Southern Ocean residual circulation, ocean carbon reservoirs and atmospheric CO₂." In: *Climate Dynamics* 41.7, pp. 2145–2164. doi: [10.1007/s00382-012-1650-3](https://doi.org/10.1007/s00382-012-1650-3) (cit. on pp. 36, 43).
- Le Quéré, Corinne et al. (2007). "Saturation of the Southern Ocean CO₂ Sink Due to Recent Climate Change." In: *Science* 316.5832, pp. 1735–1738. doi: [10.1126/science.1136188](https://doi.org/10.1126/science.1136188) (cit. on pp. 31, 36).
- Le Quéré, Corinne et al. (2016). "Global Carbon Budget 2016." In: *Earth System Science Data* 8.2, pp. 605–649. doi: [10.5194/essd-8-605-2016](https://doi.org/10.5194/essd-8-605-2016) (cit. on p. 1).
- Long, Matthew C. (2015). "The Southern Ocean and the Global Carbon Cycle." In: NCAR (cit. on p. 61).
- Lovenduski, Nicole S. and Nicolas Gruber (2005). "Impact of the Southern Annular Mode on Southern Ocean circulation and biology." In: *Geophys. Res. Lett.* 32.L11603. doi: [10.1029/2005GL022727](https://doi.org/10.1029/2005GL022727) (cit. on p. 38).
- Lovenduski, Nicole S., Nicolas Gruber, Scott C. Doney, and Ivan D. Lima (2007). "Enhanced CO₂ outgassing in the Southern Ocean from a positive phase of the Southern Annular Mode." In: *Global Biogeochemical Cycles* 21.2. GB2026. doi: [10.1029/2006GB002900](https://doi.org/10.1029/2006GB002900) (cit. on pp. 2, 15, 31, 34, 36, 47, 53).

- Lovenduski, Nicole S., Nicolas Gruber, and Scott C. Doney (2008). "Toward a mechanistic understanding of the decadal trends in the Southern Ocean carbon sink." In: *Global Biogeochem. Cycles* 22. doi: [10.1029/2007GB003139](https://doi.org/10.1029/2007GB003139) (cit. on pp. 31, 36).
- Lovenduski, Nicole S., Matthew C. Long, Peter R. Gent, and Keith Lindsay (2013). "Multi-decadal trends in the advection and mixing of natural carbon in the Southern Ocean." In: *Geophys. Res. Lett.* 40. doi: [10.1029/2012GL054483](https://doi.org/10.1029/2012GL054483) (cit. on pp. 32, 61).
- Lovenduski, Nicole S., Amanda R. Fay, and Galen A. McKinley (2015). "Observing multidecadal trends in Southern Ocean CO₂ uptake: What can we learn from an ocean model?" In: *Global Biogeochem. Cycles* 29.4, pp. 416–426. doi: [10.1002/2014gb004933](https://doi.org/10.1002/2014gb004933) (cit. on pp. 31, 32, 34, 35, 43).
- Lovenduski, Nicole S., Galen A. McKinley, Amanda R. Fay, Keith Lindsay, and Matthew C. Long (2016). "Partitioning uncertainty in ocean carbon uptake projections: Internal variability, emission scenario, and model structure." In: *Global Biogeochemical Cycles* 30.9, pp. 1276–1287. doi: [10.1002/2016gb005426](https://doi.org/10.1002/2016gb005426) (cit. on pp. 9, 10, 62).
- Lozier, M. Susan, Apurva C. Dave, Jaime B. Palter, Lisa M. Gerber, and Richard T. Barber (2011). "On the relationship between stratification and primary productivity in the North Atlantic." In: *Geophysical Research Letters* 38.18. L18609. doi: [10.1029/2011GL049414](https://doi.org/10.1029/2011GL049414) (cit. on p. 25).
- Maier-Reimer, Ernst (1984). "Toward a Global Ocean Carbon Model." In: *Progress in Biometeorology* 3, pp. 295–310 (cit. on p. 6).
- Maier-Reimer, Ernst (1993). "Geochemical Cycles in an Ocean General Circulation Model Preindustrial Tracer Distributions." In: *Global Biogeochem. Cycles* 7.3, pp. 645–677. doi: [10.1029/93GB01355](https://doi.org/10.1029/93GB01355) (cit. on pp. 6, 7).
- Mann, H. B. (1945). "Non-parametric tests against trend." In: *Econometrica* 13, pp. 163–171 (cit. on p. 11).
- Margalef, Ramon (1997). "Turbulence and marine life." In: *Scientia Marina* 61, pp. 109–123. URL: <http://scimar.icm.csic.es/scimar/pdf/61/sm61s1109.pdf> (cit. on p. 39).
- Marotzke, Jochem et al. (2017). "Climate research must sharpen its view." In: *Nature Climate Change* 7, pp. 89–91. doi: [10.1038/nclimate3206](https://doi.org/10.1038/nclimate3206) (cit. on p. 62).
- Marshall, Gareth J. (2003). "Trends in the Southern Annular Mode from Observations and Reanalyses." In: *Journal of Climate* 16.24, pp. 4134–4143. doi: [10.1175/1520-0442\(2003\)016<4134:TITSAM>2.0.CO;2](https://doi.org/10.1175/1520-0442(2003)016<4134:TITSAM>2.0.CO;2) (cit. on pp. 21, 22, 32, 43).
- Marshall, John and Kevin Speer (2012). "Closure of the meridional overturning circulation through Southern Ocean upwelling." In: *Nature Geoscience* 5.3, pp. 171–180. doi: [10.1038/ngeo1391](https://doi.org/10.1038/ngeo1391) (cit. on p. 27).

- Martin, John H. (1990). "Glacial-interglacial CO₂ change: The Iron Hypothesis." In: *Paleoceanography* 5.1, pp. 1–13. doi: [10.1029/PA005i001p00001](https://doi.org/10.1029/PA005i001p00001) (cit. on p. 38).
- Martin, John H., R. Michael Gordon, and Steve E. Fitzwater (1990). "Iron in Antarctic waters." In: *Nature* 345, pp. 156–158. doi: [10.1038/345156a0](https://doi.org/10.1038/345156a0) (cit. on p. 38).
- McKinley, Galen A., Darren J. Pilcher, Amanda R. Fay, Keith Lindsay, Matthew C. Long, and Nicole S. Lovenduski (2016). "Timescales for detection of trends in the ocean carbon sink." In: *Nature* 530.7591, pp. 469–472. doi: [10.1038/nature16958](https://doi.org/10.1038/nature16958) (cit. on pp. 2, 9, 10, 62).
- Meredith, Michael P. (2016). "Understanding the structure of changes in the Southern Ocean eddy field." In: *Geophys. Res. Lett.* 43.11, pp. 5829–5832. doi: [10.1002/2016gl069677](https://doi.org/10.1002/2016gl069677) (cit. on p. 61).
- Michaelis, L. and M. L. Menten (1913). "Die Kinetik der Invertinwirkung." In: *Biochem. Z.* 49, pp. 333–369 (cit. on p. 8).
- Monterey, G. and S. Levitus (1997). *Seasonal Variability of the Mixed Layer Depth for the World Ocean*. Research rep. NOAA Atlas NESDIS 14. URL: <https://www.nodc.noaa.gov/OC5/WOA94/mix.html> (cit. on p. 29).
- Mood, A. M., F. A. Graybill, and D. C. Boes (1974). *Introduction to the Theory of Statistics*. McGraw-Hill (cit. on p. 11).
- Morrison, AdeleK., ThomasL. Frölicher, and JorgeL. Sarmiento (2015). "Upwelling in the Southern Ocean." In: *Physics Today*. doi: [10.1063/PT.3.2654](https://doi.org/10.1063/PT.3.2654) (cit. on pp. 1, 27).
- Murphy, James M., David M. H. Sexton, David N. Barnett, Gareth S. Jones, Mark J. Webb, Matthew Collins, and David A. Stainforth (2004). "Quantification of modelling uncertainties in a large ensemble of climate change simulations." In: *Nature* 430.7001. 10.1038/nature02771, 768–772. doi: [10.1038/nature02771](https://doi.org/10.1038/nature02771) (cit. on p. 1).
- Nevison, C. D., M. Manizza, R. F. Keeling, M. Kahru, L. Bopp, J. Dunne, J. Tiputra, T. Ilyina, and B. G. Mitchell (2015). "Evaluating the ocean biogeochemical components of Earth system models using atmospheric potential oxygen and ocean color data." In: *Biogeosciences* 12.1, pp. 193–208. doi: [10.5194/bg-12-193-2015](https://doi.org/10.5194/bg-12-193-2015) (cit. on p. 25).
- Nevison, C. D. et al. (2016). "Evaluating CMIP5 ocean biogeochemistry and Southern Ocean carbon uptake using atmospheric potential oxygen: Present-day performance and future projection." In: *Geophys. Res. Lett.* 43.5, pp. 2077–2085. doi: [10.1002/2015gl067584](https://doi.org/10.1002/2015gl067584) (cit. on p. 25).
- Notz, Dirk, F. Alexander Haumann, Helmuth Haak, Johann H. Jungclaus, and Jochem Marotzke (2013). "Arctic sea-ice evolution as modeled by Max Planck Institute for Meteorology's Earth system model." In: *Journal of Advances in Modeling Earth Systems* 5.2, 173–194. doi: [10.1002/jame.20016](https://doi.org/10.1002/jame.20016) (cit. on p. 61).

- Orsi, Alejandro H., Thomas Whitworth, and Worth D. Nowlin (1995). "On the meridional extent and fronts of the Antarctic Circumpolar Current." In: *Deep Sea Research Part I: Oceanographic Research Papers* 42.5, pp. 641–673. DOI: [10.1016/0967-0637\(95\)00021-W](https://doi.org/10.1016/0967-0637(95)00021-W) (cit. on p. 23).
- Pacanowski, R. C. and S. G. H. Philander (1981). "Parameterization of Vertical Mixing in Numerical Models of Tropical Oceans." In: *Journal of Physical Oceanography* 11.11, pp. 1443–1451. DOI: [10.1175/1520-0485\(1981\)011<1443:POVMIN>2.0.CO;2](https://doi.org/10.1175/1520-0485(1981)011<1443:POVMIN>2.0.CO;2) (cit. on p. 6).
- Reick, C. H., T. Raddatz, V. Brovkin, and V. Gayler (2013). "Representation of natural and anthropogenic land cover change in MPI-ESM." In: *Journal of Advances in Modeling Earth Systems* 5.3, pp. 459–482. DOI: [10.1002/jame.20022](https://doi.org/10.1002/jame.20022) (cit. on p. 5).
- Rödenbeck, C., R. F. Keeling, D. C. E. Bakker, N. Metzl, A. Olsen, C. Sabine, and M. Heimann (2013). *Global surface-ocean CO₂ and sea-air CO₂ flux variability from an observation-driven ocean mixed-layer scheme*. 2. Copernicus GmbH, pp. 193–216. DOI: [10.5194/os-9-193-2013](https://doi.org/10.5194/os-9-193-2013) (cit. on pp. 1, 10).
- Rödenbeck, C., D. C. E. Bakker, N. Metzl, A. Olsen, C. Sabine, N. Cassar, F. Reum, R. F. Keeling, and M. Heimann (2014). "Interannual sea-air CO₂ flux variability from an observation-driven ocean mixed-layer scheme." In: *Biogeosciences* 11.17, pp. 4599–4613. DOI: [10.5194/bg-11-4599-2014](https://doi.org/10.5194/bg-11-4599-2014) (cit. on p. 10).
- Rödenbeck, C. et al. (2015). "Data-based estimates of the ocean carbon sink variability – first results of the Surface Ocean CO₂ Mapping intercomparison (SOCOM)." In: *Biogeosciences* 12.23, pp. 7251–7278. DOI: [10.5194/bg-12-7251-2015](https://doi.org/10.5194/bg-12-7251-2015) (cit. on pp. 1, 10).
- Rodgers, K. B., J. Lin, and T. L. Frölicher (2015). "Emergence of multiple ocean ecosystem drivers in a large ensemble suite with an Earth system model." In: *Biogeosciences* 12.11, pp. 3301–3320. DOI: [10.5194/bg-12-3301-2015](https://doi.org/10.5194/bg-12-3301-2015) (cit. on pp. 9, 10).
- Sabine, Christopher L. et al. (2004). "The Oceanic Sink for Anthropogenic CO₂." In: *Science* 305.5682, pp. 367–371. DOI: [10.1126/science.1097403](https://doi.org/10.1126/science.1097403) (cit. on p. 1).
- Sallée, J. B., K. Speer, and R. Morrow (2008). "Response of the Antarctic Circumpolar Current to Atmospheric Variability." In: *Journal of Climate* 21.12, pp. 3020–3039. DOI: [10.1175/2007jcli1702.1](https://doi.org/10.1175/2007jcli1702.1) (cit. on p. 20).
- Sallée, J. B., K. G. Speer, and S. R. Rintoul (2010). "Zonally asymmetric response of the Southern Ocean mixed-layer depth to the Southern Annular Mode." In: *Nature Geoscience* 3.4, pp. 273–279. DOI: [10.1038/ngeo812](https://doi.org/10.1038/ngeo812) (cit. on p. 33).
- Sallée, J.-B., E. Shuckburgh, N. Bruneau, A. J. S. Meijers, T. J. Bracegirdle, and Z. Wang (2013a). "Assessment of Southern Ocean mixed-layer depths in CMIP5 models: Historical bias and forcing

- response." In: *J. Geophys. Res. Oceans* 118.4, pp. 1845–1862. DOI: [10.1002/jgrc.20157](https://doi.org/10.1002/jgrc.20157) (cit. on pp. 29, 36, 61).
- Sallée, J.-B., E. Shuckburgh, N. Bruneau, A. J. S. Meijers, T. J. Brace-girdle, Z. Wang, and T. Roy (2013b). "Assessment of Southern Ocean water mass circulation and characteristics in CMIP5 models: Historical bias and forcing response." In: *Journal of Geophysical Research: Oceans* 118.4, pp. 1830–1844. DOI: [10.1002/jgrc.20135](https://doi.org/10.1002/jgrc.20135) (cit. on pp. 27, 29).
- Sarmiento, Jorge L. and Nicolas Gruber (2006). *Ocean Biogeochemical Dynamics*. Princeton University Press (cit. on pp. 48–50).
- Schultzweida, Uwe, Luis Kornblueh, Ralf Müller, Karl-Hermann Wieners, and Oliver Heidmann (2017). *Climate Data Operators*. Max-Planck-Institute for Meteorology, Hamburg. URL: <http://www.mpimet.mpg.de/cdo> (cit. on p. 95).
- Six, Katharina D. and Ernst Maier-Reimer (1996). "Effects of plankton dynamics on seasonal carbon fluxes in an ocean general circulation model." In: *Global Biogeochemical Cycles* 10.4, pp. 559–583. DOI: [10.1029/96GB02561](https://doi.org/10.1029/96GB02561) (cit. on pp. 6, 8, 26).
- Smith, E. L. (1936). "Photosynthesis in relation to light and carbon dioxide." In: *Proc. Nat. Acad. Sci.* 22, pp. 504–511 (cit. on p. 8).
- Speer, Kevin, Stephen R. Rintoul, and Bernadette Sloyan (2000). "The Diabatic Deacon Cell." In: *Journal of Physical Oceanography* 30.12, pp. 3212–3222. DOI: [10.1175/1520-0485\(2000\)030<3212:TDDC>2.0.CO;2](https://doi.org/10.1175/1520-0485(2000)030<3212:TDDC>2.0.CO;2) (cit. on p. 27).
- Stevens, Bjorn et al. (2013). "Atmospheric component of the MPI-M Earth System Model: ECHAM6." In: *Journal of Advances in Modeling Earth Systems* 5.2, pp. 146–172. DOI: [10.1002/jame.20015](https://doi.org/10.1002/jame.20015) (cit. on pp. 5, 6, 20, 29).
- Stössel, Achim, Dirk Notz, F. Alexander Haumann, Helmuth Haak, Johann Jungclaus, and Uwe Mikolajewicz (2015). "Controlling high-latitude Southern Ocean convection in climate models." In: *Ocean Modelling* 86, pp. 58–75. DOI: [10.1016/j.ocemod.2014.11.008](https://doi.org/10.1016/j.ocemod.2014.11.008) (cit. on pp. 29, 36, 61).
- Sverdrup, H. U. (1953). "On Conditions for the Vernal Blooming of Phytoplankton." In: *Journal du Conseil International pour l'Exploration de la Mer* 18, pp. 287–295 (cit. on p. 39).
- Tagliabue, Alessandro, Jean-Baptiste Sallée, Andrew R. Bowie, Marina Lévy, Sebastiaan Swart, and Philip W. Boyd (2014). "Surface-water iron supplies in the Southern Ocean sustained by deep winter mixing." In: *Nature Geoscience* 7.4, pp. 314–320. DOI: [10.1038/ngeo2101](https://doi.org/10.1038/ngeo2101) (cit. on pp. 38, 45).
- Takahashi, Taro, J. Olafsson, J. Goddard, D. W. Chipman, and S. C. Sutherland (1993). "Seasonal variation of CO₂ and nutrients in the high-latitude surface oceans: a comparative study." In: *Global Biogeochem. Cycles* 7, pp. 843–878. DOI: [10.1029/93GB02263](https://doi.org/10.1029/93GB02263) (cit. on pp. 13, 35, 48).

- Takahashi, Taro et al. (2002). "Global sea-air CO₂ ux based on climatological surface ocean and pCO and seasonal biological and temperature effects." In: *Deep-Sea Research II*. doi: [10.1016/j.dsr2.2008.12.009](https://doi.org/10.1016/j.dsr2.2008.12.009) (cit. on p. 13).
- Takahashi, Taro, Colm Sweeney, Burke Hales, David W. Chipman, Timothy Newberger, John G. Goddard, Richard A. Iannuzzi, and Stewart C. Sutherland (2012). "The Changing Carbon Cycle in the Southern Ocean." In: *Oceanography* 25. doi: [10.5670/oceanog.2012.71](https://doi.org/10.5670/oceanog.2012.71) (cit. on p. 1).
- Talley, Lynne D. (2013). "Closure of the global overturning circulation through the Indian, Pacific and Southern Oceans: schematics and transports." In: *Oceanography* 26.1, pp. 80–97. URL: http://pordlabs.ucsd.edu/ltalley/papers/2010s/talley_GOC_oceanography_feb2013.pdf (cit. on pp. 1, 33).
- Taucher, J. and A. Oschlies (2011). "Can we predict the dirdirect of marine primary production change under global warming?" In: *Geophys. Res. Lett.* 38. doi: [10.1029/2010GL045934](https://doi.org/10.1029/2010GL045934) (cit. on p. 25).
- Taylor, Karl E., Ronald J. Stouffer, and Gerald A. Meehl (2012). "An Overview of CMIP5 and the Experiment Design." In: *Bull. Amer. Meteor. Soc.* 93.4, pp. 485–498. doi: [10.1175/bams-d-11-00094.1](https://doi.org/10.1175/bams-d-11-00094.1) (cit. on p. 9).
- Thompson, D. and J. Wallace (2000). "Annular Modes in the Extratropical Circulation. Part I: Month-Month Variability." In: *Journal of Climate* 13.5, pp. 1000–1016. doi: [10.1175/1520-0442\(2000\)013<1000:AMITEC>2.0.CO;2](https://doi.org/10.1175/1520-0442(2000)013<1000:AMITEC>2.0.CO;2) (cit. on p. 31).
- Thompson, David W. J., Susan Solomon, Paul J. Kushner, Matthew H. England, Kevin M. Grise, and David J. Karoly (2011). "Signatures of the Antarctic ozone hole in Southern Hemisphere surface climate change." In: *Nature Geoscience* 4.11, pp. 741–749. doi: [10.1038/ngeo1296](https://doi.org/10.1038/ngeo1296) (cit. on pp. 2, 20, 32, 60).
- Thompson, David W. J., Elizabeth A. Barnes, Clara Deser, William E. Foust, and Adam S. Phillips (2015). "Quantifying the Role of Internal Climate Variability in Future Climate Trends." In: *Journal of Climate* 28.16, pp. 6443–6456. doi: [10.1175/jcli-d-14-00830.1](https://doi.org/10.1175/jcli-d-14-00830.1) (cit. on pp. 9, 10, 12).
- United Nations (2015). "ADOPTION OF THE PARIS AGREEMENT." In: *Conference of the Parties*. URL: <https://unfccc.int/resource/docs/2015/cop21/eng/l09r01.pdf> (cit. on p. 62).
- Volk, Tyler and Martin I. Hoffert (1985). "Ocean Carbon Pumps: Analysis of Relative Strengths and Efficiencies in Ocean-Driven Atmospheric CO₂ Changes." In: *The Carbon Cycle and Atmospheric CO₂: Natural Variations Archean to Present*. American Geophysical Union, pp. 99–110. doi: [10.1029/GM032p0099](https://doi.org/10.1029/GM032p0099) (cit. on pp. 8, 35).
- Wang, Lei, Jianbin Huang, Yong Luo, and Zongci Zhao (2016). "Narrowing the spread in CMIP5 model projections of air-sea CO₂

- fluxes." In: *Scientific Reports* 6, p. 37548. doi: [10.1038/srep37548](https://doi.org/10.1038/srep37548) (cit. on pp. 1, 2).
- Wang, Shanlin and J. Keith Moore (2012). "Variability of primary production and air-sea CO₂ flux in the Southern Ocean." In: *Global Biogeochemical Cycles* 26. GB1008. doi: [10.1029/2010GB003981](https://doi.org/10.1029/2010GB003981) (cit. on p. 38).
- Wanninkhof, Rik (1992). "Relationship between wind speed and gas exchange over the ocean." In: *Journal of Geophysical Research: Oceans* 97.C5, pp. 7373–7382. doi: [10.1029/92JC00188](https://doi.org/10.1029/92JC00188) (cit. on p. 8).
- Weiss, R.F. (1974). "Carbon dioxide in water and seawater: the solubility of a non-ideal gas." In: *Marine Chemistry* 2, pp. 203–215. doi: [10.1016/0304-4203\(74\)90015-2](https://doi.org/10.1016/0304-4203(74)90015-2) (cit. on p. 7).
- Williams, N. L. et al. (2017). "Calculating surface ocean pCO₂ from biogeochemical Argo floats equipped with pH: An uncertainty analysis." In: *Global Biogeochemical Cycles*. doi: [10.1002/2016gb005541](https://doi.org/10.1002/2016gb005541) (cit. on p. 61).
- Williams, Richard G. and Michael J. Follows (2011). *Ocean Dynamics and the Carbon Cycle*. Cambridge University Press.
- Yuan, Xiaojun (2004). "ENSO-related impacts on Antarctic sea ice: a synthesis of phenomenon and mechanisms." In: *Antarctic Science* 16.4, pp. 415–425. doi: [10.1017/s0954102004002238](https://doi.org/10.1017/s0954102004002238) (cit. on p. 20).
- de Lavergne, Casimir, Jaime B. Palter, Eric D. Galbraith, Raffaele Bernardello, and Irina Marinov (2014). "Cessation of deep convection in the open Southern Ocean under anthropogenic climate change." In: *Nature Climate Change* 4, pp. 278–282. doi: [10.1038/nclimate2132](https://doi.org/10.1038/nclimate2132) (cit. on pp. 29, 61).

ACKNOWLEDGMENTS

Writing this thesis was an incredible journey of personal learning and failures, which I could not have accomplished without the help of my environment.

I thank my supervisors Tatiana Ilyina for setting the foundations of this thesis and guidance in contents, and Norbert Frank for external feedback and encouraging me to apply to an external research center like Max Planck Institute for Meteorology Hamburg ([MPI](#)).

I enjoyed my visit to the [HAMOCC](#) group in Hamburg. I especially thank Hongmei for high-frequency support, also Irene, Tinka and Jöran for their time and patience in explaining me the basics of marine biogeochemistry over and over again.

I also acknowledge [MPI](#) for the inhouse development of the extremely quick and easy-to-use commando-line to CDO [Schultzweida et al., [2017](#)] and Luis Kornblueh for running the historical Max Planck Institute-Earth System Model Large Ensemble ([MPI-ESM LE](#)).

Finally, I thank my parents for encouraging me to study what I strived for, financing my studies and for who they are. And Alisha for a great 2017.

DECLARATION

Erklärung:

Ich versichere, dass ich diese Arbeit selbstständig verfasst habe und keine anderen als die angegebenen Quellen und Hilfsmittel benutzt habe.

Heidelberg, Juni 2017

Aaron Spring